Application of Dynamic Fracture Mechanics to the Investigation of Catastrophic Failure in Aircraft Structures

Thesis by

Benjamin Chow

In Partial Fulfillment of the Requirements

for the Degree of

Doctor of Philosophy

Graduate Aeronautical Laboratories

California Institute of Technology

Pasadena, California

2001

(Defended May 25, 2001)

© 2001

Benjamin Chow

All Rights Reserved

To my parents,
Chung Tze and Huey Yung Chow,

My wife,
Freda,

And my brother,
Gary.

In memory of my late grandfather.

Acknowledgement

First and foremost, I would like to thank my two advisors Prof. Rosakis and Prof. Ravichandran for their continuous support, guidance and encouragement. I am very fortunate to work with not one, but two excellent advisors. Professor Rosakis is a great scholar and a perfect gentleman. He is always very enthusiastic about fracture mechanics, and often gets excited when we have new findings from the experiments. It is his enthusiasm and dedication to excellence in research and teaching that kept me motivated for my research and studies at Caltech.

I am greatly in debts to Prof. Ravichandran, without whom, I would not have been able to make it at Caltech. Prof. Ravichandran not only supported and directed my research work, he also helped me tremendously in my studies, especially at the time of my candidacy examination. Like a living encyclopedia, Prof. Ravichandran knows about almost everything. It is always fun to chat with him about things outside of research and listen to his stories and his views on the world. Being such a caring person, Prof. Ravichandran is the best mentor I could hope for.

I would like to thank Dr. Victor Chen of the Boeing Company for his support and input to my research project. From talking to an industry expert like him, I was able to relate my current academic research to real life applications in the aerospace industry. I would like to thank Prof. Joseph Shepherd and Prof. Kaushik Bhattacharya for being on my thesis committee and providing me with many valuable suggestions.

I am in debt to many members of Prof. Rosakis and Prof. Ravichandran's research groups. I would like give special thanks to Dr. Pradeep Guduru, from whom I learned what it takes to be a good experimentalist. Pradeep was very patient when he taught me the "art" of the dynamic fracture experiments. With him there to help me, I was able to succeed on my very first experiments. I would also like to thank Dr. David Owen for his help and support through out my years at Caltech. I have gained many insights and avoided many long routes by having discussions with Dave. I would like to thank the "other Dave" in the group, David Anderson, for the use of his great CGS digitization program. I think it is only a matter of time, before he becomes a millionaire from his CGS program or from being the father of two movie stars. I would like to thank Prof. Mikio Oda for his assistance in running my last batch of experiments, so that I could finish them in time to be included in my thesis. I would also like to thank Dr. Hansuk Lee, Dr. Tamim Carin, Dr. Omprakash Samudrala, Dr. Demir Coker and Petros Arakelian for their help and support.

I feel the years I have spent at Caltech have been some of the best years of my life. This would not be possible without some of my very best friends. Dr. Eric Burcsu has not only been one of my best friends but also helped me tremendously on my research. Nitin Deshpande has always been fun to chat with. Dr. Lavi Zuhal and I still have disagreement on who is better at the game of pool, although we always talk the same "talk." Ioannis Chasiotis, a very civilized gentleman, is also my gym partner. Many others at Caltech have made my graduate student life colorful, Shiming Zhuang,

Jun Lu, Dr. Sandeep Sane, Dr. Adam Rasheed, Dr. Ying Huang and Dr. Sairam Sundaram, just to name a few.

Finally, I would like to thank my family for their continuous support thoughout my years as a graduate student. I would like to thank my parents, both physics teachers, for passing on the love for science and engineering. I thank my parents for giving me the chance for a good education by leaving all their achievements behind and immigrating to the US. Their belief in me and their encouragement have carried me from start to finish during my Ph.D. program. I would also like to thank my brother Gary for his support. Last, but not least, I would like to thank my lovely wife, Freda. She had made many sacrifices just to support me while completing my degree. Her patience and love made me realize how important it was to successfully complete my degree in a timely manner for both of us. I will never forget how hard she worked while going to school to support me while completing my degree.

Abstract

A dynamic fracture mechanics approach to the estimation of the residual strength of aircraft structures is presented. The dependence of the dynamic crack initiation toughness of aluminum 2024-T3 on loading rate is first studied experimentally. A drop of up to 40% in the value of dynamic initiation toughness, K_{IC}^{d}, is discovered for loading rates in the range of $1.0\times10^{4} MPa\sqrt{m}/s$ to $1.0\times10^{6} MPa\sqrt{m}/s$. This range of loading rate corresponds to the typical rates found in an aircraft fuselage experiencing explosive loading conditions. A dramatic increase in the value of dynamic crack initiation toughness is also found for loading rates above $1.0\times10^{6} MPa\sqrt{m}/s$. Based on these results and on established dynamic fracture mechanic concepts, a fracture mechanics based failure model is established and is used to estimate the residual strength of aircraft structures.

A methodology to determine residual strength of dynamically loaded structures based on global structural analysis coupled with local finite element analysis is introduced. Local finite element calculations were performed for different loading rates, $\dot{\sigma}$, ranging from $1\times10^{5} MPa/s$ to $1\times10^{8} MPa/s$, to simulate the conditions encountered in an explosively loaded aircraft fuselage. Simulations were conducted at a number of loading rates for the following cases of relevance to aircraft fuselage: (i) center cracked panels, (ii) rivet holes with wing cracks, (iii) biaxially loaded panels and (iv) panels pre-stressed to simulate pressurization. The results from the analyses were then used in conjunction with the experimental results for the dynamic fracture toughness of a 2024-

T3 aluminum alloy as a function of loading rate, K_{IC}^{d} vs. $\dot{K}^{d}(t)$, to determine the time to failure, t_f, for a given loading rate. A failure envelope, σ_f vs. $\dot{\sigma}$, based on the failure model and finite element analysis, is presented for the different cases and the implications for the residual strength of aircraft structures is discussed.

Mixed mode dynamic crack initiation in aluminum 2024-T3 alloy is investigated by combining experiments with numerical simulations. Pre-fatigued single edge notched specimens and three point bend specimens are subjected to dynamic symmetric and asymmetric loading to generate a range of mode mixity at the cracktip. The optical technique of coherent gradient sensing (CGS) and a strain gage method are employed to study the evolution of the mixed mode stress intensity factors. The dynamic mixed mode failure envelope is obtained using the crack initiation data from the experiments at a nominal loading rate of $7\times10^{5} MPa\sqrt{m}/s$ and is compared with the static counterpart for 2024-T3 aluminum alloy. The fracture surfaces near the crack initiation site are investigated using a scanning electron microscope and reveal ductile void growth and coalescence. Numerical simulations of the experiments are conducted to both help in designing the experiments and to validate the results of the experiments. The numerical simulations show good correlation with the experimental results.

Table of Contents

Introductory Remarks

This doctoral dissertation consists of three chapters, each with its own abstract, introduction and conclusions. The overall theme of this work is the investigation of dynamic failure of structural materials such as 2024-T3 aluminum alloy through combined experimental procedures and numerical techniques to arrive at fracture mechanics based failure criteria that are applicable to the study of catastrophic failure of structures.

In the first chapter, a dynamic fracture mechanics approach to the estimation of the residual strength of aircraft structures is presented. The dependence of the dynamic crack initiation toughness of aluminum 2024-T3 on loading rate is first studied experimentally. Based on these results and on established dynamic fracture mechanic concepts, a fracture mechanics based failure model is established and is used to estimate the residual strength of aircraft structures.

In the second chapter, global structural analysis is conducted, coupled with local finite element analysis that includes the capability of addressing issues related to dynamic fracture mechanics. Local finite element calculations are performed for different loading rates to simulate the conditions encountered in an explosively loaded aircraft fuselage. The results from the analyses were then used in conjunction with the experimental results obtained in the first chapter to obtain a stress and stress rate based failure envelope. The implications for the residual strength of aircraft structures are discussed.

Chapter 3 deals with mixed mode dynamic crack initiation in aluminum 2024-T3 alloy by combining experiments with numerical simulations. Pre-fatigued single edge notched specimens and three point bend specimens are subjected to dynamic symmetric and asymmetric loading to generate a range of mode mixity at the cracktip. The optical technique of coherent gradient sensing (CGS) and a strain gage method are employed to study the evolution of the mixed mode stress intensity factors. A dynamic mixed mode failure envelope is obtained for a nominal loading rate. The fracture surfaces near the crack initiation site are investigated using a scanning electron microscope to study the micromechanism of failure. Numerical simulations of the experiments are also conducted to both help in designing the experiments and to validate the results of the experiments.

Chapter 1

Dynamic Fracture Mechanics Approach to the Estimation of the Residual Strength of Impulsively Loaded Structures: Part I: Experiments and Theoretical Methodology

Abstract

In the present two parts study, a dynamic fracture mechanics approach to the estimation of the residual strength of aircraft structures is presented. In Part-I, the dependence of the dynamic crack initiation toughness of aluminum 2024-T3 on local crack tip loading rate is first studied experimentally. The rate of change of the dynamic stress intensity factor is adopted as a measure of stress rate. A drop of up to 40% in the value of dynamic initiation toughness K_{IC}^{d} is discovered for loading rates in the range of $1.0\times10^{4} MPa\sqrt{m}/s$ to $1.0\times10^{6} MPa\sqrt{m}/s$. This range of loading rate corresponds to the typical rates found in an aircraft fuselage experiencing explosive loading conditions. A dramatic increase in the value of dynamic crack initiation toughness is also found for loading rates above $1.0\times10^{6} MPa\sqrt{m}/s$. Based on these results and on established dynamic fracture mechanics concepts, a theoretical fracture mechanics failure model is established and is used as an example to demonstrate the proposed methodology. In Part II of this study, the methodology is used in conjunction with realistic numerical models to estimate the residual strength of aircraft structures.

1.1 Introduction

Explosive loading due to accidents or threats can produce extensive structural damage to aircraft structures resulting in substantial loss of their load bearing ability (Kanninen & O'Donoghue, 1995). In order to understand the behavior and the residual strength of the overall aircraft structure under such loading conditions, one needs to investigate the failure behavior of structural aluminum under high rates of loading. The loading rate for an explosively loaded aircraft can be as high as $50x10^6$ N/s (Kamoulakos, Chen, Mestreau & Lohner, 1996), with strain rates in the range of $10^6 - 10^7$ s^{-1} (Meyers, 1994). A schematic of an aircraft damaged in a typical simulated bomb blast experiment is shown in Figure 1, while a photograph of a controlled explosion experiment performed on a decommissioned aircraft structure is shown in Figure 2.

Conventional analyses of failure in full-scale structures subjected to explosive loading often utilize ad-hoc failure criteria based on the attainment of critical levels of stress corresponding to failure initiation. Such critical stress levels are often arbitrarily chosen to be fractions of the yield stress and are assumed to be uniform throughout the structure, irrespective of the rate of loading experienced at different locations. Let us consider an aging airplane, with multi-site damage at its rivet holes, subjected to blast loading as shown in Figure 1 (Kanninen & O'Donoghue, 1995). When such an aircraft structure is subjected to explosive dynamic loading, the cracks are subjected to high loading rates. Under such conditions, the fatigue cracks can initiate and propagate for

substantial distances. When many of these cracks propagate and connect, catastrophic failure of the structure occurs, as illustrated in Figure 1. Such a failure mode scenario is highly possible and is consistent with observations. Consequently, we expect that dynamic fracture mechanics based analyses can provide valuable insights into the initiation of dynamic cracks from pre-existing fatigue crack sites in aging airplanes subjected to blast loading.

In the present work (both Parts I and II), basic concepts of dynamic fracture mechanics are used to rationalize, examine and refine the stress-based approach. In order to achieve this, detailed models describing the fracture behavior at high rates of loading are needed. A typical commercial aircraft fuselage structure is made from 2024-T3 aluminum alloy. In order to investigate the residual strength of aircraft structures subjected to intense dynamic loading, one needs to first characterize the dynamic fracture response of the aluminum alloy itself. Unlike quasi-static material and fracture properties, the corresponding dynamic values are not readily available in the literature. However, what is well documented is that the dynamic fracture toughness of most structural materials is a strong function of the loading rate (Freund, 1990, Costin and Duffy, 1979, Liu, Knauss and Rosakis, 1998, Freund, Duffy and Rosakis, 1981). Indeed, extensive research has been done to determine the dynamic fracture toughness, K_{IC}^{d}, of ductile materials such as high strength steels. Owen *et al.* (1998) have also conducted experiments on a 2024-T3 aircraft grade aluminum alloy over a range of loading rates (see Figure 3). However, no data points for K_{IC}^{d} were obtained for loading rates between $1\times10^{4}\ MPa\sqrt{m}/s$ and $1\times10^{6}\ MPa\sqrt{m}/s$, clearly shown by the gap in this figure. This

loading rate region corresponds to rates experienced by fuselage fatigue cracks during typical bomb blast events (Kamoulakos *et al.*, 1998). As a result, it becomes crucial to understand the dynamic fracture behavior in this missing region. In this study (Part I), different dynamic experimental techniques are used to obtain the value of K_{IC}^{d} for loading rates in the important but unexplored range between $1\times10^{4}\ MPa\sqrt{m}/s$ and $1\times10^{6}\ MPa\sqrt{m}/s$.

The experimentally obtained fracture toughness versus loading rate relation can be subsequently used to predict crack initiation time and failure load levels in structures containing pre-existing cracks. The methodology for achieving this is also illustrated in Part I of this study by means of a simple example in which the fracture criterion can be implemented in conjunction with existing analytical solutions for the dynamic stress intensity factor history in simple geometries. In Part II of this study, the same methodology is extended to the numerical failure analysis of an aircraft structure containing pre-existing fatigue cracks. A combined global/local numerical approach connecting the global stress state of the fuselage to the local fracture initiation behavior is implemented. Estimates of the failure stress as a function of local stress rate in the impulsively loaded fuselage are thus obtained, demonstrating the power of the methodology.

1.2 Dynamic Initiation Criterion

1.2.1 DYNAMIC FRACTURE MECHANICS BACKGROUND

It has long been recognized that two-dimensional, near-tip deformation fields (plane strain or plane stress) in the vicinity of dynamically loaded cracks have universal spatial structures when they are either stationary or propagating. If such cracks are loaded symmetrically, the magnitude of this field is controlled by a time-dependent scalar, the dynamic stress intensity factor. As stated by Freund and Clifton (1974), the stress field with reference to a Cartesian coordinate system centered at the crack tip of all plane elastodynamic solutions can be asymptotically described by the following expression:

$$\sigma_{\alpha\beta} = \frac{K_I^d(t)}{\sqrt{2\pi r}} f_{\alpha\beta}(\theta) + O(l) \; as \; r \rightarrow 0. \qquad (1)$$

Here, (r, θ) is a polar coordinate system centered at the crack tip, $f_{\alpha\beta}(\theta)$ is a known universal function of time and K_I^d is called the dynamic stress intensity factor. For stationary cracks that are dynamically loaded (e.g., by means of stress waves), the amplitude, K_I^d, of the asymptotic stress field is time varying and is a function of the time history of the load and the specimen geometry.

It is also known that for more realistic materials, where the near crack tip region develops a contained active plastic zone, relation (1) will still hold in the elastic region surrounding the zone of contained plasticity. In such a case, the dynamic stress intensity factor also characterizes the fracture process and determines the time varying, size and

shape of the active plastic zone. This situation is often referred to as a condition of "small scale yielding" (Freund, 1990). Small scale yielding (S.S.Y.) has been experimentally found to accurately approximate fracture events in many high strength metals such as most steels, aluminum, and titanium alloys used in engineering practice. As a result, dynamic fracture criteria, even if contained plasticity is present, can still be simply formulated by means of parameters such as the dynamic stress intensity factor.

The mechanical fields around the crack tip (and thus the instantaneous values of the stress intensity factors in equation (1)) can be obtained in principle within the context of linear elastic continuum mechanics as long as the configuration of the body and the details of time-dependent loading are also specified. This is often achieved numerically by means of the finite element method. However, since the initiation and motion of the crack tip is controlled completely by the transient deformation state and the micromechanics of separation of the surrounding material, the initiation of the crack tip cannot be specified a priori. Due to the fact that the usual constitutive equation for the material does not include the possibility of material separation, a mathematical statement of a crack initiation and growth criterion must be added to the governing equations. Such a criterion must be stated as a physical postulate of material behavior. This criterion should be at the same level as the kinematical theorems governing deformation, momentum balance principles, as well as the constitutive relation describing material response. The most common form for such a criterion is the requirement that the crack must initiate and then continue to grow at a particular crack tip speed in such a way that some parameter defined as part of the crack tip field maintain a certain critical level.

The critical level is specific to the material, temperature and local strain rate experienced at the crack tip, where the decohesion process takes place. For dynamically loaded stationary cracks, the near tip strain rate, and thus this critical level, depends on the resulting crack face opening rate just before crack initiation. The resulting critical level of dynamic stress intensity factor sustainable by the material at particular loading rates (stationary cracks) is called the dynamic initiation fracture toughness of the material. These critical levels and their dependence on rate and temperature can only be determined through experimental measurements. For a detailed discussion of dynamic fracture criteria, see Rosakis and Ravichandran, (2000).

1.2.2 DYNAMIC INITIATION AT DIFFERENT LOADING RATES

It has been observed experimentally that growth initiation of a stationary crack or flaw of length a_o at time $t= t_o$ occurs when the instantaneous value of the stress intensity factor, $K_I^d(t)$, at $t=t_o$ reaches a critical value which is dependent on the material. In addition, this critical value also depends on the local, near-tip strain rate. A measure of this rate for small scale yielding is the time rate of change of the stress intensity factor (i.e., $\dot{K}_I^d$) (Freund, Duffy & Rosakis, 1981, Ravi-Chandar and Knauss, 1984a, Dally and Barker, 1988, Suresh *et al.,* 1990, Owen *et al.,* 1998). This dependence reflects the local nonlinear deformation processes at the crack tip which generally are rate dependent, such as a rate dependent yield stress (strain rate hardening), and/or local thermal softening due to the adiabatic conversion of plastic work into heat. For ductile solids it also reflects the

rate and inertia-dependent processes of void nucleation, growth and coalescence responsible for eventual crack extension. Given the above, the dynamic crack initiation criterion takes the form

$$K_I^d(P(t), a_o) = K_{IC}^d(\dot{K}_I^d(t)) \quad at\ t = t_o \tag{2}$$

In the above equation, the left-hand side is the instantaneous value of the dynamic stress intensity factor, symbolically represented as a function of some generalized transient load *P(t)*. Alternatively, the right-hand side represents the critical value for initiation and is a material and temperature dependent function of loading rate, which is represented as $\dot{K}_I^d(t) = dK_I^d / dt$. The left-hand side is calculated using numerical techniques modeling the specific geometry and transient loading, whereas the right-hand side can only be determined experimentally for a specific material. The experimental measurement as a function of loading rate is best achieved in an arrangement which can provide a wide range of loading rates and a well characterized loading history. Once the right hand side has been obtained experimentally, Eq. (2) will provide the time of initiation and the level of stress intensity factor at that instant. For a particular boundary value problem, it will also provide the maximum amplitude of the time varying loads at which crack growth will commence. For analytical examples of the left-hand side of Eq. (2), see Freund (1990).

1.3 Experiments

In order to establish the complete dependence of the dynamic initiation fracture toughness K_{IC}^{d} *vs.* $\dot{K}_{I}^{d}$ for the 2024-T3 aluminum alloy (a typical material used in commercial aircraft fuselage), different loading methods and diagnostics techniques were utilized. The dynamic loading is provided by a drop weight tower or by a gas gun. The optical method of Coherent Gradient Sensing (CGS) (Rosakis, 1990) used in conjunction with high speed photographs and strain gages (Dally, 1993) were simultaneously used as real time diagnostics.

1.3.1 SPECIMEN DESIGN AND PREPARATION

Two different designs of the double cantilever beam specimens were utilized in this study. The dimensions of the specimens are illustrated in Figure 4. The specimens were 150mm in width and 87.3mm in height. All specimens were made from commercial grade 2024-T3 aluminum alloy plate stock of two different thicknesses. From here forward, we will denote Type A specimens to be the ones made from 5 mm thick plates and Type B specimens to be the ones made from the 10 mm thick plates. The specimen notches (260 μm wide) in both type A and B specimen were made by using wire EDM (Electric Discharge Machining). The specimens were pre-fatigued to introduce a sharp crack at the tip of the notch. The total length of the resulting crack was 18.75 mm. The typical length of the fatigue crack was about 2 mm. By fatiguing, we are also able to move the crack tip away from heat affected zone introduced by the EDM wire. The pre-fatiguing is carried out following the procedures outlined in ASTM standards.

Since we are using optical techniques such as CGS to conduct the majority of the experiments, it is necessary to create a reflective and optically flat specimen surface. This was achieved by lapping the aluminum plates and by subsequently polishing the flat, gray surfaces to make them spectacularly reflective. Lapping is done by using an industry standard lapping machine, which can make the specimens flat, and remove the surface non-uniformities caused by the plastic zones resulting from the fatiguing process. The specimens are polished by hand using different particle sizes of diamond paste to achieve the desired reflectivity. The strain gages for measuring the strains near the crack tip were fixed by a strain gage adhesive to the back (non-reflective) side of the specimens.

1.3.2 DYNAMIC LOADING

Two types of dynamic loading devices were used to conduct the dynamic crack initiation experiments – a gas gun and a drop weight tower. Low impact speed experiments featured specimens loaded in a three point bend loading configuration under a drop weight tower (Dynatup 8100A), with a tup mass of 250 kg. The impact speeds ranged from 2 m/s to 10 m/s. Higher impact speed experiments featured a custom-made gas gun used to fire a 2.5 kg projectile into a specimen at speeds of up to 50 m/s.

1.3.3 THE COHERENT GRADIENT SENSING METHOD

The majority of the experiments were performed with CGS (Coherent Gradient Sensing) in combination with strain gage measurements, which will be discussed in the following section. The technique of CGS is a shearing interferometric technique which, when used in a reflection mode, is sensitive to the in-plane gradients of the surface out-of-plane displacements at the specimen. The method of CGS was first developed at Caltech by Rosakis and his co-workers. The technique, its principle and background information was briefly described in the original papers by Tippur *et al.* (1991) and also in an extensive review article by Rosakis (1993). A typical gas gun experiment using CGS is illustrated in Figure 5. A collimated laser beam from an Innova Sabre argon-ion pulsed laser is first reflected from the surface of the specimen under impact and is subsequently optically sheared by two parallel, high-density gratings which are placed in the optical path. The distance between the gratings is denoted here as Δ. The gratings produce multiple diffraction spots of orders 0, ± 1, ± 2, ... on a filter plane and the interference fringe pattern from the +1 or the −1 order spot is used. The image from the gratings is then focused by a convex lens and the images are captured by a Cordin, Inc., model 330A rotating-mirror-type high-speed film camera, which is capable of taking 80 frames (pictures) at up to 2 million frames per second.

By appropriately rotating the gratings, the beam can be sheared either in a direction perpendicular to the crack (x_2) or in a direction parallel to the crack (x_1). Shearing and subsequent interference results in an optical differentiation of the reflected wavefront and provides information on the components of the time-varying surface

slopes in the vicinity of the crack tip. The governing equations for interpreting the interference fringes are (Rosakis, 1993):

$$u_{3,1} = \frac{\partial u_3}{\partial x_1} = \frac{mp}{2\Delta}, \tag{3}$$

$$u_{3,2} = \frac{\partial u_3}{\partial x_2} = \frac{np}{2\Delta}, \tag{4}$$

where u_3 is the time varying out of plane displacement field of the specimen surface, x_1 and x_2 are the directions of shearing of the beam, m and n are the fringe orders for the two cases and p is the pitch of the gratings, which equals to 25.4 μm in the current study. Figure 6 shows two pictures of typical fringe patterns obtained by shearing either in the x_1 or x_2 directions, respectively. Each fringe in these pictures represent the locus of constant $u_{3,1}$ or $u_{3,2}$ values of surface slope components. Since the fringes are sensitive only to the gradients of displacements, they are insensitive to infinitesimal rigid motions of the specimen during deformation, which makes CGS an excellent full-field optical technique for dynamic fracture mechanics experiments.

The entire experimental system shown in Figure 5 is triggered when the projectile fired by the gas gun impacts the trigger strain gage attached to the top of the impact point of the specimen. Upon impact, the pulse laser is triggered and emits 80 discrete coherent light pulses (514.5 nm wavelength, 20 ns pulse in width) with an inter-pulse time of 2 μs. These pulses, collimated to a diameter of 50 mm, pick up information about the out-of-plane gradient-field displacement when reflected from the specimen surface. The

reflected wavefront passes through the CGS setup, and the resulting interference fringe patterns are then recorded using the high-speed camera. The images are recorded on TMAX 3200 high-sensitivity film. The field-of-view of the images on the film is approximately a circle of 27 mm in diameter. Accurate synchronization between the laser, high-speed camera and the strain gage for both triggering and recording purposes is crucial to insure the success of the experiments. A high-speed digital oscilloscope (Nicolet Model 440) at a sampling rate of 5 MHz is used to record all the strain gage signals as well as the impactor speed, which is measured using interrupted optical beams.

The film from the high speed camera is developed and the negatives are scanned into the computer by a high resolution Epson Scanner (Expression 636). The fringes are digitized using MATLAB and the crack tip location with respect to the original crack tip, $\Delta a(t)$, and values of $K_I^d(t)$ are calculated and recorded.

In order to calculate the dynamic stress intensity factor, $K_I^d(t)$, we assume that the near-tip stress field of the dynamically loaded crack is under conditions of small scale yielding and is well described by plane stress elastodynamics. The following asymptotic equations are used to relate the stress intensity factor to the specimen surface slopes near the crack tip (Rosakis, 1993):

$$\frac{np}{2\Delta} = \frac{\nu h}{2E\sqrt{2\pi}} K_I r_1^{\frac{3}{2}} \cos\frac{3\theta_1}{2} = u_{3,1} . \qquad (5)$$

In equation (5), n is the fringe order, p is the pitch of the gratings, Δ is the distance between the gratings, ν is the Poisson's ratio, h is the specimen thickness and E is the Young's modulus.

1.3.4 THE STRAIN GAGE METHOD

During the dynamic crack initiation experiments, near tip strain gage measurements are also used to record the time history of $K_I^d(t)$ up to crack initiation. The method used in these experiments is described in detail in a review article by Dally and Berger (1993). Figure 7 illustrates the coordinate system transformation that Dally et al. used to obtain the stress intensity factors from the strain gage measurements. The location of the gage is also illustrated in the diagram. The origin of the coordinate system is located at the crack tip, and $-x_1$ coincides with the crack line. The optimal orientation of the gage with respect to the crack line depends on the Poisson's ratio ν of the material that is being investigated. The higher order linear elastic asymptotic stress field is used to relate the measured strain, $\varepsilon_g(t)$, to the stress intensity factor, $K_I^d(t)$, as follows:

$$2\mu\varepsilon_g = \frac{K_I}{\sqrt{2\pi r}}\left(k\cos\frac{\theta}{2} - \frac{1}{2}\sin\theta\sin\frac{3\theta}{2}\cos 2\alpha + \frac{1}{2}\sin\theta\cos\frac{3\theta}{2}\sin 2\alpha\right). \quad (6)$$

In the above expression, $\alpha = \cos^{-1}(-k)$, $k = (1-\nu)/(1+\nu)$ and $\mu = E/2(1+\nu)$.

For aluminum 2024-T3 with Poisson's ratio $\nu \cong 0.33$, Eq. (6) is maximized to give optimal strain gage orientation values that will enhance the signal at $\theta = \alpha = 60°$. Then Eq. (6) reduces to

$$K_I = E\sqrt{\frac{8}{3}\pi r \varepsilon_g}\,. \tag{7}$$

By recording the time history of the strain gage data, $\varepsilon_g(t)$, one can obtain $K_I(t)$ using Eq. (7). The crack initiation time, t_i, can be obtained by examining a major deviation from linearity in $\varepsilon_g(t)$. The value of K_I^d at $t=t_i$ is the dynamic fracture toughness K_{IC}^d corresponding to a particular rate of loading.

The strain gages used in the experiments are 350 Ω gages obtained from Micro-Measurements. (model EA-06-062AQ-350). Each gage is placed 6 mm from the tip of the fatigue crack and is oriented at an angle of 60° to the crack line. (x_1 - direction). The strain gage signals were recorded with the Nicolet Model 440 digital oscilloscope with a sampling rate of 5 MHz.

1.4 Results and Discussion

1.4.1 THE CGS STUDY

The optical technique of CGS and high speed photography were used in both the gas gun setup and drop weight tower experiments for both type A and type B specimens. Different high-speed camera frame rates were chosen in the experiments for different rates of loading. Figure 8 shows a series of CGS fringe from a typical experiment using the drop weight tower at a low impact speed of 3 m/s. In order to identify the dynamic crack initiation toughness, K_{IC}^{d}, one needs to identify the time at which crack initiation takes place. One way to locate the crack initiation in the high-speed CGS images is to look at the geometrical characteristics of the back loops ($-x_1$ direction) on the fringe pattern. As the slope of the back loop of the fringe start to become perpendicular to the crack, the initiation is said to take place. This change in fringe pattern occurs due to the change in features of surface deformation resulting from the initiation of crack growth by tunneling in the middle of the specimen. The accurate way to identify crack initiation is to plot the crack extension, history $\Delta a(t)$, deduced from locating the current crack tip through the optical data fitting procedures that have been described before. As $\Delta a(t)$ increases outside of the noise zone, one can identify the initiation by extrapolating the linear portion of the $\Delta a(t)$ curve backwards and intersecting it with the abscissa (t-axis) to estimate the initiation point. The procedure is clearly shown in Figure 9. Figure 10 shows a typical $K_I^d(t)$ vs. t from a CGS experiment, each data point is obtained by fitting the fringe pattern using the procedure described in Section 1.3.3. The initiation time, t_i, is marked by an arrow and was identified using the change in shape of the back loop in the fringe pattern.

Once the initiation time, t_i, is identified, then one can use the $K_I^d(t)$ vs. t plot to identify the dynamic crack initiation toughness, K_{IC}^d, as $K_I^d(t_i)$. The corresponding crack extension, $\Delta a(t)$ vs. t, is shown in Figure 9.

1.4.2 THE STRAIN GAGE STUDY

Strain gage results were analyzed from the raw signals recorded using the high-speed digital oscilloscope. Figure 11 shows the raw strain gage signal from a typical drop weight tower experiment at an impact speed of 5 m/s. Since the oscilloscope begins to acquire data before the specimen is impacted (usually the system is triggered by the projectile velocity measurement system or by the triggering flag on the drop weight tower), it is possible to identify the time of impact, t_o, from the triggering strain gage that is fixed at the point of impact. Time t_o is shown in Figure 11 (a) as an abrupt jump in the gage signal. Since all of the strain gage signals are recorded on the same oscilloscope, t_o can be subtracted from the actual time of initiation to accurately determine the initiation time, t_i. This t_i can later be compared with that estimated from the CGS measurement which is conducted simultaneously.

Figure 11 (b) shows typical strain gage data for the same experiment as discussed in the CGS section (Drop weight tower, impact velocity of 5 m/s). An apparent deviation from linearity is observed at $t = 166\ \mu s$. This corresponds to the crack initiation time, t_i, (note that this t_i is measured by appropriately accounting for the value of t_o in Figure 11(a)). Figure 12 shows the $K_I^d(t)$ history calculated from the strain gage signal using

Eq. (7) for the same experiment. The crack initiation toughness, K_{IC}^{d}, is identified by $K_I^d(t_i)$. In this case, the computed K_{IC}^{d} from the strain gage signal at $t=t_i$ is 19 $MPa\sqrt{m}$. The loading rate $\dot{K}_I^d$ is calculated from the slope of the first nearly linear portion of $K_I^d(t)$ until crack initiation. In this case, the crack tip loading rate $\dot{K}_I^d$ is 1.2×10^5 $MPa\sqrt{m}/s$.

1.4.3 CORRELATION BETWEEN CGS AND STRAIN GAGE DATA

As illustrated in the previous two sections, we have performed data reduction on both the CGS and the strain gage measurements for the same impact experiment. Most the experiments were conduct with both CGS and strain gage diagnostics simultaneously. By doing so, we were not only able to compare the results from the two different methods but also help pin point the time of crack initiation in cases where initiation is not obvious in either measurement.

An example of the comparison between the two techniques is shown using the data from CGS (Figure 10) and data from strain gages (Figure 12). As seen from the strain gage data, initiation occurs at $t=166\ \mu s$, as discussed in Section 1.4.2. In Figures 9 and 10, one can see that the CGS data shows that initiation occurs at $t=178\ \mu s$ for the same experiment. The initiation times obtained from these distinctly different techniques agree reasonably well. Comparing the K_{IC}^{d} obtained from the two techniques, we find that they are very similar in value; their difference being less than 5%.

By correlating these two methods, one can take advantage of the multiplicity and redundancy of measurements for cross checking and minimizing any user induced error. Thus, it is possible to pin point the time of crack initiation accurately. Indeed, one is able to make a more objective judgment regarding the crack initiation time as well as the stress intensity factor. The close match in the results also increases confidence on these two well-known dynamic fracture experimental methods. Indeed, one should be able to confidently use either method as a means of determining the dynamic initiation toughness in case one of the two experimental setups is not readily available.

1.4.4 THE DEPENDENCE OF CRACK INITIATION TOUGHNESS ON LOADING RATE

For each experiment, the value for K_{IC}^{d} is determined by using CGS, strain gages or a combination of both. The loading rate, $\dot{K}_I$, is calculated by taking the slope of the linear portion of the $K_I^d(t)$ up to initiation. The summary of results for the series of experiments using both type A and type B specimens is shown in Figure 13. Figure 13 also shows results from experiments conducted on much smaller specimens of the same material by Owen *et al.* (1998). The different loading rates in their investigation were achieved by using either a tensile Kolsky (split Hopkinson) bar or a servo-hydraulic MTS system and covered a wide, albeit discontinuous, spectrum of dynamic loading rates. Due to the limitations associated with maximum attainable hydraulic loading rates, the maximum $\dot{K}_I$ obtained in this configuration was of the order of $10^4\ MPa\sqrt{m}/s$. Also,

similar limitations of the Hopkinson bar technique restricted testing to values of $\dot{K}_I > 8\times10^5\ MPa\sqrt{m}/s$, leaving a substantial gap (two orders of magnitude) in the measured behavior. It is perhaps fortuitous that the techniques described herein are able to cover this gap since it contains the most interesting trend in the toughness versus loading rate behavior as evident from the figure. The plot shows that K_{IC}^d remains close to its static value of $30\ MPa\sqrt{m}$ for rates up to $1\times10^4\ MPa\sqrt{m}/s$. For loading rates from $1\times10^4\ MPa\sqrt{m}/s$ to $1\times10^6\ MPa\sqrt{m}/s$, we see a substantial decline (drop) in the value of K_{IC}^d, with a minimum value of K_{IC}^d at $18.4\ MPa\sqrt{m}$. This corresponds to a 40% decrease from the static level. The decrease in fracture toughness with rate can perhaps be attributed to the generation of a substantial adiabatic temperature rise at the crack tip. Indeed, at such intermediate loading rates, even if inertial effects may not yet be dominant, local conditions within the developing crack tip plastic zone often become adiabatic. In structural metals subjected to low speed impact conditions, recent full field, dynamic measurements of the crack tip temperatures using high speed IR thermography (Zehnder, Guduru, Rosakis and Ravichandran, 2001) have revealed temperature increases exceeding 150°c at crack initiation. The implication of this is self evident. In a material such as aluminum 2024-T3, the yield stress at the vicinity of the crack tip will drop with increasing adiabatic temperature (20% or more), enhancing the growth of the voids that control the crack initiation process. Since this particular aluminum alloy is not rate sensitive, the thermal effects will be the only dominant influence at these intermediate loading rates, thus providing a plausible scenario for the decrease in the value of K_{IC}^d. For loading rates higher than $1\times10^6\ MPa\sqrt{m}/s$, we see a dramatic increase in the value

of K_{IC}^{d}. The data in this regime presented herein matches with the results of Owen *et al.* (1998) obtained by entirely different loading and data reduction techniques and much smaller specimen geometries. The increase in K_{IC}^{d} value is typically attributed to inertial effects which significantly retard the activation of failure mechanisms such as void growth or micro-crack nucleation in the vicinity of the main crack (Tong and Ravichandran, 1995, Ravi-Chandar and Knauss, 1984, Liu, Knauss and Rosakis, 1998). Indeed, as the loading rates are increased, inertia effects start dominating the void nucleation and growth process (Tong and Ravichandran 1995). In addition, and as illustrated by Liu, Knauss and Rosakis (1998), extremely high loading rates result in the inability of the dynamic, singular near-tip stress field to establish itself quickly enough at finite distances ahead of the crack. This translates to inefficient loading of the voids or micro-cracks which are expected to eventually trigger initiation of crack growth. This effect, which was first shown to be very important even for purely brittle solids, is purely inertia driven and accounts for a phenomenal increase in apparent dynamic fracture toughness. An alternative explanation of this phenomenon has recently been presented by Basu and Narasimhan (2000) for ductile rate sensitive materials. In their work, they attributed the dramatic increase in toughness to loading rate increase related loss of crack tip constraint.

Finally, it should be noted here that the results from the two types of specimens with different thickness yield similar results for the same loading rates and are comparable to that of Owen *et al.* (1998), who used much smaller specimens of thickness between 1.63mm and 2.54mm.

1.5 Implementations of the Fracture Criterion

Once the functional dependence of the dynamic fracture toughness on loading rate is established experimentally, the fracture criterion discussed in Section 1.2.2 can be implemented to study particular cases involving a variety of fracture geometries and dynamic loading histories. Indeed, this functional dependence determined the right hand side of Eq. (2) for any particular material. The left hand side of the same equation can be determined either analytically or numerically, given a structure and a dynamic loading history. In this section we consider a simple example for which the left hand side can be expressed in terms of closed form analytical representations. This example is used to demonstrate how dynamic fracture mechanics concepts can be utilized to provide structural design parameters (e.g., failure stress levels) in dynamically loaded structures. In Chapter 2, the same methodology is used to treat a much more realistic case, i.e. the case of an aging aircraft structure with wide spread fatigue damage subjected to dynamic, explosive loading.

1.5.1 AN ANALYTICAL EXAMPLE

We treat the simple case of an infinitely large solid (an infinite, thin plate to be exact) which contains a central crack of finite length, 2a, subjected to mode-I loading through the arrival of a dilatational wave at time t=0 (see Figure 14). The wave subjects

the crack to a tensile in plane stress pulse, $\sigma = \sigma(t)$, which will be assumed to vary linearly with time as follows:

$$\sigma(t) = \dot{\sigma} t, \quad t > 0, \quad \dot{\sigma} > 0 \tag{8}$$

In the above equation, $\dot{\sigma}$ is the stress rate and is a parameter that provides a macroscopic measure of the local dynamic loading rate in the structure and is expected to vary from location to location depending on proximity to the source of explosive loading. As we will see from Chapter 2, in explosively loaded fuselages, this linearity assumption of the local stress is not a bad approximation for at least 200 μs after the explosion.

In order to make the problem analytically tractable, in addition to the linearity assumption, we also consider two extreme limiting situations. The first one corresponds to the case of very dynamic loadings (high loading rate, $\dot{\sigma}$), and the other to very low loading rates such that quasi-static stress intensity factor calculations are good assumptions. In the first case, provided that the crack initiation time, t_c, is shorter than the travel time, $2a/c_R$, of Rayleigh waves between the two crack tips, the crack behaves as essentially semi-infinite (Freund, 1990) and the each of the tips is still unaware of the presence of the other. In this case, the dynamic stress intensity factor history is given by (Freund, 1990):

$$K^d(t) = 2/3 C \dot{\sigma} \sqrt{2\pi c_l} t^{3/2}, \qquad C = \sqrt{\frac{2(1-2\nu)}{\pi(1-\nu)}} \tag{9}$$

As state above, Eq. (9) would hold provided:

$$2a / c_R \geq t_c = \sigma_c / \dot{\sigma}\,, \tag{10}$$

where σ_c is the critical level of applied stress at crack initiation. For this to be a good approximation, Eq. (10) implies that the crack length should be long enough and the pulse rate high enough so that

$$a \geq \frac{\sigma_c c_R}{2\dot{\sigma}}\,. \tag{11}$$

For the second case (low loading rate), the dynamic stress intensity factor will be given by the quasi-static formula for a crack length 2a, i.e.:

$$K^d(t) = \sigma(t)\sqrt{\pi a} = \dot{\sigma} t \sqrt{\pi a}, \tag{12}$$

where time enters through the fact that the loading stress, $\sigma(t)$, is still allowed to be time varying.

In the first extreme (High loading rate $\dot{\sigma}$ or long crack), the rate of change of the dynamic stress intensity factor is given by

$$\dot{K}^d(t) = C\dot{\sigma}\sqrt{2\pi c_l t} \qquad (13)$$

Eliminating time between (8) and (13) provides an explicit relation between K^d and $\dot{K}^d$ as follows:

$$K^d = \frac{2/3(\dot{K}^d)^3}{C^2\dot{\sigma}^2(2\pi c_l)} \qquad (14)$$

For a specific set of elastic properties (values of C and c_l), equation (14) represents a one parameter family of curves relating K^d and $\dot{K}^d$ with $\dot{\sigma}$ as the parameter. This family can now be displayed on the K^d, $\dot{K}^d$ space.

To implement the fracture criterion of Eq. (2), one should recall that for crack initiation under dynamic loading conditions, the instantaneous value of the dynamic stress intensity factor, $K^d(t)$, and its rate $\dot{K}^d(t)$, should equal a critical pair of values $(K_c^d, \dot{K}_c^d)$ at $t=t_c$ which lies on the experimentally obtained dynamic fracture toughness vs. rate curve of Figure 12. By using Eq. (14) together with the fracture criterion, the above statement is equivalent to:

$$K^d = \frac{2/3(\dot{K}^d)^3}{C^2\dot{\sigma}^2(2\pi c_l)} = K_c^d(\dot{K}), \qquad (15)$$

where $K_c^d(\dot{K})$ is the experimentally obtained toughness variation. Indeed, a graphical representation of this process (furnishing solutions of (15)) is shown in Figure 15, where the intersections between the left hand side and right hand side of (15) for different rates, $\dot{\sigma}$, furnish different pairs of dynamic stress initiation toughness and its rate corresponding to initiation at various macroscopic loading rates.

Once these intersections are determined, Eq. (13) can be now used to determine the time of initiation, $t=t_c$, for each loading rate, $\dot{\sigma}$, symbolically denoted here as $t_c = \hat{t}_c(\dot{\sigma})$. This plot is shown here in Figure 16.

Finally, the critical level of stress, σ_c, at the time of crack initiation can be obtained as a function of stress rate, $\dot{\sigma}$, by applying Equation 8 at $t=t_c$ as follows:

$$\sigma_c = \dot{\sigma} t_c = \dot{\sigma} \hat{t}_c(\dot{\sigma}) = \hat{\sigma}_c(\dot{\sigma}). \qquad (16)$$

Eq. (16) furnishes the variation of σ_c with $\dot{\sigma}$ and is displaced in Figure 17.

It should be recalled at this time that our first approximation strictly holds for either long cracks or very high $\dot{\sigma}$. Indeed, the results of this analysis are independent of the pre-existing crack length and will be useful only at locations close to the center of the explosive loading.

To implement the other extreme case (low stress rate), which is represented by the quasi-static analysis adjusted for dynamic loading, we employ a similar methodology to the one described above. In this case the stress intensity factor is given by Eq. (12) while its rate of change is given by:

$$\dot{K}^d(t) = \dot{\sigma}\sqrt{\pi a}\,. \tag{17}$$

For each value of $\dot{\sigma}$, $\dot{K}^d$ is constant with time. However in this case $\dot{K}^d$ also depends on the pre-existing crack length 2a. For a fixed initial pre-crack length, implementation of the fracture criterion requires intersecting the toughness curve with the vertical line corresponding to different values of $\dot{K}^d(t) = \dot{\sigma}\sqrt{\pi a}$ for each stress rate $\dot{\sigma}$. This will provide the level of K_{IC}^d for each stress rate and will thus determine the initiation time t_c as a function of $\dot{\sigma}$. To obtain the variation of σ_c as a function of $\dot{\sigma}$, one only has to recall that $\sigma_c = K_c^d / \sqrt{\pi a}$ and directly apply the fracture criterion i.e.:

$$\sigma_c = \frac{K_c^d(\dot{K}^d)}{\sqrt{\pi a}} = \frac{K_c^d(\dot{\sigma}\sqrt{\pi a})}{\sqrt{\pi a}}. \tag{18}$$

It should be noted that the above relation depends on the functional form of the toughness vs. rate curve (i.e. $K_c^d(\dot{K}^d)$) but also depend on the crack length a. This is in contrast to the equivalent result, displaced in Figure 17, for the case of a very long crack or a very high loading rate. To point out this difference, the results of the extreme analyses are displaced here in Figure 18 for different crack lengths. The figure clearly shows the

strong dependence of critical stress, σ_c, on loading rate, $\dot{\sigma}$. It also shows that for small loading rates, there is a strong dependence of σ_c on pre-existing crack length, 2a. The existence of a distinct minimum in all of these cases clearly reflects the presence of a minimum in the material dependent dynamic fracture toughness vs. $\dot{K}^d$ curve in Figure 13. This minimum raises a red flag against relying on purely static fracture design which may not be conservative, as often assumed in the literature.

For intermediate loading rates, neither analysis is expected to be very accurate. However, the methodology presented here can indeed be extended numerically to elaborate cases involving both fully dynamic loading histories and finite pre-crack lengths of more complex shapes as encountered in real aircraft structures (e.g. fatigue winged cracks emitted from rivet holes). This approach is demonstrated in Part II of this investigation. As is noted in this Chapter, depending on the distance of a pre-existing fatigue crack from the site of the explosive loading, the local rate, $\dot{\sigma}$, will vary and, through Figure 18, would initiate a crack in this location. Indeed if a large structural code is to be used, one could possibly use the relation between σ_c and $\dot{\sigma}$ to analyze different explosive scenario by pronouncing an element failed if this macroscopic criterion is met. This allows for the incorporation of dynamic fracture concepts without efficiently requiring the structural code to resolve stress states at the level of individual fatigue cracks of an aging airplane structure.

1.6 Conclusions

Dynamic impact experiments have been conducted on three-point bend, 2024-T3 aluminum alloy specimens with different specimen geometries and thicknesses. The time history of dynamic stress intensity factor and the time of crack initiation were measured based on CGS as well as strain gage data. The two techniques are found to yield consistent data and are shown to be very useful tools in accurately estimating dynamic crack initiation times for structural metals, a task that has been a serious experimental challenge in the past. By using the two methods, the dynamic initiation toughness, K_{IC}^{d}, was obtained for different loading rates. The dynamic initiation toughness, K_{IC}^{d}, vs. loading rate, $\dot{K}$, was subsequently documented for a wide range of loading rates spanning 7 order of magnitude. Loading rates that were unattainable in earlier investigations (between $1\times10^{4}\ MPa\sqrt{m}/s$ and $1\times10^{6}\ MPa\sqrt{m}/s$), were achieved in the present experimental study by using various specimen geometries and using both a drop weight and a gas gun setup. A drop in the value of K_{IC}^{d} relative to its static value was observed in the loading rate range of $1\times10^{4}\ MPa\sqrt{m}/s$ to $1\times10^{6}\ MPa\sqrt{m}/s$. A significant increase in K_{IC}^{d} is observed for loading rates above $1\times10^{6}\ MPa\sqrt{m}/s$. This decrease and subsequent increase in the value of K_{IC}^{d} can be attributed to the competition between inertial and thermal effects on material failure. A more detailed microscopic experimental investigation, coupled with numerical simulations, will be needed to understand the reason behind the observed drop, followed by increase in the value of K_{IC}^{d} as a function of loading rate. For the range of thickness tested, the functional dependence of K_{IC}^{d} on $\dot{K}$ for the 2024-T3 aluminum alloy appears to be independent of thickness, and the results corresponding to different specimen geometries and loading configurations are

found to yield a single unique functional form relating toughness to loading rate. This further verifies that dynamic initiation toughness is an inherent material property, which, as such, is independent of geometrical effects and depends on loading rate only through an appropriate local measure.

Reference

T.L. Anderson, *Fracture Mechanics*, CRC Press, Boston (1991).

Basu S, Narasimhan R, A comparative study of dynamic, ductile fracture initiation in two specimen configurations *International Journal of Fracture* 102 (2000), (4) 393-410.

J. Barnes and R.L. Peters, The challenge of commercial aircraft survivability. *Aerospace America* (1992) pp. 55-56.

Costin, L.S. and Duffy, J., 1979. The Effect of Loading Rate and Temperature on The Initiation of Fracture in a Mild, Rate Sensitive Steel. *Journal of Engineering Materials and Technology*, 101, 258-264

J.W. Dally, Dynamic photoelastic studies of fracture. *Experimental Mechanics* 19 (1979) 349-367.

J.W. Dally and J.R. Berger, The role of electrical resistance strain gages in fracture research. *Experimental Techniques in Fracture* (Edited by J.S. Epstein) VCH Publishers, Inc., New York (1993) pp. 1-39.

X. Deng and A.J. Rosakis, Dynamic crack propagation in elastic-perfectly plastic solids under plane stress conditions. *Journal of the Mechanics and Physics of Solids* 39 (1991) 683-722.

X. Deng and A.J. Rosakis, A finite element investigation of quasi-static and dynamic asymptotic crack tip fields in hardening elastic-plastic solids under plane stress - I. Crack growth in linear hardening materials. *International Journal of Fracture* 57 (1992a) 291-308.

X. Deng and A.J. Rosakis, A finite element investigation of quasi-static and dynamic asymptotic crack tip fields in hardening elastic-plastic solids under plane stress - II. Crack growth in power-law hardening materials. *International Journal of Fracture* 58 (1992b) 137-156.

L.B. Freund and R. Clifton, On the uniqueness of plane elastodynamic solutions for running cracks. *Journal of Elasticity* 4 (1974) 293-299.

L.B. Freund, J. Duffy, and A.J. Rosakis, Dynamic fracture initiation in metals and preliminary results on the method of caustics for crack propagation measurements. ASME Paper No. 81-PVP-15, (1981).

L.B. Freund and A.S. Douglas, The Influence of Inertia on Elastic-Plastic Antiplane Shear Crack Growth. *Journal of the Mechanics and Physics of Solids* 30 (1982) 59-74.

L.B. Freund, *Dynamic Fracture Mechanics* Cambridge University Press (1990).

G.R. Irwin, Crack extension force for a part-through crack in a plate. *Journal of Applied Mechanics* 29 (1962) 651-654.

A. Kamoulakos, V.L. Chen, E. Mestreau and R. Lohner, Finite element modelling of structure/fluid interaction in explosively loaded aircraft fuselage panels using pamshock/pamflow coupling. Presented at the Conference of on Spacecraft Structures, Materials and Mechanical Testing, ESA/CNES/DARA, Noordwijk, The Netherlands, (1996).

M.F. Kanninen and C.H. Popelar, *Advanced Fracture Mechanics* Oxford University Press, New York (1985).

M.F. Kanninen and P.E. O'Donoghue, Research challenges arising from current and potential applications of dynamic fracture mechanics to the integrity of engineering structures. *International Journal of Solids and Structures*, 32 (1995) 2423-2445.

M. Kosai, A. Shimamoto, C.-T. Yu, A.S. Kobayashi and P. Tan, A biaxial test specimen for crack arrest studies. *Experimental Mechanics* 36 (1996) 277-283.

P.S. Lam and L.B. Freund, Analysis of dynamic growth of a tensile crack in an elastic-plastic material. *Journal of the Mechanics and Physics of Solids* 33 (1985) 153-167.

C. Liu, W.G. Knauss, and A.J. Rosakis, Loading rates and the dynamic initiation toughness in brittle solids. *International Journal of Fracture* 90 (1998) 103-118.

H. Maigre and D. Rittel, Dynamic fracture detection using the force-displacement reciprocity: application to the compact compression specimen. *International Journal of Fracture* 73 (1995) 67-79.

M.A. Meyers, *Dynamic Behavior of Materials*, John-Wiley & Sons, New York (1994).

D.M. Owen, S.M. Zhung, A.J. Rosakis and G. Ravichandran, Experimental determination of dynamic crack initiation and propagation fracture toughness in thin aluminum sheets *International Journal of Fracture* 90 (1998) 153-174.

K. Ravi-Chandar and W.G. Knauss, An experimental investigation into dynamic fracture: i. crack initiation and arrest. *International Journal of Fracture* 25 (1984) 247-262.

D. Rittel and H. Maigre, A study of mixed-mode dynamic crack initiation in PMMA. *Mechanics Research Communications* 23 (1996a) 475-481.

D. Rittel and H. Maigre, An investigation of dynamic crack initiation in PMMA. *Mechanics of Materials* 23 (1996b) 229-239.

A.J. Rosakis, J. Duffy and L.B. Freund, The determination of the dynamic fracture toughness of aisi 4340 steel by the shadow spot method. *Journal of the Mechanics and Physics of Solids* 34 (1984) 443-460.

A.J. Rosakis, Two optical techniques sensitive to gradients of optical path difference: the method of caustics and the coherent gradient sensor (CGS). In: *Experimental Techniques in Fracture (Ed. Epstein, J.), VCH, New York,* 1993 327-425.

A.J. Rosakis and G. Ravichandran, Dynamic Failure mechanics. *International Journal of Solid and Structures* 37 (2000) 331-348

C.F. Shih, Relationships between the *J*-integral and the crack opening displacement for stationary and extending cracks. *Journal of the Mechanics and Physics of Solids* 29 (1981) 305-326.

C.F. Shih, Tables of Hutchinson-Rice-Rosengren singular field quantities. (1983).

H.V. Tippur, S. Krishnaswamy, and A.J. Rosakis,. Optical mapping of crack tip deformations using the method of transmission and reflection coherent gradient sensing: a study of crack tip *k*-dominance. *International Journal of Fracture* 52 (1991) 91-117.

W. Tong and G. Ravichandran, Inertia effects on void growth in viscoplastic materials. *Journal of Applied Mechanics* 62 (1995) 633-639.

M.L. Wilson, R.H. Hawley, and J. Duffy, The effect of loading rate and temperature on fracture initiation in 1020 hot-rolled steel. *Engineering Fracture Mechanics* 13 (1980) 371-385.

A.T. Zehnder and A.J. Rosakis, Dynamic fracture initiation and propagation in 4340 steel under impact loading. *International Journal of Fracture* 43 (1990) 271-285.

List of figures

Figure 10. $K_I^d(t)$ vs. t for a CGS drop weight tower experiment (impact speed 5m/s)

Figure 11. Strain gage signals with triggering signals for a drop weight tower experiment (impact speed 5m/s)

Figure 12. $K_I^d(t)$ calculated from the strain gage signal for a CGS drop weight tower experiment (impact speed 5m/s)

Figure 13. Experimentally determined K_{IC}^d *vs.* $\dot{K}_I^d$ data compared with result from Owen *et al.* (1998).

Figure 14. Schematic of an infinitely large solid contains a central crack of finite length 2a, subjected to mode-I loading of a dilatational tensile wave $\sigma(t)$.

Figure 15. Graphical representations of the intersection between the experimentally determined K_{IC}^d *vs.* $\dot{K}_I^d$ data with the case of dynamic analytical solution for a central crack of finite length, 2a, subjected to mode-I loading of a dilatational tensile wave, $\sigma(t)$, in an infinite solid.

Figure 16. The time to failure, t_c, as a function of loading rate, $\dot{\sigma}$, for the case of dynamic analytical solution for a central crack of finite length, 2a, subjected to mode-I loading of a dilatational tensile wave, $\sigma(t)$, in an infinite solid.

Figure 17. Failure stress, σ_c, as a function of loading rate, $\dot{\sigma}$, for the case of dynamic analytical solution for a central crack of finite length, 2a, subjected to mode-I loading of a dilatational tensile wave $\sigma(t)$ in an infinite solid.

Figure 18. Comparison of the failure stress, σ_c, as a function of loading rate, $\dot{\sigma}$, between the case of dynamic analytical solution (long crack, high loading rate) and the case of low stress rate implemented using quasi-static approach.

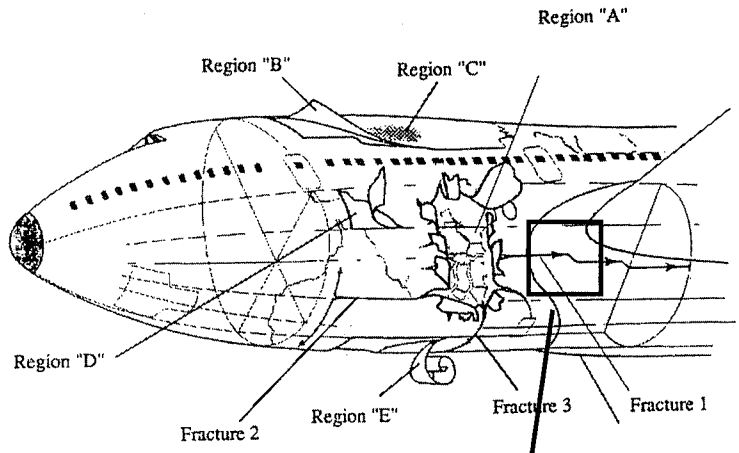
Region "A"
Region "B"
Region "C"
Region "D"
Fracture 2
Region "E"
Fracture 3
Fracture 1

(a)

(b)

Figure 1

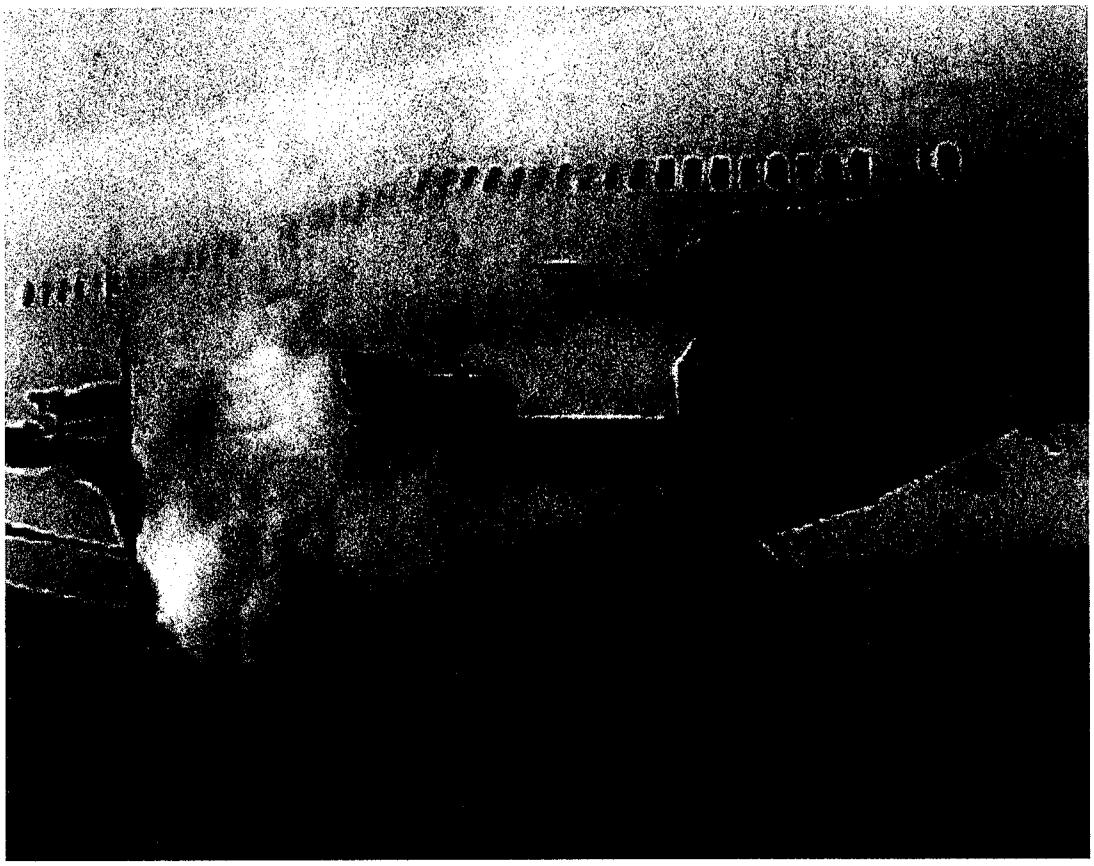

Figure 2

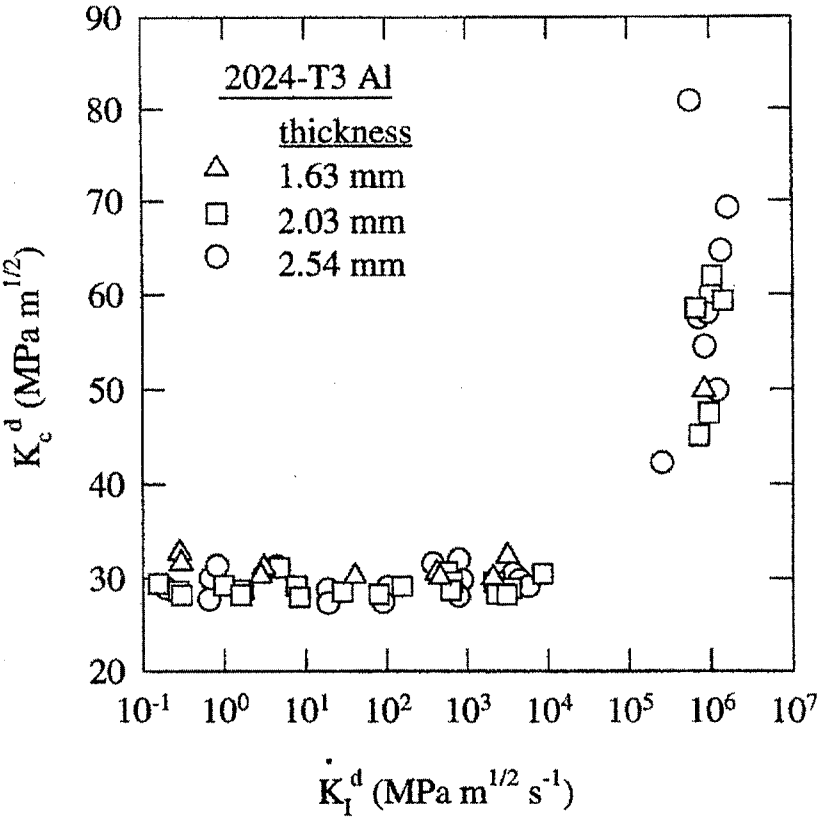
2024-T3 Al
thickness
1.63 mm
2.03 mm
2.54 mm
90
80
70
60
50
40
30
20
K_c^d (MPa m$^{1/2}$)
10^{-1} 10^0 10^1 10^2 10^3 10^4 10^5 10^6 10^7
$\dot{K}_I^d$ (MPa m$^{1/2}$ s^{-1})

Figure 3

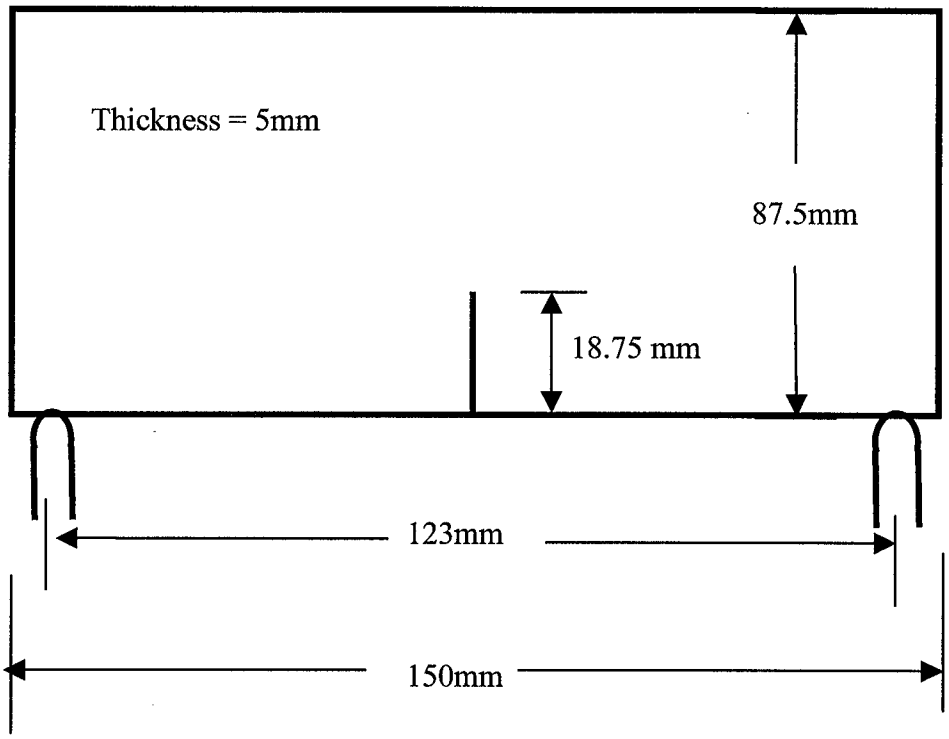

Figure 4

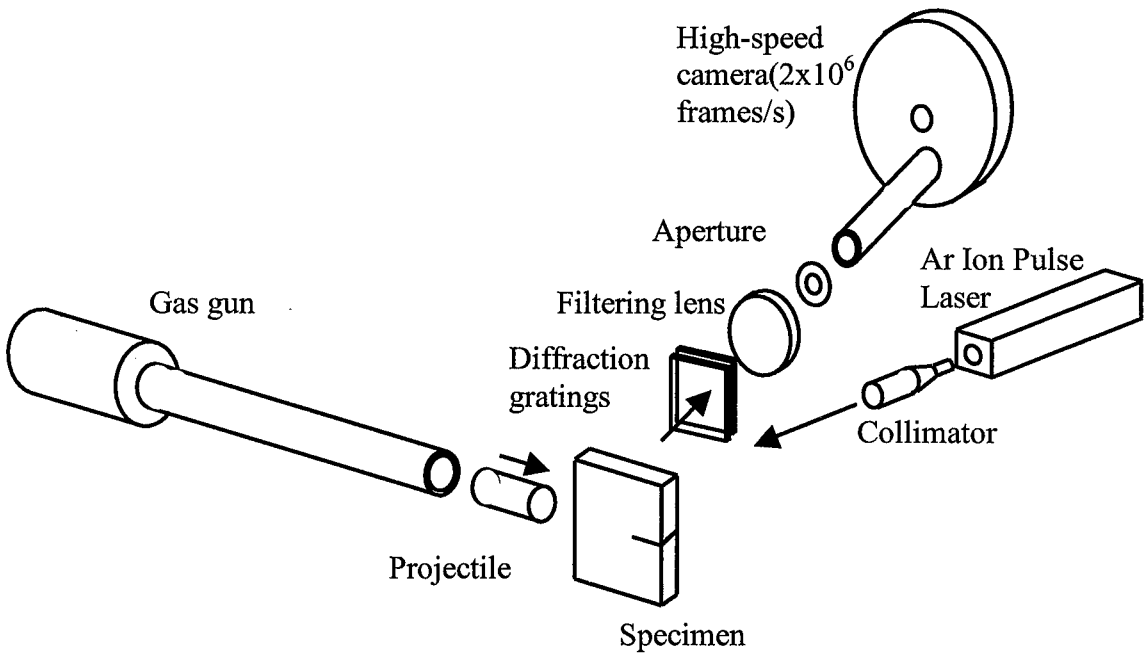
High-speed
camera(2x10^6
frames/s)
Aperture
Ar Ion Pulse
Laser
Gas gun
Filtering lens
Diffraction
gratings
Collimator
Projectile
Specimen

Figure 5

(a)

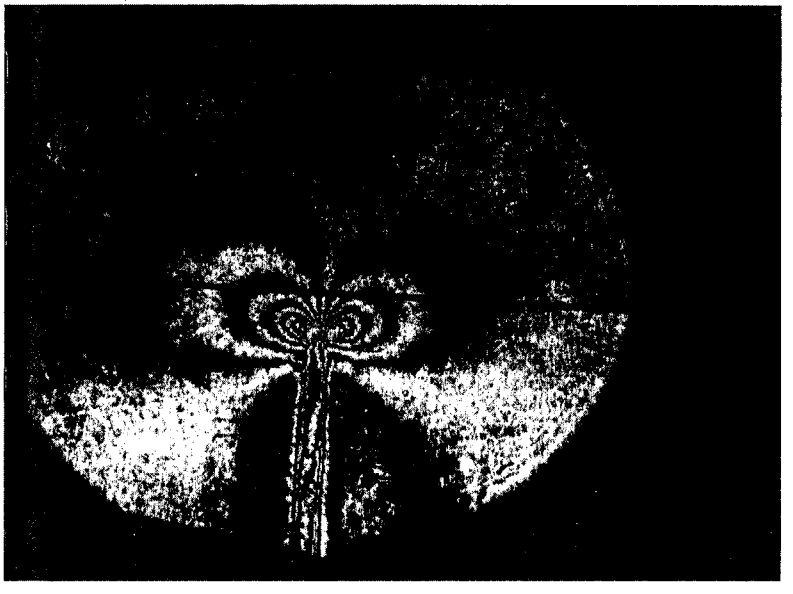

(b)

Figure 6

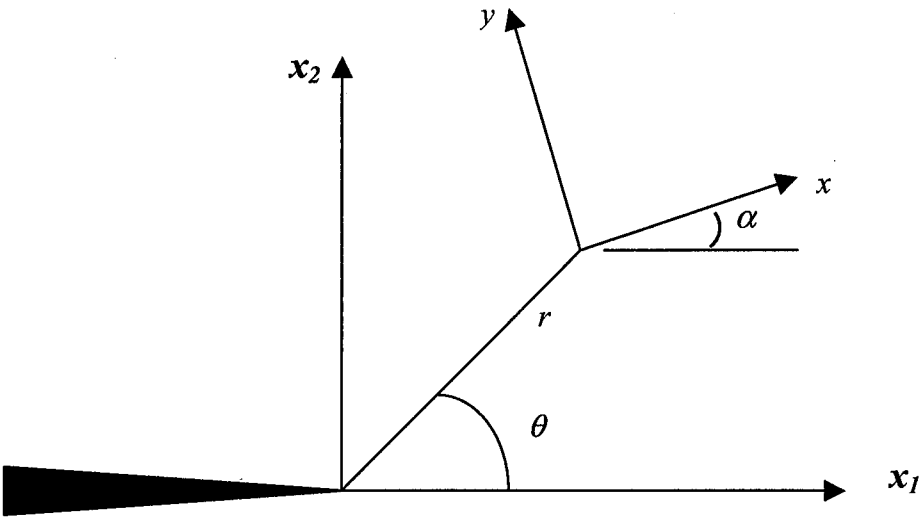

Figure 7

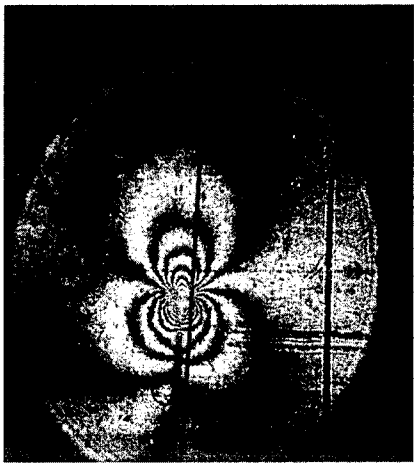

141.61μs

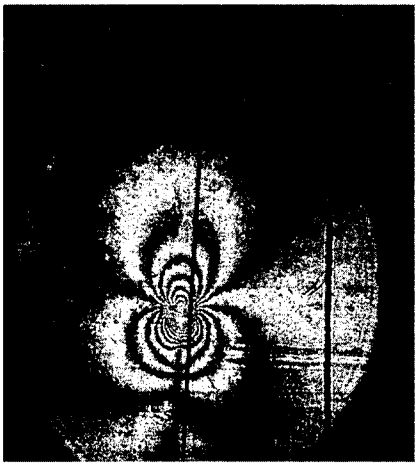

158.27μs

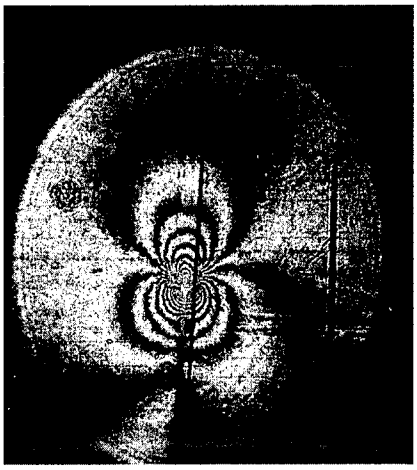

166μs

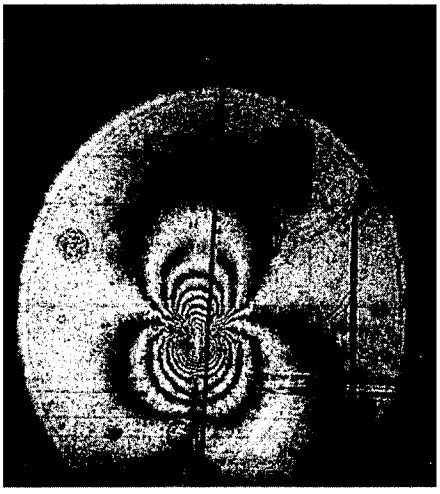

174.93μs

Figure 8

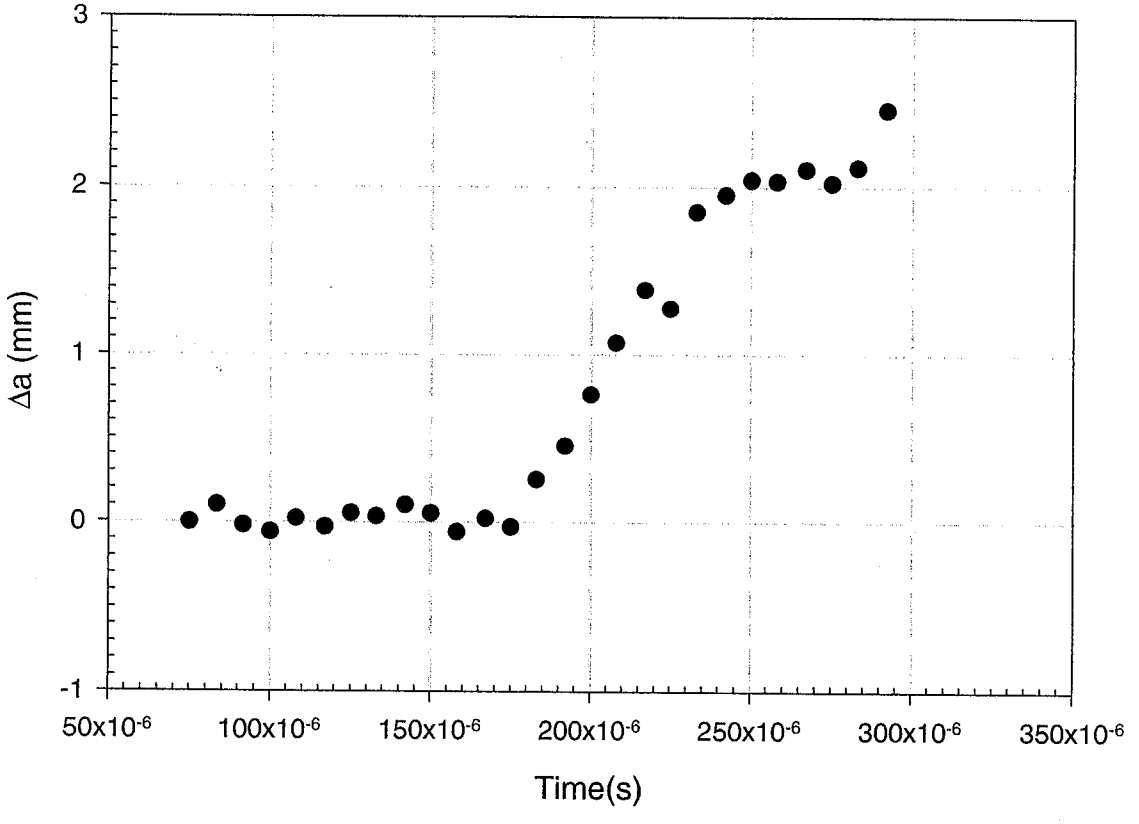
3
2
1
0
-1
Δa (mm)
50x10-6
100x10-6
150x10-6
200x10-6
250x10-6
300x10-6
350x10-6
Time(s)

Figure 9

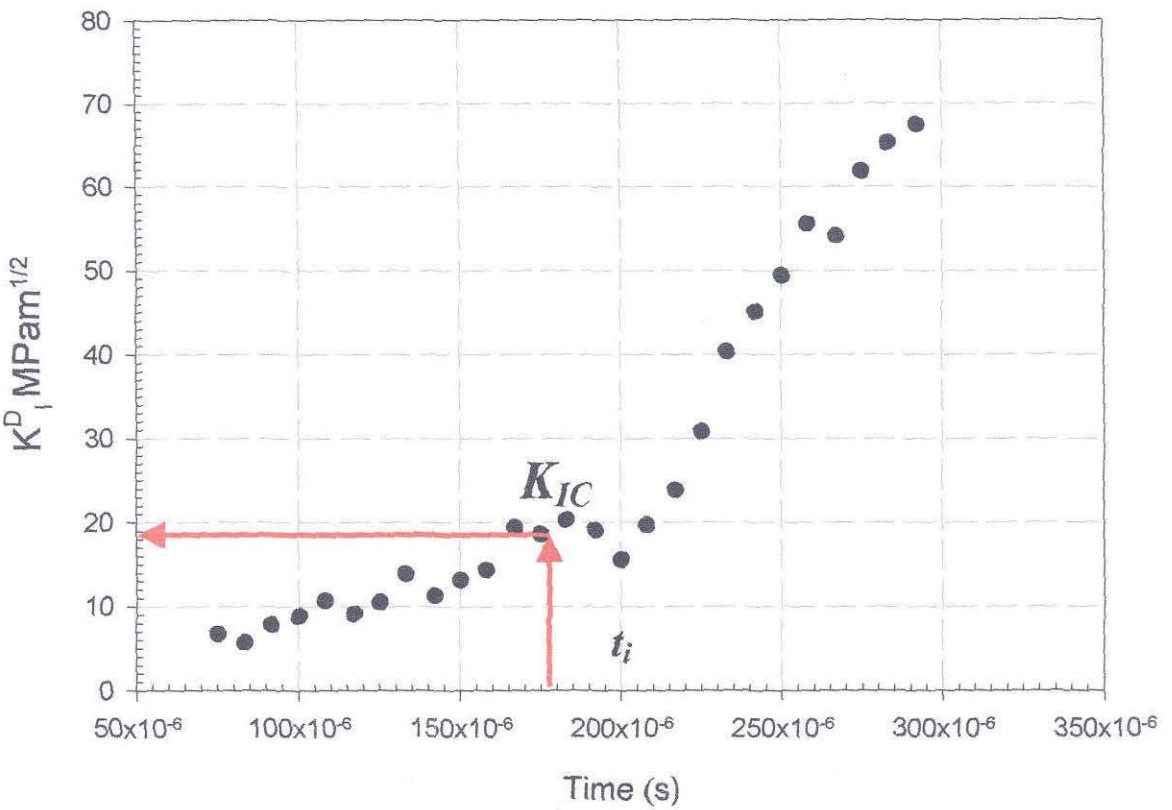
80
70
60
50
40
30
20
10
0
K^D_I MPam$^{1/2}$
K_{IC}
t_i
50x10^{-6}
100x10^{-6}
150x10^{-6}
200x10^{-6}
250x10^{-6}
300x10^{-6}
350x10^{-6}
Time (s)

Figure 10

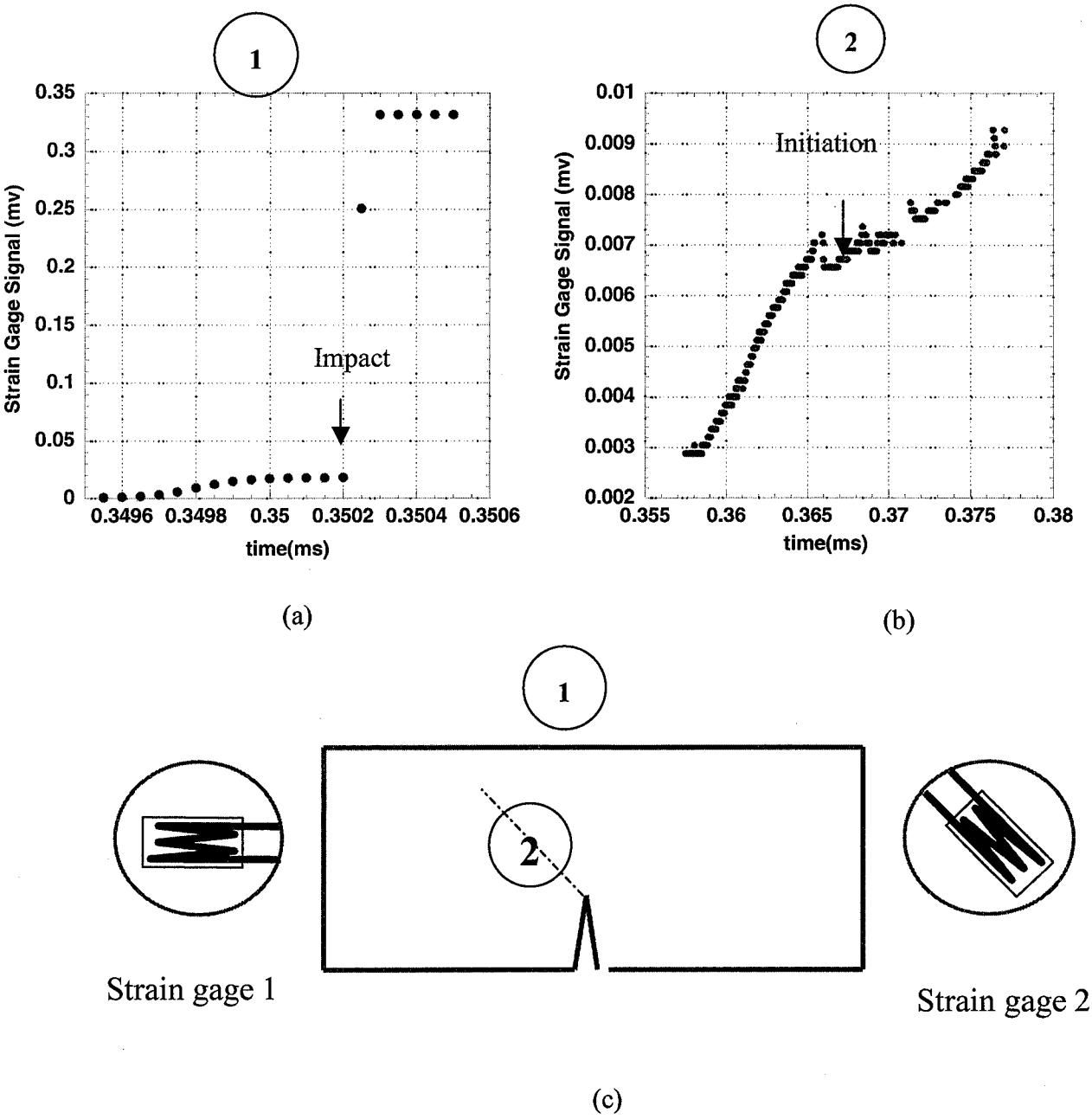
1
Strain Gage Signal (mv)
0.35
0.3
0.25
0.2
0.15
0.1
0.05
0
Impact
0.3496 0.3498 0.35 0.3502 0.3504 0.3506
time(ms)
(a)
2
Strain Gage Signal (mv)
0.01
0.009
0.008
0.007
0.006
0.005
0.004
0.003
0.002
Initiation
0.355 0.36 0.365 0.37 0.375 0.38
time(ms)
(b)
1
2
Strain gage 1
Strain gage 2
(c)

Figure 11

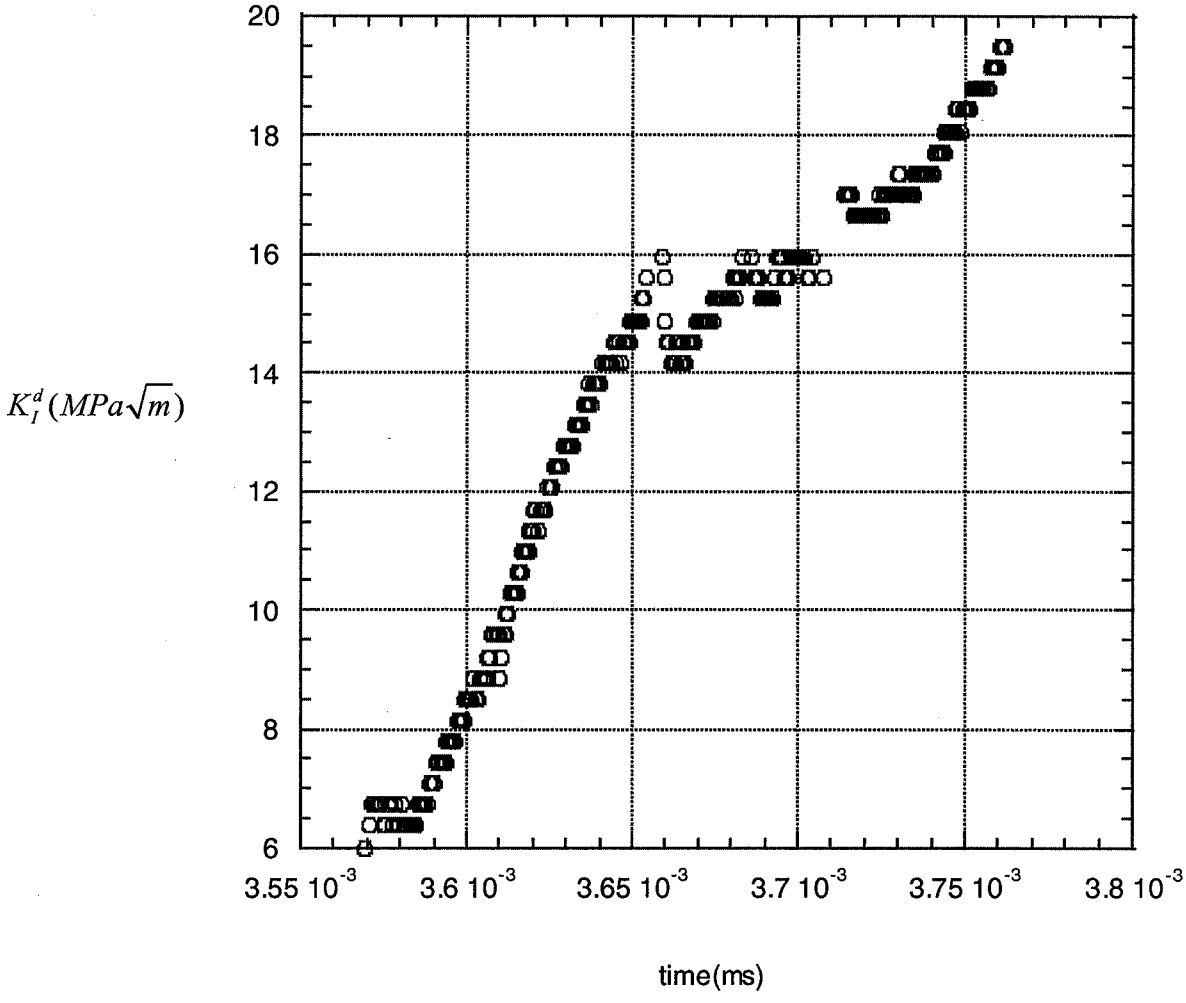
$K_I^d(MPa\sqrt{m})$
20
18
16
14
12
10
8
6
3.55 10^-3
3.6 10^-3
3.65 10^-3
3.7 10^-3
3.75 10^-3
3.8 10^-3
time(ms)

Figure 12

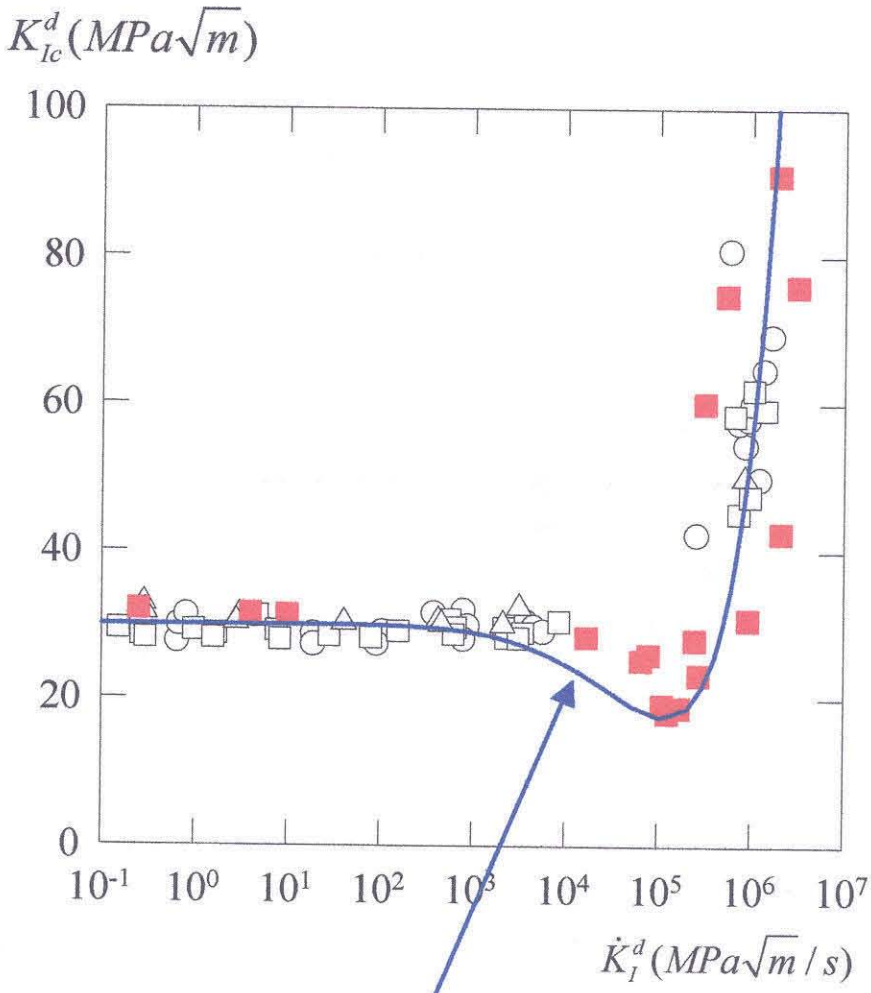

$$K_{Ic}^{d} = 50\left(\left[\frac{\log(\dot{K}^{d})}{5.7}\right]^{12} - \left[\frac{\log(\dot{K}^{d})}{5.7}\right]^{6}\right) + 30$$

Figure 13

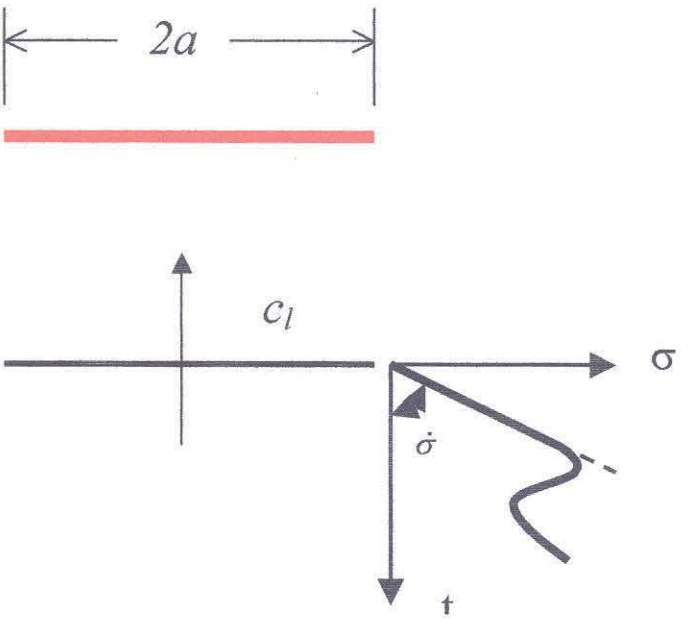

Figure 14

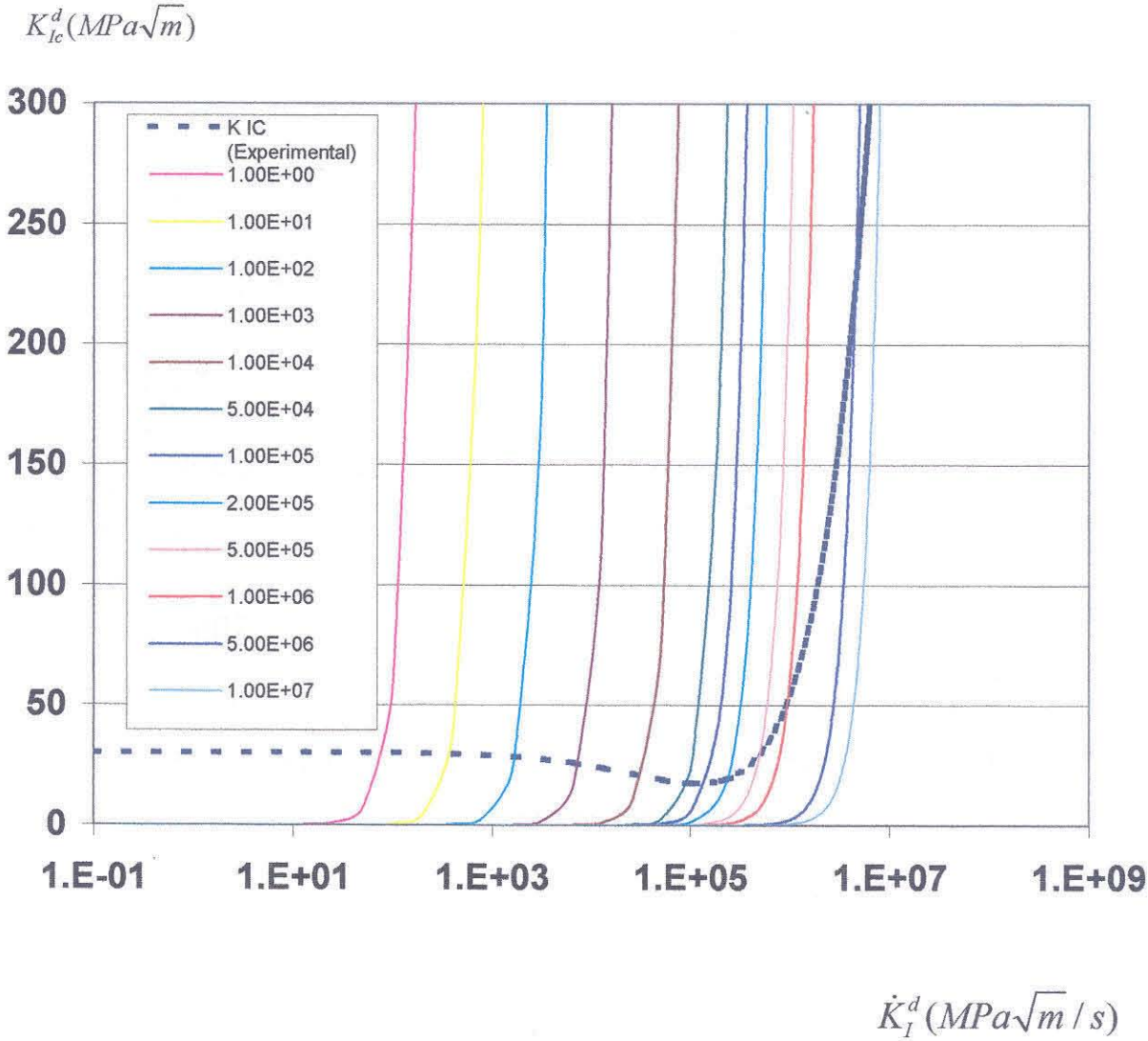
$K_{Ic}^{d}(MPa\sqrt{m})$
300
250
200
150
100
50
0
K IC (Experimental)
1.00E+00
1.00E+01
1.00E+02
1.00E+03
1.00E+04
5.00E+04
1.00E+05
2.00E+05
5.00E+05
1.00E+06
5.00E+06
1.00E+07
1.E-01
1.E+01
1.E+03
1.E+05
1.E+07
1.E+09
$\dot{K}_{I}^{d}(MPa\sqrt{m}/s)$

Figure 15

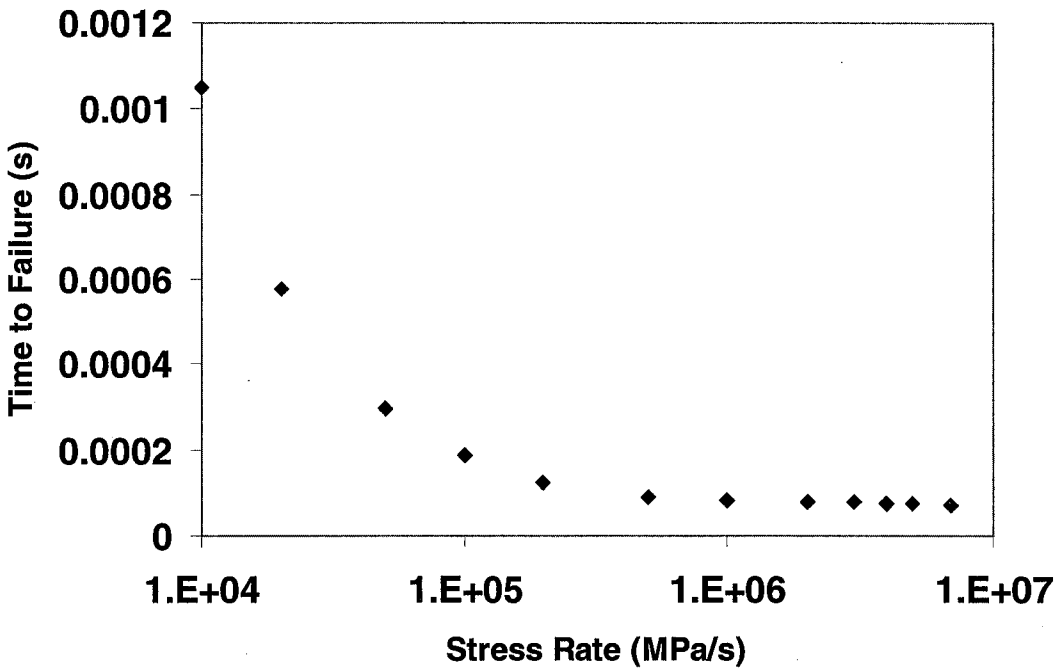
0.0012
0.001
0.0008
0.0006
0.0004
0.0002
0
Time to Failure (s)
1.E+04
1.E+05
1.E+06
1.E+07
Stress Rate (MPa/s)

Figure 16

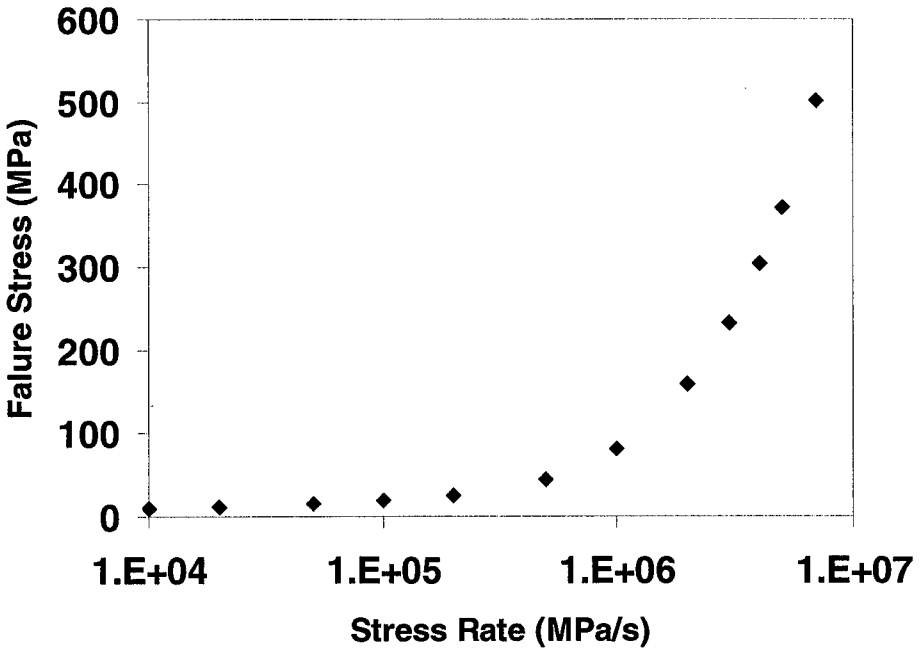
600
500
400
300
200
100
0
Falure Stress (MPa)
1.E+04
1.E+05
1.E+06
1.E+07
Stress Rate (MPa/s)

Figure 17

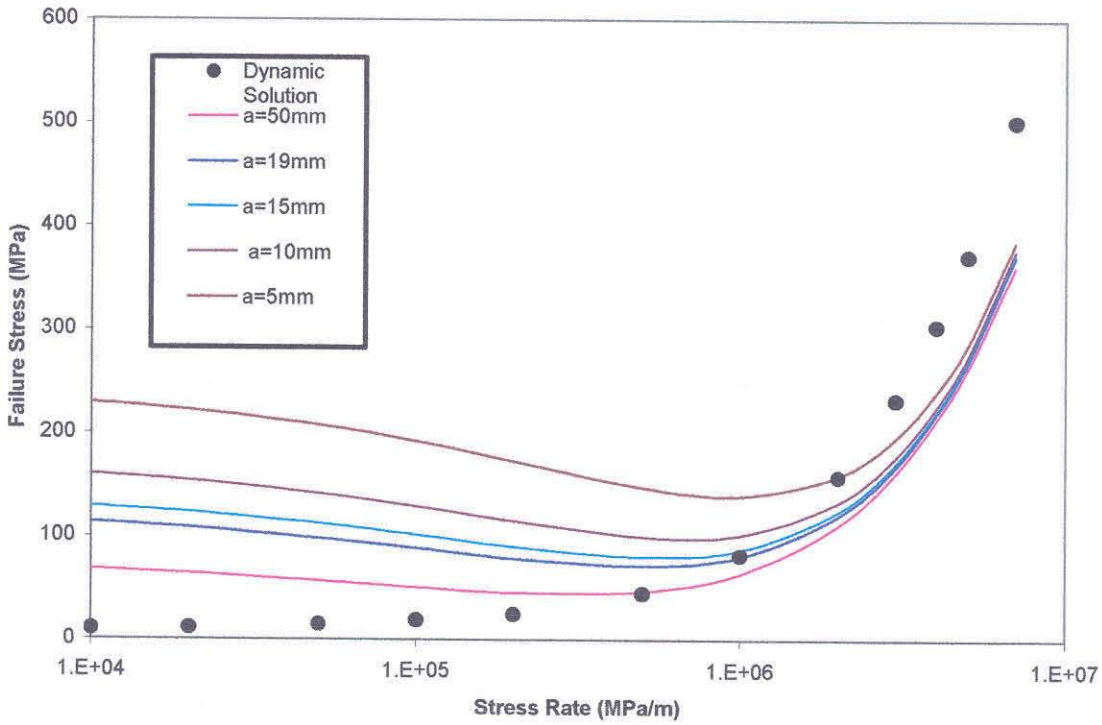
600
500
400
300
200
100
0
Failure Stress (MPa)
Dynamic Solution
a=50mm
a=19mm
a=15mm
a=10mm
a=5mm
1.E+04
1.E+05
1.E+06
1.E+07
Stress Rate (MPa/m)

Figure 18

Chapter 2

A Dynamic Fracture Mechanics Approach to the Estimation of Residual Strength of Impulsively Loaded Structures: Part II: Application to Explosively Loaded Aircraft Fuselage

Abstract

A dynamic fracture mechanics based approach for prediction of the residual strength of structures with applications to explosively loaded aircraft fuselage is introduced. Global structural analysis is conducted, coupled with local finite element analysis that includes the capability of addressing issues related to dynamic fracture mechanics. Local finite element calculations were performed for different loading rates, $\dot{\sigma}$, ranging from $1\times10^{5} MPa/s$ to $1\times10^{8} MPa/s$ to simulate the conditions encountered in an explosively-loaded aircraft fuselage. Simulations were conducted at a number of loading rates for the following cases of relevance to aircraft fuselage: (i) center cracked panels, (ii) rivet holes with wing cracks, (iii) biaxially loaded panels and (iv) panels pre-stressed to simulate pressurization. The results from the analyses were then used in conjunction with the experimental results for the dynamic fracture toughness of a 2024-T3 aluminum alloy as a function of loading rate, K_{IC}^{d} vs. $\dot{K}^{d}(t)$, to determine the time to failure, t_f, for a given loading rate. A failure envelope, σ_f vs. $\dot{\sigma}$, based on the failure model and finite element analysis is presented for the different cases and its implications for the residual strength of aircraft structures is discussed.

2.1 Introduction

Explosive or detonation loading due to accidents or threats can produce extensive structural damage to aircraft structures resulting in substantial loss of their load bearing ability and flight control (Kanninen and O'Donoghue, 1995). In order to understand the behavior and the residual strength of the overall aircraft structure subjected to such loading conditions, one needs to investigate the failure behavior of structural materials under correspondingly high rates of loading. The loading rate for an explosively loaded aircraft can be as high as $50x10^6$ N/s (Kamoulakos, Chen, Mestreau & Lohner, 1996) with strain rates in the range of $10^6 - 10^7$/s (Meyers, 1994). Consider an aging commercial airplane, with multi-site damage (e.g., fatigue cracks) at the rivet holes, under blast loading as shown in Figure 1 (Kanninen and O'Donoghue, 1995). When such an aircraft structure is subjected to explosive dynamic loading, the cracks are loaded with very high loading rates. Under such transient loading conditions, these fatigue cracks can initiate and propagate rapidly. When many of these cracks coalesce, catastrophic failure can occur, resulting in loss of the functionality of the structure and rapid depressurization. This failure mode is highly possible under the blast loading condition, as illustrated in Figure 1a. Thus, a dynamic fracture mechanics based analysis can provide valuable insights into the dynamic initiation of fatigue cracks in aging airplaneS under blast loading due to explosives.

Conventional analyses of failure in full-scale structures subjected to explosive loading often utilize ad-hoc failure criteria based on the attainment of critical levels of

stress corresponding to failure initiation. Such critical stress levels are often arbitrarily chosen to be some fraction of the yield stress and are assumed to be uniform throughout the structure, irrespective of the rate of loading experienced at different locations. In the present work, basic concepts of dynamic fracture mechanics are used to examine, rationalize and refine this ad-hoc, yet simple approach. In order to achieve this, a detailed analytical model based on the fracture behavior at high rates of loading is needed. The methodology presented here for the prediction of residual strength of aircraft structures is based on a combined global/local computational approach combined with experimentally determined dynamic fracture resistance of the structural material. The problem formulation and the background for the current study are provided in Section 2.2 and as well as the methodology to arrive at the failure criteria. Detailed description of the finite element analysis procedure is presented and the results from different local geometrical configurations and loading conditions are summarized in Section 2.3. The chapter concludes with the implications of the present approach in determining the residual strength of dynamically loaded aircraft structures and provides validation for the empirical approach currently used in the aircraft industry.

2.2 Problem Formulation

The problem of an aircraft fuselage structure subjected to explosive loading is analyzed in two stages. First, the resultant "global" structural loads due to the explosive loading at different locations are obtained using fluid-structure interaction codes, PAM-FLOW and PAM-SHOCK. Next, the resultant loads from the global analyses applied as

boundary conditions of a panel with simulated pre-fatigued cracks present as the result of flight service loads (pressurization – depressurization cycles) using a special purpose finite element code, FEAP-DYNA. The "local" analysis of these panels involves computing dynamic stress intensity factors as a function of time and comparing them with experimentally determined fracture parameters to establish the critical conditions for crack initiation.

A typical fuselage section of a wide body commercial airliner is simulated in the global analysis. The length of this section is about 6.6 m, while the radius is 1.8 m. The full-scale fuselage is subdivided into smaller elements containing pre-existing fatigue cracks emanating from rivet holes. Figure 2 presents a typical global finite element mesh for this section of the fuselage structure. A typical element from the global finite element analysis is then used as the subject of the local finite element analysis. The element is subjected to transient loads from the global stress analysis. The local dynamic fracture problem is then solved numerically, and when possible, analytically, and the resulting time histories of dynamic stress intensity factor are obtained for different fuselage locations. These time variations are compared to the dynamic fracture toughness of the material obtained from the experimental studies to determine critical conditions for crack initiation. Experimental data for the dependence of fracture toughness of the typical aircraft fuselage material, 2024-T3 aluminum alloy, on loading rate, presented in Chapter 1, are utilized. This comparison determines the times and critical stress levels for crack initiation as a function of loading rate.

The local analysis is carried out using a two-dimensional finite element analysis program (FEAP-DYNA) incorporating implicit dynamics. This is used to model the stress wave loading of the panels with pre-existing fatigue cracks. This special purpose finite element program has the unique capability to compute the dynamic energy release rate (dynamic J integral), J^d, using a domain integral method (Nakamura et al. (1986)). The dynamic stress intensity factor, K^d, was computed from the calculated value of the dynamic J^d integral at each time step.

The model size chosen for the local numerical simulations was based on the typical element size used in the global fluid-structure code used for estimating blast loads from an explosion in the cargo hold area of the model aircraft shown in Figure 3. The panel sizes used in the simulation are 127 mm (5") wide and 102 mm (4") high, with a central crack of 19 mm (0.75") parallel to the wider side. Due to symmetry of the panel, only one quarter of the model panel was simulated. From the global stress histories provided by Boeing, the range of stress rate of loading on the model panel was estimated. The plates were assumed to be in plane stress, which accurately reflects the stress state in a fuselage panel. The crack size was chosen based on the worst-case scenario of fatigue cracks near rivet holes. The loading rates are expected to be very high in the vicinity of the blast site ($10^9\ MPa/s$) and continue to decrease away from the blast site, to about $10^4\ MPa/s$.

From the local simulations, the time history of the dynamic energy release rate, J^d, and hence the dynamic stress intensity factor, K^d, were obtained for various loading

rates. The loading rates were varied by prescribing the appropriate time history of tractions at the boundaries of the model panel (Figure 3). The stress intensity factor history was differentiated numerically with respect to time to obtain the stress intensification rate, $\dot{K}$, as a function of time. These results are used to construct the driving force (K vs. $\dot{K}$) curve and are plotted together with the experimentally obtained material response curve for 2024-T3 aluminum alloy in Chapter 1. The intersection between these two curves provides the critical dynamic stress intensity factor or the fracture toughness for that particular loading rate. The time for crack initiation (failure), t_f, for a given stress rate, $\dot{\sigma}$, is obtained from the values of the critical stress intensity factor and the knowledge of the time history of the stress intensity factor for that rate. Once the time to fracture is established for a given a stress rate, the critical failure stress, σ_f, can be obtained from their product, i.e., stress rate and the failure time, $\dot{\sigma}t_f$. Thus, one will be able to arrive at a simple failure criterion in terms of σ_f and $\dot{\sigma}$, which is based on principles dynamic fracture mechanics. A quantity of utmost engineering importance in the design and analysis of aerospace structures is *their residual strength subsequent to explosive or detonation loading.* The critical failure stress, σ_f, can be viewed as a reasonable measure of the residual strength of the materials of the structures.

2.3 Finite Element Analysis

As mentioned in the previous section, the finite element analysis is carried out in two parts: a global analysis and a local analysis. The methodologies used for each

analysis are outlined in this section. The details of how the local finite element analysis uses the output of the global finite element analysis is also presented.

2.3.1 GLOBAL FINITE ELEMENT ANALYSIS

The global finite element analysis was carried out by Chen and co-workers at Boeing Phantom Works in Long Beach, California. The analysis was carried out to simulate the structural response of a section of the model aircraft fuselage structure (Figure 2) under the blast loading of a certain size of explosive. In this section, the basic methodology used by Chen at Boeing is presented. For a detailed description of the analysis and the capabilities of the finite element programs used in the analysis, one should refer to report by Chen.

The finite element programs used for the global analysis are PAM-SHOCK and PAM-FLOW by ESI Corporation in France. The approach taken to conduct the simulation is to couple these two finite element codes, a structural code (PAM-SHOCK) for the structural part, and a fluids code (PAM-FLOW) for the cabin air response modeling. A coupled simulation requires two meshes: one for the fluid and one for the structure. Transfer interpolation routines are used to take care of any size discrepancies between the two meshes at the interface. They can be non-matching and have very different element sizes.

PAM-FLOW is an explicit finite element code, based on tetrahedral, that solves the compressible Euler and Navier-Stokes equations. Several numerical schemes are

available for shock propagation analysis: central difference, upwind Roe and Van Leer and flux corrected transport. PAM-SHOCK is an explicit finite element code dedicated to shock wave propagation and subsequent response of complex structures.

In the present global simulation, a pressurized section of the fuselage is used to model a wide-body airplane under explosive loading. The length of this section is about 6.6 meters and its radius is around 1.8 meters. The material properties used for the fuselage skin are those of 2024-T3 aluminum alloy, widely used in aircraft construction. The material properties of 2024-T3 aluminum are as follows: Young's modulus $E = 72\ GPa$, Poisson's ratio $\nu = 0.33$ and yield stress $\sigma_o = 350\ MPa$. The fuselage section is modeled with as much detail as possible with cabin floor, cargo floor, frames, longerons and rivets. The dimensions of the features used resemble those of an actual wide-body commercial airplane. The complexity of the fuselage is modeled in order to closely simulate of an actual aircraft structure.

In order to model a section of the fuselage under explosive loading, the following simulations take place in sequence. First, the simulation of detonation and burn of the explosive was conducted. The explosion and blast wave creation is performed by an axisymmetric analysis, in this case with PAM-SHOCK2D. For a given explosive, the analysis has to be performed once and the results obtained can be used with different structures as initial conditions to the fluids code -- PAM-FLOW. For this simulation, a bare-charge of 225 grams (0.5 lb) spherical C4 explosive mass is used. The general properties for the C4 explosive are as follows: density =1.601 gram/cm^3, detonation

pressure (Chapman-Jouget) = 0.281 Mbar, detonation velocity = 0.804 cm/μs and initial explosion energy density = 0.087 Mbar/cm^3. Figure 5 shows a picture of the modeled explosive and surrounding air. Due to symmetry, only a wedge is shown. Second, the expansion of the gases and deformation of the blast wave is simulated with PAM-FLOW using the initial condition from the blast wave creation described above. This is done in a pressurized medium (1.5 bar) to simulate the internal pressure of the fuselage. The density of air is 0.0019395 gram/cm^3 for this corresponding pressure.

The next step is to simulate the interaction of the expanding blast wave with the complex fuselage geometry. This is done by coupling PAM-FLOW and PAM-SHOCK through the use of a restart file. The state variables such as pressure, displacement, velocity and acceleration are passed for each time interval between the fluid and structure programs though the use of restart files. The response of the structure is then carried out for each time step. The three expected structural responses of the fuselage section are as follows: high acceleration imposed upon the skin at the footprint of the explosion, possible subsequent separation of the skin from the frames and longerons leading to failure of the skin and subsequent venting. The global structural analysis provides the time histories of loading at various locations in the fuselage which form the basis of input for the local analysis described in the next section.

2.3.2 LOCAL FINITE ELEMENT ANALYSIS

Local finite element analysis was conducted on a typical element from the global finite element analysis along with the structural response of the global finite element program as boundary conditions. For this local analysis, a modified version of the finite element program FEAP is used. FEAP was first developed by Professor R.L. Taylor from the Civil Engineering Department at UC Berkeley. The version of FEAP used in this analysis was modified to incorporate the capability of conducting dynamic fracture mechanics calculations (e.g., Tippur et al. 1991).

For this local finite element analysis, various configurations that closely resemble different scenarios of the aircraft fuselage with damage are used. First, a center-cracked panel under uniaxial loading was investigated. Then the effects of the rivet hole with winged cracks was studied. Different ratios of the rivet hole diameter to crack length were used to study the effect of crack length which arises as a result of widespread multi-site fatigue damage (Kanninen, 1995). Biaxial loading situations were also studied to simulate the loading on an aircraft panel due to the hoop stress and the longitudinal loading conditions in a cylindrical structure. Lastly, a constant pre-stress is applied on the panel which simulates the static cabin pressure for a pressurized fuselage prior to the imposed dynamic loading.

A typical element from the global code is 127 mm (5") wide and 102 mm (4") high with a central crack of 19 mm (0.75") parallel to the wider side. The crack length chosen here for the simulations is approximately four times the rivet hole diameter (3/16''). Only a quarter of this panel is modeled in the local analysis due to symmetry of

applied loading. Two dimensional plane stress analysis is conducted on the panel using FEAP. This is a good approximation of the state of stress in the curved shell panels of the aircraft fuselage. The panel is meshed using 4 node quadrilateral elements with a finely (logarithmically) graded mesh in the vicinity of the crack and a coarse mesh away from the crack tip. The boundary conditions prescribed for the analysis are the stress histories from the global finite element analysis. Figure 6 shows the time history of stress components for one typical element in the global finite element analysis taken at a location 1 m away from the blast site. Both the hoop stress and the longitudinal stresses are plotted in the figure. The larger stress component (hoop stress) is applied in the perpendicular direction to the crack in the local analysis. In the biaxial analysis, the longitudinal stress is applied parallel to the crack direction.

As one can see from Figure 6, stress vs. time data from the global analysis can be roughly approximated as linear in the initial part of the loading curve. Hence, a corresponding idealized loading curve is used in the local analysis (constant stress rate) and is shown in Figure 7. By making use of this observed linear behavior of the stress history (Figure 6), the prescribed stress boundary conditions for the local finite element analysis can be idealized (Figure 7). Hence, without applying the actual loading history, the local analysis can be conducted for a variety of loading rates in addition to those obtained from the global analysis. By doing so, a wide range of stress rates to be used in the development of a failure stress criteria can be investigated. In the current study, the constant stress rates that are used are in the range of $10^5\ MPa/s$ to $10^8\ MPa/s$.

The goal of the local finite element analyses is to obtain the dynamic J integral as a function of time for the different loading rates that correspond to those experienced at different locations in the aircraft fuselage. From the dynamic J integral obtained, one can calculate the dynamic stress intensity factor, $K_I^d(t)$, which can then be used to obtain a dynamic fracture mechanics based failure criteria. For a two dimensional body containing a crack subjected to dynamic loading, the energy release rate can be expressed as the following:

$$G = \lim_{\Gamma \to 0} \int_{\Gamma} [(U + T)n_1 - \sigma_{ij} n_j \frac{\partial u_i}{\partial x_1}] d\Gamma , \qquad (1)$$

where U is the stress work density, T is the kinetic energy density, u is the displacement, Γ is the contour surrounding the crack tip, n_i are components of the outward unit normal vector to the contour and σ is the stress tensor (Freund, 1990).

The stress work density, U, and the kinetic energy density, T, can be written as:

$$\int_0^{\varepsilon} \sigma_{ij} d\varepsilon_{ij} = \int_0^{t'} \sigma_{ij} \frac{\partial^2 u_1}{\partial t' \partial x_j} dt' ; \qquad T = \frac{1}{2} \rho \frac{\partial u_i}{\partial t} \frac{\partial u_i}{\partial t} . \qquad (2)$$

For the case of a stationary crack under dynamic loading conditions, the kinetic energy should be bounded near the crack tip. Therefore, Eq. (1) can be rewritten as:

$$G = J = \lim_{\Gamma \to 0} \int_{\Gamma} [Un_1 - \sigma_{ij} n_j \frac{\partial u_i}{\partial x_1}] d\Gamma \tag{3}$$

The above integral needs to be evaluated as $\Gamma \to 0$, which makes it unsuitable for discrete computations. In order to calculate the J integral, a virtual crack extension method developed by Li et al. (1985) is used to transfer the contour integral to a finite domain integral. In Figure 8, for a 2-D problem, the area A enclosed by contour Γ and Γ_0 is shown near the crack tip. A weighting function, $f(x_1, x_2)$, an arbitrary smooth function having the values between 0 and 1 within area A and $f(x_1, x_2)$ is 1 and 0 on Γ and Γ_0 respectively, is used.

Therefore for a weighting function, *f*, with the characteristics described in Eq. (3) can be represented by a line integral over the closed contour C, which includes Γ, Γ_0 and the crack surface:

$$J = \lim_{\Gamma \to 0} \int_C (\sigma_{ij} m_j - U m_1) f dC \tag{4}$$

For this equation, m represent the outward unit vector normal to C (Figure 8). By applying the divergence theorem to Eq. (4) and using the equation of motion, the J integral takes the following form:

$$J = \int_A [\sigma_{ij} \frac{\partial u_i}{\partial x_1} \frac{\partial f}{\partial x_j} - U \frac{\partial f}{\partial x_1} + \rho \frac{\partial^2 u_i}{\partial t^2} \frac{\partial u_i}{\partial x_1} f] dA \,. \tag{5}$$

For numerical computation of J within the finite element framework, the discrete form of (5) is used with 2x2 Gaussian quadrature. The discrete form of Eq. (5) is as follows:

$$J = \sum_{\text{all elements in } A} \sum_{p=1}^{4} \left\{ \left[\sigma_{ij} \frac{\partial u_i}{\partial x_1} \frac{\partial f}{\partial x_j} - U \frac{\partial f}{\partial x_1} + \rho \frac{\partial^2 u_i}{\partial t^2} \frac{\partial u_i}{\partial x_1} f \right] \det \left[\frac{\partial x_k}{\partial \eta_k} \right] \right\}_p w_p . \quad (6)$$

All the field quantities and spatial derivatives are evaluated at the quadrature points for (p=1,2,3,4) and weighted by w_p. Similarly, f and $\partial f / \partial x_i$ at the quadrature points are evaluated:

$$f = \sum_{I=1}^{4} N_1 Q_{1I} \quad \frac{\partial f}{\partial x_i} = \sum_{I=1}^{4} \sum_{k=1}^{2} \frac{\partial N_1}{\partial \eta_k} \frac{\partial \eta_k}{\partial x_i} Q_{1I}, \quad (7)$$

where N_I is the bilinear shape function and Q_{II} is the value of f at the I^{th} node of an element.

Within FEAP, the contours used to enclose the domains for evaluating J can be both circular and rectangular. In the present analysis, the rectangular contours are used. The function f used for the analysis is a plateau function (Shih et al., 1985). In the current analysis, Eq. (6) is evaluated over several (up to 10) domains surrounding the crack tip, for every time step, corresponding to different areas, A, near the crack tip. The integral is calculated using a two-dimensional Simpson's rule and in general the variation in the computed values of J between different domains is less than 2%. The average

value J is computed and presented here. Finally, the dynamic stress intensity factor, K^d, is evaluated using its relation to the J integral. For plane stress,

$$J = \frac{\left(K_I^d\right)^2}{E}. \tag{8}$$

2.4 Results and Discussion

2.4.1 GLOBAL STRUCTURAL LOADS

The boundary conditions used in the local finite element analysis are from the global analysis in the form of stress vs. time. The stress history vs. time results for two such elements away from the blast site are shown in Figure 6 (Shell 8118) and Figure 9 (Shell 8512) from the global analysis. The stress history data consists of the hoop stress and longitudinal stress. The longitudinal stress is about 50% of the hoop stress, as expected for a thin wall cylindrical structure.

As shown in Figures. 6 and 9, the stress vs. time outputs are nearly linear in nature for a period of time ($\sim 150\ \mu s$) after stress waves arrive at the elements. For shell element 8118, the stresses start to increase around 0.2 ms after the explosion, and increase linearly until 0.35 ms. For shell element 8512, the stresses start to increase at around 0.17 ms and remain linear until 0.35 ms. The corresponding stress rate can be computed by simply taking two points on the linear portion of the curve and calculating

the slope of the curve. The hoop stress rates computed for shell element 8118 and 8512 are 1.9 MPa/μs and 1.88 MPa/μs, respectively.

Since the stresses calculated from PAM-Shock increase linearly with respect to time for the time of interest, one can utilize the linearity of the stresses to investigate a broad range of the stress rates. For the local finite element analysis using FEAP, stress rates ranging from $10^4\ MPa/s$ to $10^8\ MPa/s$ are used. By doing so, the effects of the crack subjected to explosive loading on the residual strength for a range of loading rates can be investigated.

2.4.2 CENTER CRACKED PANEL

A panel of the aircraft fuselage structure with a center crack subjected to a prescribed loading history is studied. The crack size (19 mm) used is 4 times of the diameter of a typical rivet (4.75 mm) used for the fuselage structure. Stress boundary conditions were prescribed at the outer edge of the panel. For the center cracked panel, the hoop stress is applied in the direction normal to the crack. A broad spectrum of loading rates is used as the boundary condition for the local analyses. The dynamic stress intensity factor, K_I^d, was computed as a function of time, t, using Eq. (8) for all loading rates, ranging from $10^4\ MPa/s$ to $10^8\ MPa/s$. Figure 10 shows K_I^d as a function of time for a loading rate $2\times10^6\ MPa/s$, which is the very close to the stress rate for shell element 8118 and 8152 in the PAM analysis. The K_I^d increases nearly linearly as a

function of time with slight deviation from linearity. By differentiating the K_I^d with respect to time, the dynamic stress intensity factor loading rate history, $\dot{K}_I^d$, as function of time is obtained. Figure 11 is the plot of $\dot{K}_I^d$ as a function of time for loading rate of $2\times10^6\ MPa/s$. As the plot shows, $\dot{K}_I^d$ increases rapidly for the first $30\mu s$, and eventually levels off at around $3\times10^5\ MPa\sqrt{m}/s$. A typical K_I^d vs. $\dot{K}_I^d$ is shown in Figure 12 for the stress rate of $2\times10^6\ MPa/s$. The K_I^d vs. $\dot{K}_I^d$ curve thus obtained numerically is then used to intersect the K_{IC}^d vs. $\dot{K}_I^d$ curve obtained experimentally in Chapter 1. K_{IC}^d is the critical value of dynamic stress intensity factor for crack initiation, i.e., dynamic crack initiation toughness. Figure 13 shows the intersection of numerically determined K_I^d vs. $\dot{K}_I^d$ from the current local analysis with the experimentally determined K_{IC}^d vs. $\dot{K}_I^d$ for loading rate $2\times10^6\ MPa/s$. The intersection determines the time to failure (initiation), t_f, for this particular loading rate to be 129 μs. Since the stress history is linear (constant stress rate $\dot{\sigma}$), one is able to calculate the failure stress for this particular loading rate simply by multiplying the loading rate, $\dot{\sigma}$, with the time to failure t_f.

$$\sigma_f = \dot{\sigma} t_f \tag{9}$$

By repeating the above procedure for all the loading rates of interest, a stress rate based failure criteria for this center-cracked panel can be deduced. The failure stress, σ_f, vs. time to failure, t_f, obtained using the above stated procedure is plotted in Figure

14 for the range of loading rates from $10^4\ MPa/s$ to $10^8\ MPa/s$. The corresponding failure stress, σ_f, vs. stress rate, $\dot{\sigma}$, is plotted in Figure 15. As shown in Figure 15, there is a drop in the failure stress for the range of loading rates between $10^5\ MPa/s$ and $10^6\ MPa/s$; the lowest level of stress for this geometry is 120 MPa at the stress rate of $10^5\ MPa/s$. For stress rates greater than $10^6\ MPa/s$, the failure stress, σ_f, increases as a function of applied stress rate, $\dot{\sigma}$. The yield stress for 2024-T3 aluminum alloy is 350 MPa. Thus, if one uses the yield stress of 350 MPa to design impulsively loaded aircraft structures, even a safety factor of 2 may prove to be insufficient.

2.4.3 EFFECT OF RIVET HOLES

In addition to the center-cracked panels, the effect of the rivet hole with different sizes of winged cracks on either side is also investigated. The overall dimension of the panel is the same as the one used in the center-cracked panel case. A typical central rivet hole (radius, R) of the size 4.76 mm (3/16 inches) is used in the analyses. Different wing crack lengths *a* are used with the ratios to the rivet radius of 0.2, 0.5 and 1. Again, only a quarter of the panel is modeled in the finite element analysis due to the symmetry of the problem. Figure 16 shows the typical FEAP mesh for a plate with a hole in the center. For the reduction of the data, similar procedures to those of the center-cracked panels (Section 2.4.2) are followed. Figure 17 shows the K_I^d as a function of time for all three crack lengths for the stress rate of $2\times10^6 MPa/s$. As shown in Figure 17, for all the cases considered here, the curves are fairly linear. The loading rates $\dot{K}_I^d$ for the

corresponding cases are plotted in Figure 18. The loading rates show characteristics similar to those for the center-cracked panel. The loading rate is the highest for the case *a/R=1* (a is the crack length and R is the radius of the rivet hole) and lowest for the smallest crack length to radius ratio *a/R=0.2.*

The failure stress, σ_f, vs. stress rate, $\dot{\sigma}$, is determined in the same manner as described for the case of center-cracked panel. The resultant failure stress as a function of stress rate is plotted for all three ratios of crack size to hole radius in Figure 19. The three curves follow the same pattern as the one for the center cracked panel, first a decrease for stress rate between $1\times10^6\ MPa/s$ and $5\times10^6\ MPa/s$, then increases dramatically beyond $\dot{\sigma} > 5\times10^6\ MPa/s$. Since the loading rate, $\dot{K}_I^d$, is slightly different for the three configurations, the minimum failure stress, σ_f, occurs at a different stress rate. For *a/R=0.5* and *a/R=1.0*, the lowest failure stress occurs at $1\times10^6 MPa/s$; while for *a/R=0.2*, the lowest failure stress occurs at $2\times10^6\ MPa/s$. The lowest level of failure stresses for the three configurations *a/R=0.2, 0.5* and *1.0* are 208, 215 and 176 MPa, respectively. As one would expect, the configuration with the longest crack has the smallest failure stress. But due to rate effects, the configuration with the smallest crack does not have the largest failure stress, since its lowest failure stress occurs at a different stress rate.

2.4.4 EFFECT OF BIAXIAL STRESS

In order to accurately simulate the loading scenarios of a cylindrical shell structure under both pressure induced hoop stress and longitudinal stress, biaxial loading conditions are imposed in the local finite element analysis. The rivet hole with a wing crack *a/R=1.0* configuration is used for the biaxial loading simulations. In accordance with the results from the global analysis (Figures. 6 and 9), the longitudinal stress imposed in a direction parallel to the crack is half of the hoop stress in all the cases. The numerically determined stress intensity factor, K_I^d, for both the biaxial and uniaxial loading conditions for stress rate $2\times10^6\ MPa/s$ are shown in Figure 20. The corresponding loading rate, $\dot{K}_I^d$, for both cases are shown in Figure 21. The loading rate for the biaxial loading case is slightly smaller than the one corresponding to the uniaxial case.

Following the same procedures described in previous sections, a stress rate based failure criteria is computed. Figure 22 compares the σ_f vs. $\dot{\sigma}$ data for biaxial and uniaxial loadings for the configuration of *a/R=1.0.* The minimum failure stress of *226 MPa* for the biaxial loading occurs at loading rate of $10^6\ MPa/s$. As shown in Figure 22, the global failure stresses are higher for the biaxial case in comparison to the uniaxial case for most of the stress rates. This is easily understood since the resultant stress normal to the crack in the biaxial case is lower near the crack tip region in comparison to the uniaxial case.

2.4.5 EFFECT OF STATIC PRE-STRESS

To simulate the effect of static cabin pressure for a commercial airliner, the addition of the static pre-stress is superposed on top of the dynamic biaxially loaded local simulations. Again, the configuration used for the static pre-stress analysis is the rivet hole with a wing crack, *a/R=1.0*. The dynamic stress intensity factor, K_I^d, and loading rate, $\dot{K}_I^d$, for the pre-stress and biaxial cases are very similar for most of the loading rates. Following the methods described in previous sections, Figure 23 compares the σ_f vs. $\dot{\sigma}$ failure criteria of the pre-stress, biaxial case to that of biaxial and uniaxial cases without pre-stress. The minimum failure stress for the pre-stress, biaxial case is *240 MPa* and occurs at $2\times10^6\ MPa/s$. As seen from Figure 23, the differences between the pre-stress, biaxial case and biaxial without pre-stress case are small for all the loading rates studied. The differences in the failure stresses can be attributed to the shift in loading rate, $\dot{K}_I^d$, and time to failure, t_f, caused by the inclusion of the pre-stress.

2.5. Conclusions

Detailed numerical simulations have been conducted using a combined global/local approach to study the residual strength of aircraft fuselage structure subjected to explosive loading. A methodology for predicting the residual strength of an aircraft structure utilizing the concept of dynamic fracture mechanics is developed. By combining the results from experimentally determined Mode I dynamic initiation toughness data with that of dynamic *J*-integral based numerical studies, a failure criteria in the form of failure stress, σ_f, vs. stress rate, $\dot{\sigma}$, is developed. This simple to use and

yet rigorous dynamic fracture mechanics based failure criteria can be customized to fit many different loading scenarios for structures subjected to transient loading.

In the present study, different local geometries or configurations of relevance to aircraft structures were used. A systematic approach was developed to get a step closer to accurately simulating an aircraft fuselage structure under explosive loading by refinement of the geometrical and loading configurations. Local analyses have been conducted for center-cracked panels and rivet holes with different size winged cracks subjected to dynamic, biaxial loading and static pre-stress. In each of these analyses, a failure stress, σ_f, vs. stress rate, $\dot{\sigma}$, envelope has been determined. It is found that for most cases, there is a decrease in failure stress for loading rates between $1\times10^6\ MPa/s$ and $5\times10^6\ MPa/s$. This decrease in the failure stress is due the decrease in dynamic crack initiation toughness between loading rates of $1\times10^4\ MPa\sqrt{m}/s$ to $1\times10^6\ MPa\sqrt{m}/s$ (Chapter 1, Figure 13). The lowest failure stress found for the case of a center-cracked panel is *120 MPa,* which is barely one-third of the yield stress for the material studied, 2024-T3 aluminum alloy, which is widely used in constructing commercial aircraft fuselage. This illustrates that using static material properties to design for dynamic loading conditions sometimes can be non-conservative and even dangerous, possibly leading to catastrophe.

For loading rates higher than $5\times10^6\ MPa/s$, a rapid increase in failure (residual) strength with increasing loading rate is observed. This strengthening can be attributed to

the considerable increase in dynamic crack initiation toughness (K_{IC}^{d}) at higher loading rates ($\dot{K}_{I}^{d} > 1\times10^{6}\ MPa\sqrt{m}/s$) (Chapter 1, Figure 13). The higher stress rates are experienced in the vicinity of the blast site. This increase in residual strength can result in loading induced *self hardening* of aircraft structures near the location of the explosion. This might help to explain other dominant failure modes shown in Figure 1 that causes the fuselage structure to fail in modes other than the tearing of the skin near the blast site.

References

Basu S, Narasimhan R, A comparative study of dynamic, ductile fracture initiation in two specimen configurations. *International Journal of Fracture* 102 (2000), (4) 393-410

T.L. Anderson, *Fracture Mechanics*, CRC Press, Boston (1991).

J. Barnes and R.L. Peters, The challenge of commercial aircraft survivability. In *Aerospace America* (1992) pp. 55-56.

J.W. Dally, Dynamic photoelastic studies of fracture. *Experimental Mechanics* 19 (1979) 349-367.

J.W. Dally and J.R. Berger, The role electrical resistance strain gages in fracture research. In *Experimental Techniques in Fracture* (Edited by J.S. Epstein) VCH Publishers, Inc., New York (1993) pp. 1-39.

X. Deng and A.J. Rosakis, Dynamic crack propagation in elastic-perfectly plastic solids under plane stress conditions. *Journal of the Mechanics and Physics of Solids* 39 (1991) 683-722.

X. Deng and A.J. Rosakis, A finite element investigation of quasi-static and dynamic asymptotic crack tip fields in hardening elastic-plastic solids under plane stress - I. Crack

growth in linear hardening materials. *International Journal of Fracture* 57 (1992a) 291-308.

X. Deng and A.J. Rosakis, A finite element investigation of quasi-static and dynamic asymptotic crack tip fields in hardening elastic-plastic solids under plane stress - II. Crack growth in power-law hardening materials. *International Journal of Fracture* 58 (1992b) 137-156.

L.B. Freund and R. Clifton, On the uniqueness of plane elastodynamic solutions for running cracks. *Journal of Elasticity*, 4 (1974) 293-299.

L.B. Freund, J. Duffy and A.J. Rosakis, Dynamic fracture initiation in metals and preliminary results on the method of caustics for crack propagation measurements. ASME Paper No. 81-PVP-15 (1981).

L.B. Freund and A.S. Douglas, The Influence of Inertia on Elastic-Plastic Antiplane Shear Crack Growth. *Journal of the Mechanics and Physics of Solids* 30 (1982) 59-74.

L.B. Freund, *Dynamic Fracture Mechanics*, Cambridge University Press (1990).

G.R. Irwin, Crack extension force for a part-through crack in a plate. *Journal of Applied Mechanics* 29 (1962) 651-654.

A. Kamoulakos, V.L. Chen, E. Mestreau and R. Lohner, Finite element modelling of structure/fluid interaction in explosively loaded aircraft fuselage panels using pamshock/pamflow coupling. Presented at the Conference of on Spacecraft Structures, Materials and Mechanical Testing, ESA/CNES/DARA, Noordwijk, The Netherlands, (1996).

M.F. Kanninen and C.H. Popelar, *Advanced Fracture Mechanics*, Oxford University Press, New York (1985).

M.F. Kanninen and P.E. O'Donoghue, Research challenges arising from current and potential applications of dynamic fracture mechanics to the integrity of engineering structures. *International Journal of Solids and Structures*, 32 (1995) 2423-2445.

M. Kosai, A. Shimamoto, C.-T. Yu, A.S. Kobayashi and P. Tan, A biaxial test specimen for crack arrest studies. *Experimental Mechanics* 36 (1996) 277-283.

P.S. Lam and L.B. Freund, Analysis of dynamic growth of a tensile crack in an elastic-plastic material. *Journal of the Mechanics and Physics of Solids* 33 (1985) 153-167.

C. Liu, W.G. Knauss and A.J. Rosakis, Loading rates and the dynamic initiation toughness in brittle solids. *International Journal of Fracture* 90 (1998) 103-118.

H. Maigre and D. Rittel, Dynamic fracture detection using the force-displacement reciprocity: application to the compact compression specimen. *International Journal of Fracture* 73 (1995) 67-79.

M.A. Meyers, *Dynamic Behavior of Materials*, John-Wiley & Sons, New York (1994).

T. Nakamura, C.F. Shih and L.B. Freund, Analysis of Dynamically Loaded Three-Point-Bend Ductile Fracture Specimen. *Engineering Fracture Mechanics* 25 (1986) 323-339.

D.M. Owen, S.M. Zhung, A.J. Rosakis and G. Ravichandran, Experimental determination of dynamic crack initiation and propagation fracture toughness in thin aluminum sheets. *International Journal of Fracture* 90 (1998) 153-174.

K. Ravi-Chandar and W.G. Knauss, An experimental investigation into dynamic fracture: i. crack initiation and arrest. *International Journal of Fracture* 25 (1984) 247-262.

D. Rittel and H. Maigre, A study of mixed-mode dynamic crack initiation in PMMA. *Mechanics Research Communications* 23 (1996a) 475-481.

D. Rittel and H. Maigre, An investigation of dynamic crack initiation in PMMA. *Mechanics of Materials* 23 (1996b) 229-239.

A.J. Rosakis, J. Duffy, and L.B. Freund, The determination of the dynamic fracture toughness of aisi 4340 steel by the shadow spot method. *Journal of the Mechanics and Physics of Solids* 34 (1984) 443-460.

A.J. Rosakis, Two optical techniques sensitive to gradients of optical path difference: the method of caustics and the coherent gradient sensor (CGS). In: *Experimental Techniques in Fracture (Ed. Epstein, J.), VCH, New York,* 1993 327-425.

A.J. Rosakis and G. Ravichandran, Dynamic Failure mechanics. *International Journal of Solid and Structures* 37 (2000) 331-348.

C.F. Shih, Relationships between the *J*-integral and the crack opening displacement for stationary and extending cracks. *Journal of the Mechanics and Physics of Solids* 29 (1981) 305-326.

C.F. Shih, Tables of Hutchinson-Rice-Rosengren singular field quantities (1983).

H.V. Tippur, S. Krishnaswamy, and A.J. Rosakis. Optical mapping of crack tip deformations using the method of transmission and reflection coherent gradient sensing: a study of crack tip *k*-dominance. *International Journal of Fracture* 52 (1991) 91-117.

W. Tong and G. Ravichandran, Inertia effects on void growth in viscoplastic materials. *Journal of Applied Mechanics* 62 (1995) 633-639.

M.L. Wilson, R.H. Hawley, and J. Duffy, The effect of loading rate and temperature on fracture initiation in 1020 hot-rolled steel. *Engineering Fracture Mechanics* 13 (1980) 371-385.

A.T. Zehnder and A.J. Rosakis, Dynamic fracture initiation and propagation in 4340 steel under impact loading. *International Journal of Fracture* 43 (1990) 271-285.

List of figures

Figure 10. Dynamic stress intensity factor, K_I^d, as a function of time for stress loading rate $2\times10^6 MPa/s$ for the case of center-cracked panel.

Figure 11. Dynamic stress intensity factor loading rate, $\dot{K}_I^d$, as a function of time for loading rate $2\times10^6 MPa/s$ for the center-cracked panel.

Figure 12. Dynamic stress intensity factor, K_I^d, vs. loading rate, $\dot{K}_I^d$, for the stress rate of $2\times10^6 MPa/s$ for the center-cracked panel.

Figure 13. Intersection of numerically determined K_I^d vs. $\dot{K}_I^d$ with the experimentally determined K_c^d vs. $\dot{K}_I^d$ for loading rate $2\times10^6 MPa/s$.

Figure 14. Failure stress, σ_f, vs. time to failure, t_f, for the center-cracked panel.

Figure 15. Failure stress, σ_f, vs. stress rate, $\dot{\sigma}$, for the center-cracked panel.

Figure 16. Local finite element mesh for a plate with a rivet hole in the center with winged cracks.

Figure 17. Dynamic stress intensity factor, K_I^d, vs. loading rate, $\dot{K}_I^d$, for the stress rate of $2\times10^6 MPa/s$ for the panel with rivet hole and winged crack.

Figure 18. Loading rate, $\dot{K}_I^d$, as a function of time for loading rate $2\times10^6 MPa/s$ for the panel with rivet hole and winged crack.

Figure 19. Failure stress, σ_f, vs. stress rate, $\dot{\sigma}$, for the panel with rivet hole and winged crack.

Figure 20. Dynamic stress intensity factor, K_I^d, vs. loading rate, $\dot{K}_I^d$, for the stress rate of $2\times10^6 MPa/s$ for the panel with rivet hole and winged crack (*a/R=1.0*) subjected to dynamic bi-axial loading.

Figure 21. Loading rate, $\dot{K}_I^d$, as a function of time for loading rate $2\times10^6 MPa/s$ for the panel with rivet hole and winged crack (*a/R=1.0*) subjected to dynamic bi-axial loading.

Figure 22. Failure stress, σ_f, vs. stress rate, $\dot{\sigma}$, for the panel with rivet hole and winged crack (*a/R=1.0*) subjected to dynamic bi-axial loading.

Figure 23. Failure stress, σ_f, vs. stress rate, $\dot{\sigma}$, for the panel with rivet hole and winged crack (*a/R=1.0*) subjected to dynamic bi-axial loading and static pre-stress.

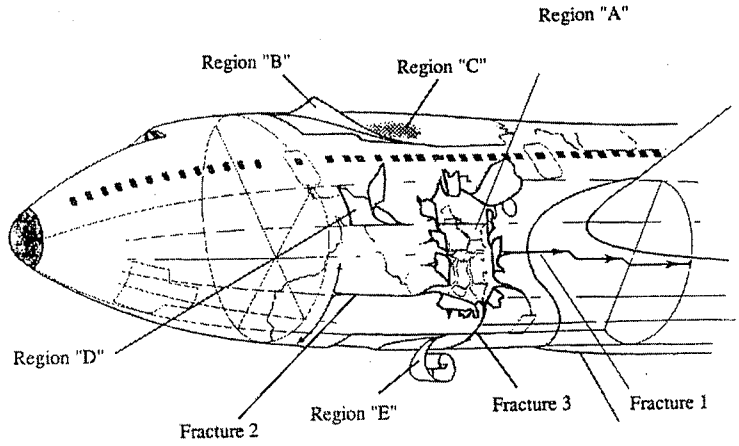
Region "A"
Region "B"
Region "C"
Region "D"
Fracture 2
Region "E"
Fracture 3
Fracture 1

Figure 1

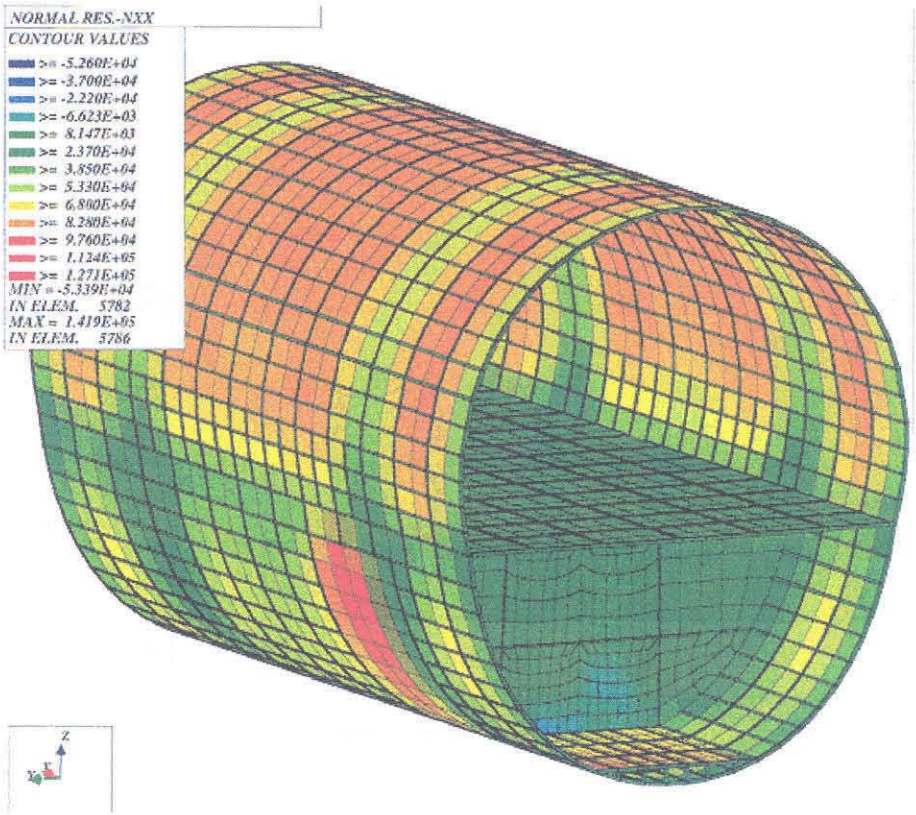
NORMAL RES.-NXX
CONTOUR VALUES
>= -5.260E+04
>= -3.700E+04
>= -2.220E+04
>= -6.623E+03
>= 8.147E+03
>= 2.370E+04
>= 3.850E+04
>= 5.330E+04
>= 6.890E+04
>= 8.280E+04
>= 9.760E+04
>= 1.124E+05
>= 1.271E+05
MIN = -5.339E+04
IN ELEM. 5782
MAX = 1.419E+05
IN ELEM. 5786
Z
Y
X

Figure 2

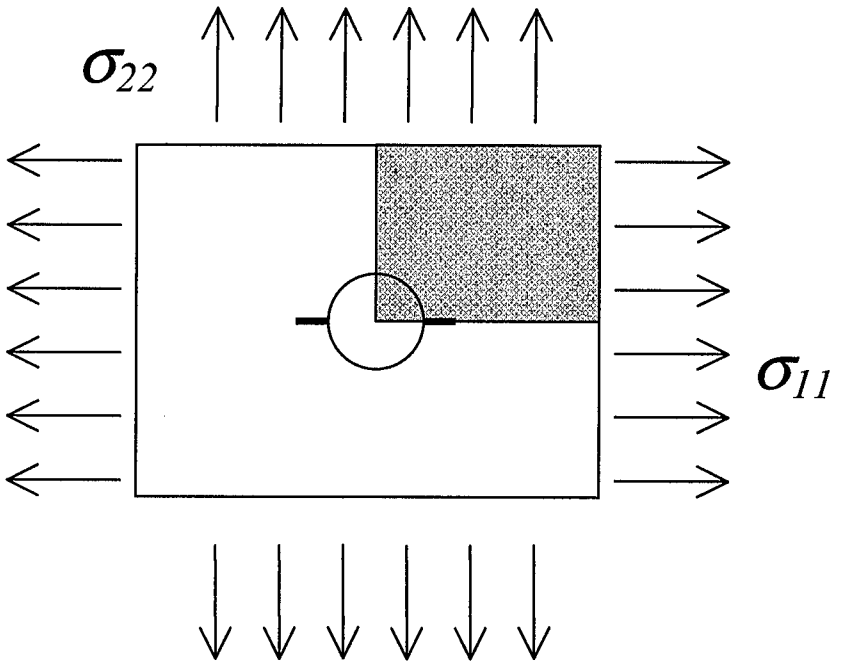

Figure 3

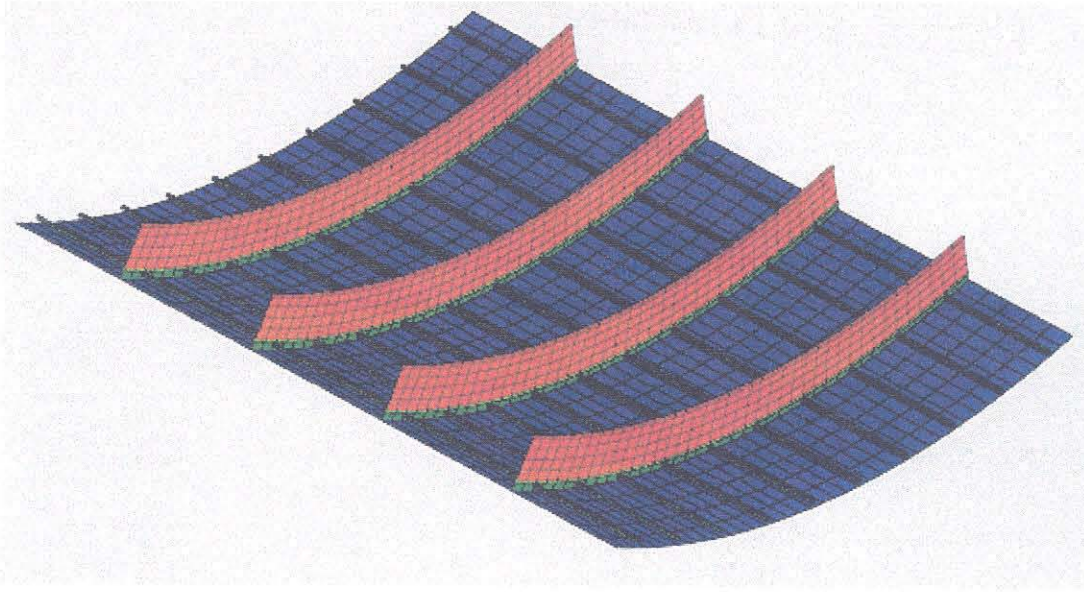

Figure 4

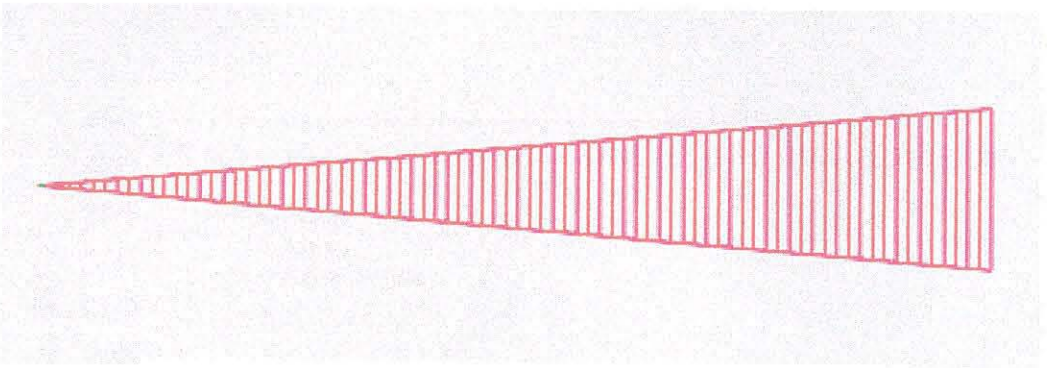

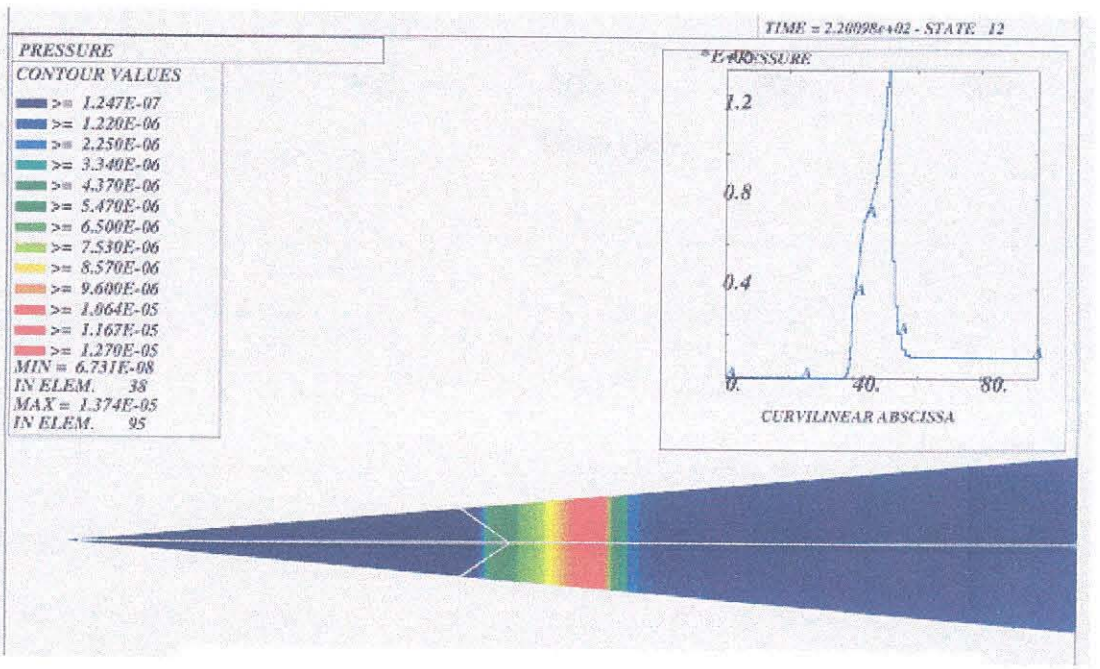
PRESSURE
CONTOUR VALUES
>= 1.247E-07
>= 1.220E-06
>= 2.250E-06
>= 3.340E-06
>= 4.370E-06
>= 5.470E-06
>= 6.500E-06
>= 7.530E-06
>= 8.570E-06
>= 9.600E-06
>= 1.864E-05
>= 1.167E-05
>= 1.270E-05
MIN = 6.731E-08
IN ELEM. 38
MAX = 1.374E-05
IN ELEM. 95
TIME = 2.26098e+02 - STATE 12
*E+00
1.2
0.8
0.4
0.
40.
80.
CURVILINEAR ABSCISSA

Figure 5

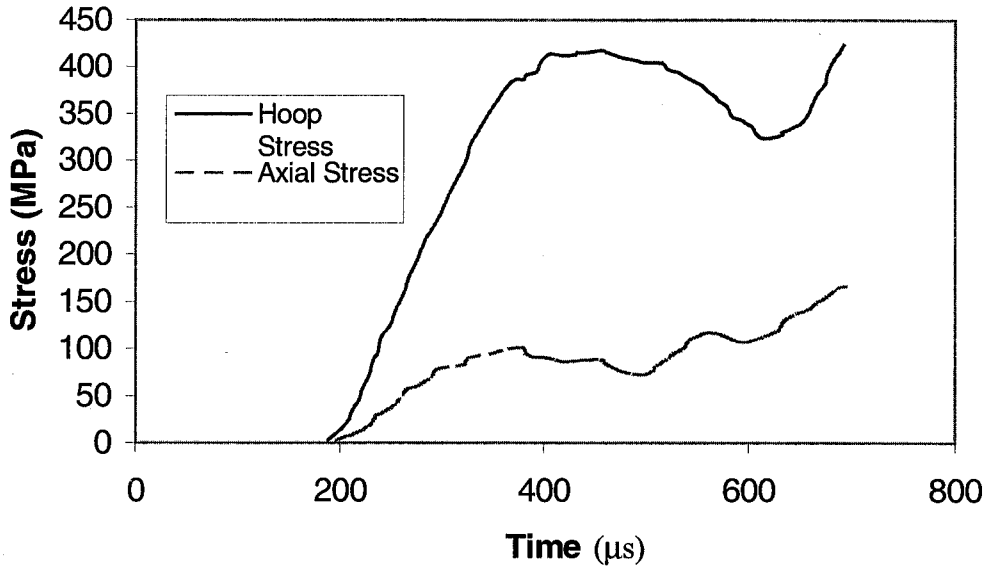
450
400
350
300
250
200
150
100
50
0
Stress (MPa)
Hoop Stress
Axial Stress
0
200
400
600
800
Time (μs)

Figure 6

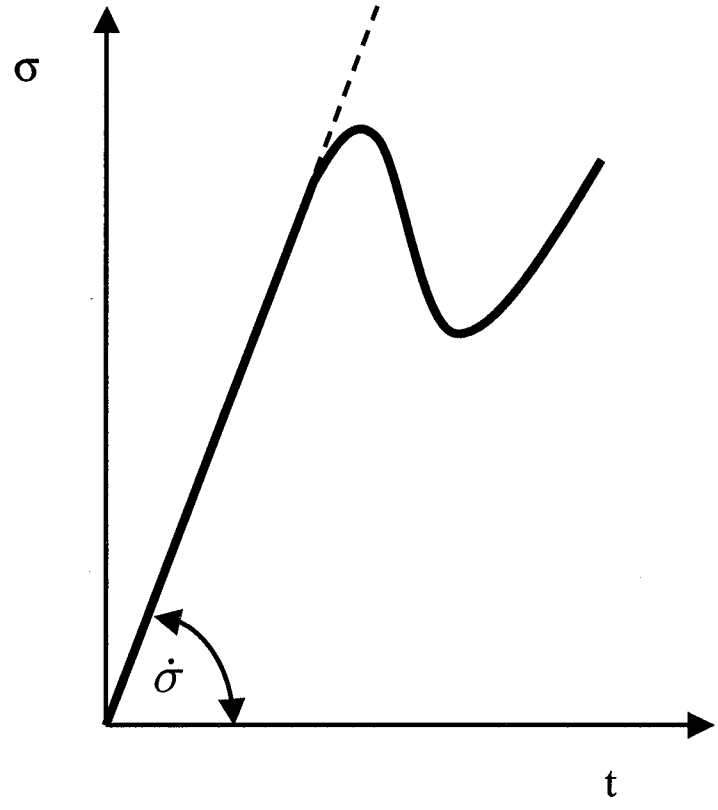

Figure 7

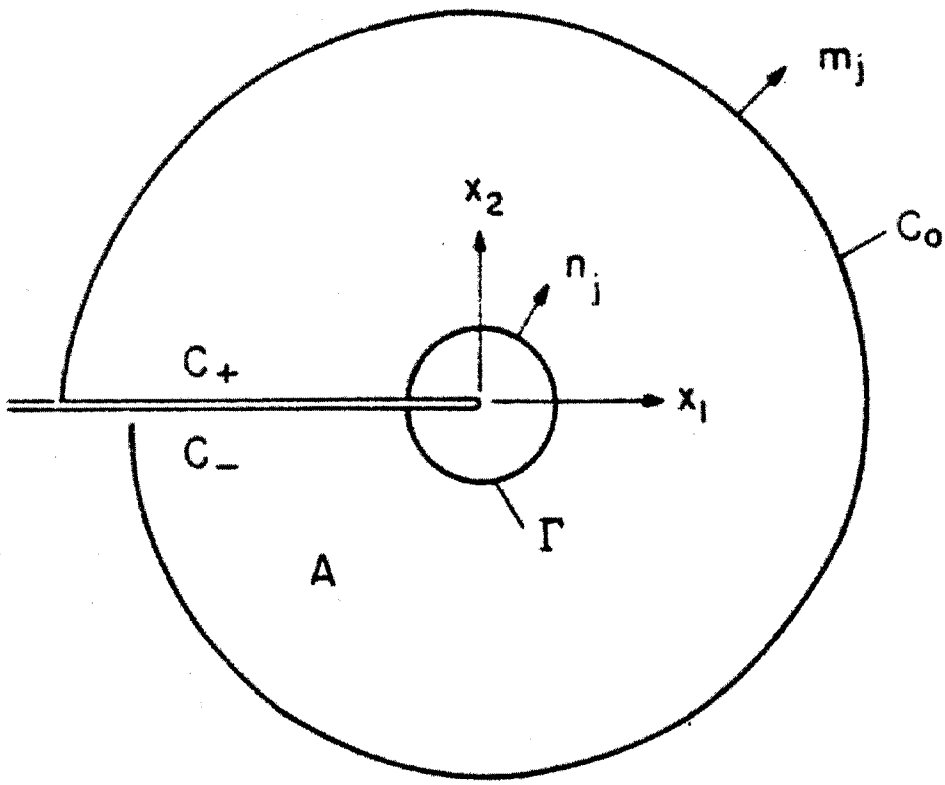

Figure 8

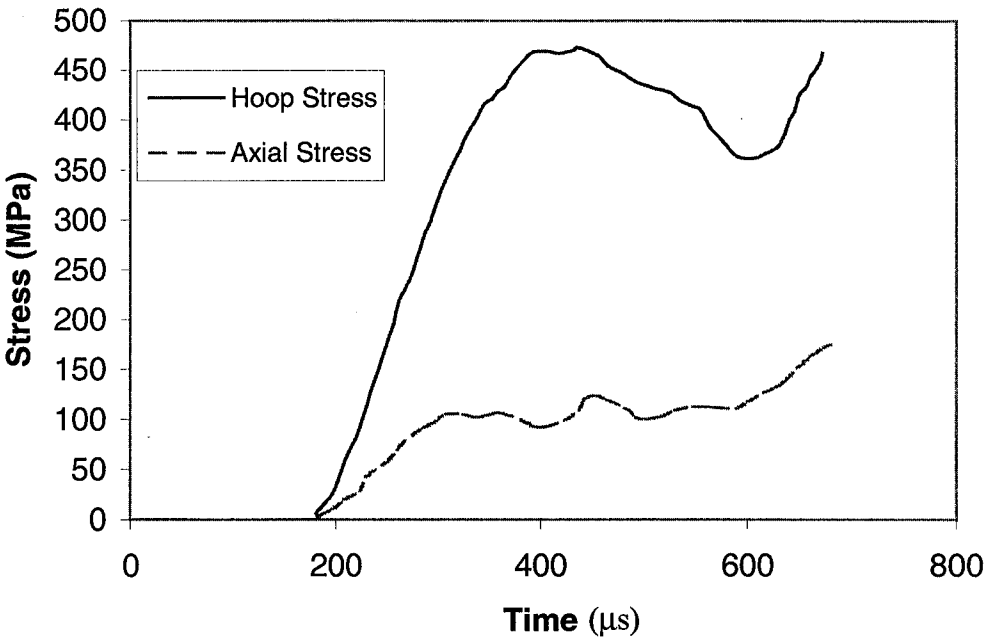
500
450
400
350
300
250
200
150
100
50
0
Stress (MPa)
Hoop Stress
Axial Stress
0
200
400
600
800
Time (μs)

Figure 9

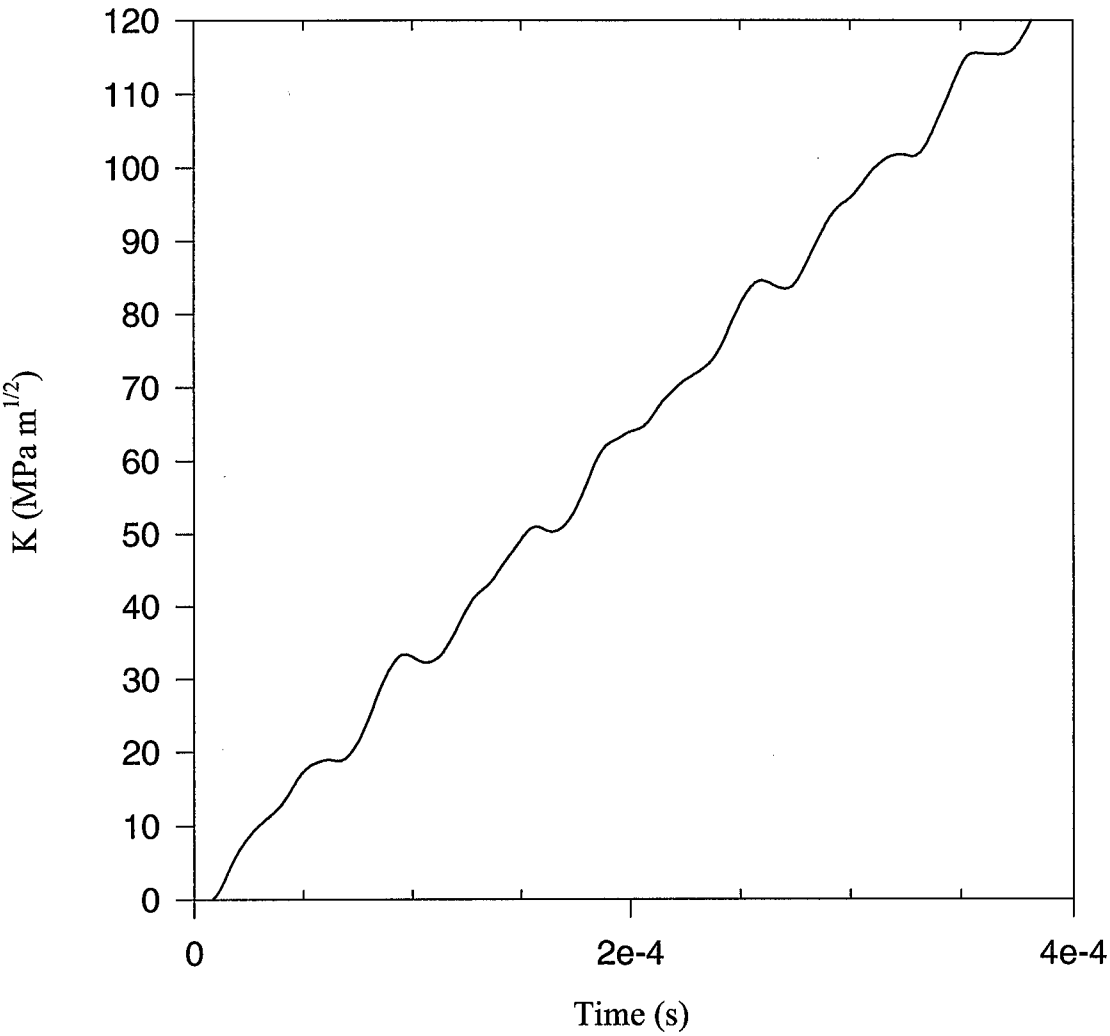

Figure 10

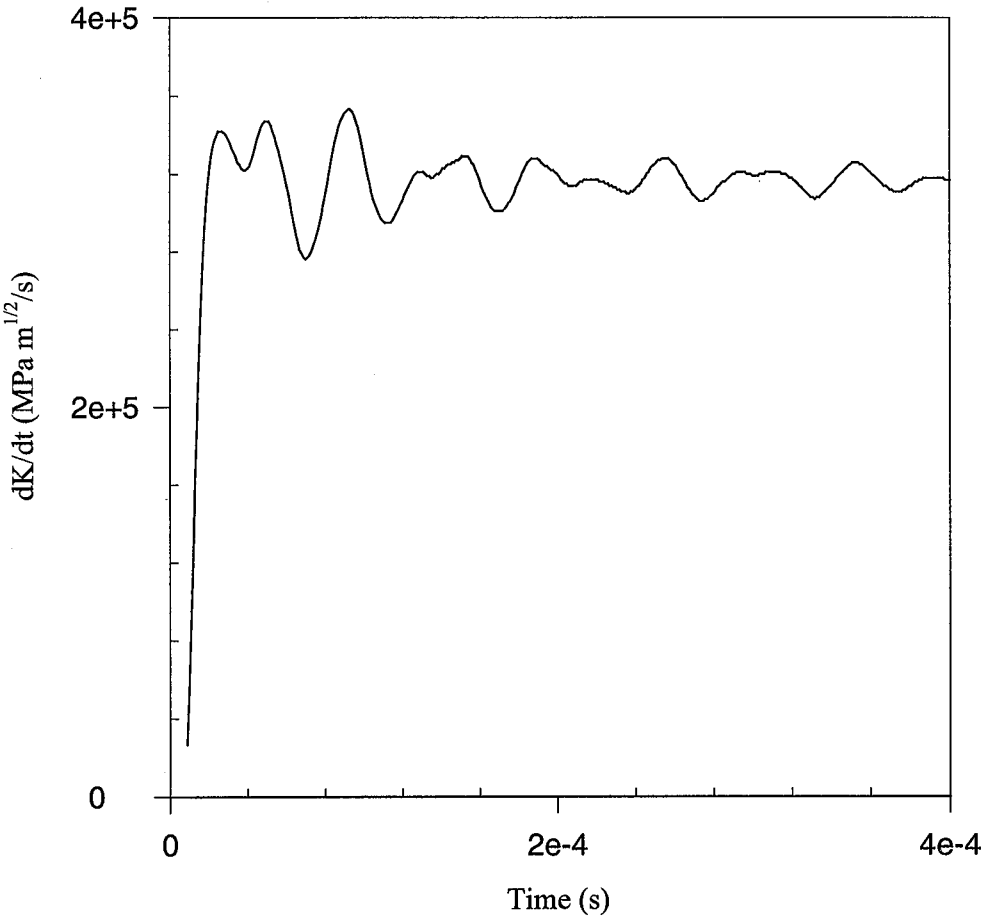

Figure 11

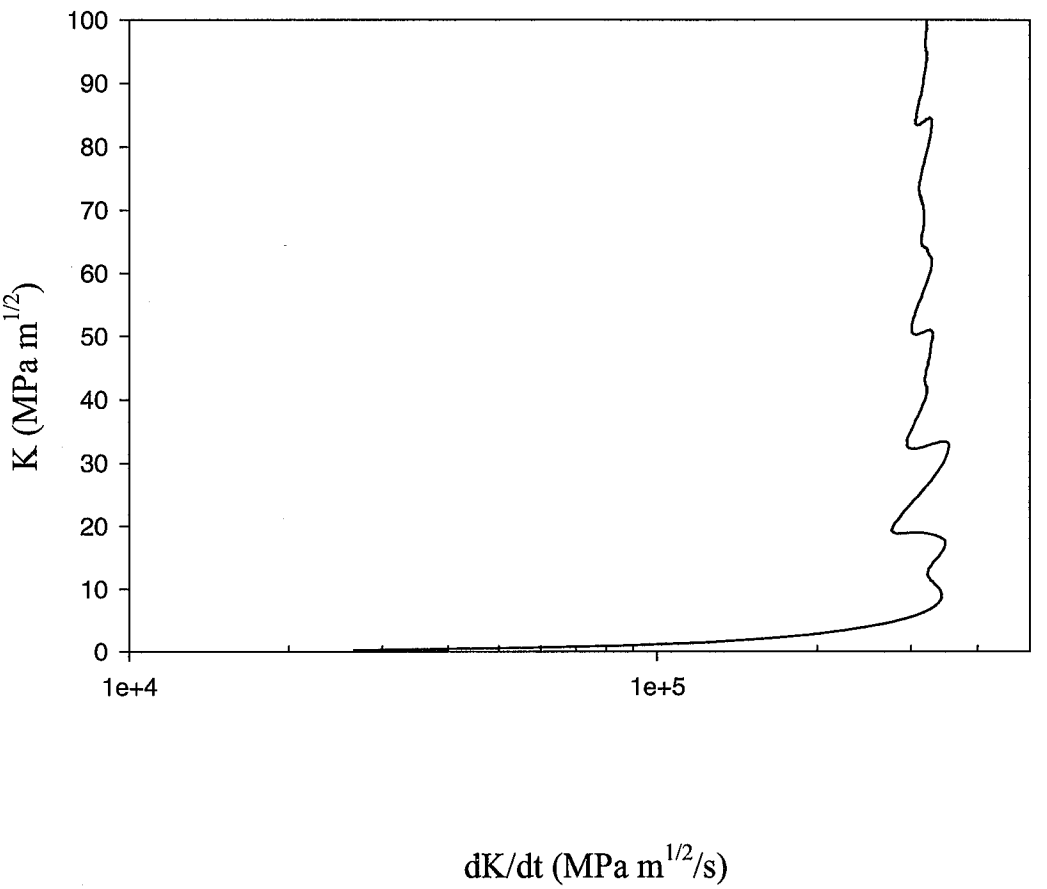

Figure 12

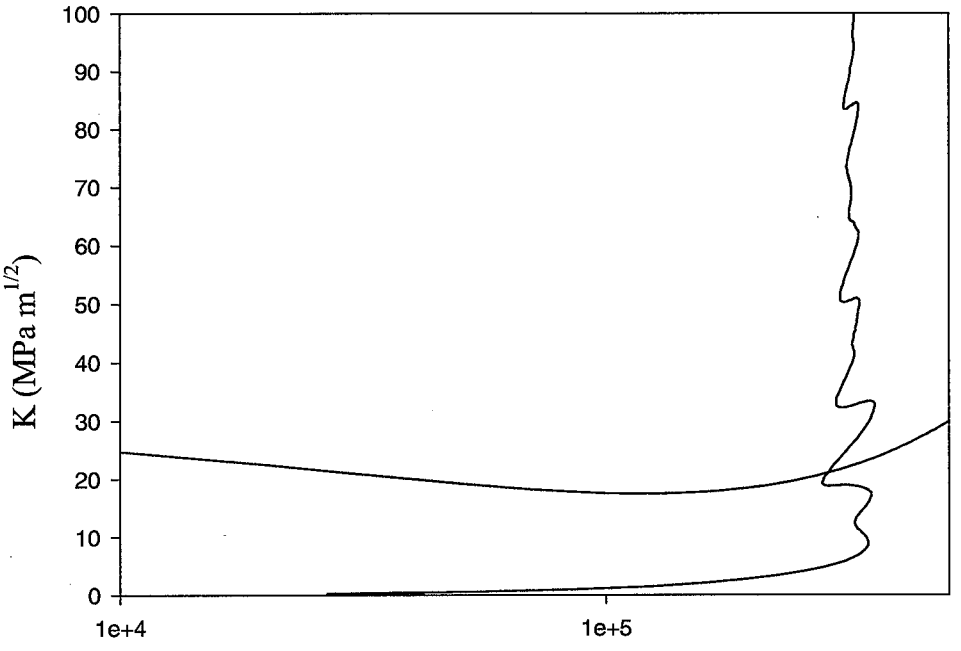

Figure 13

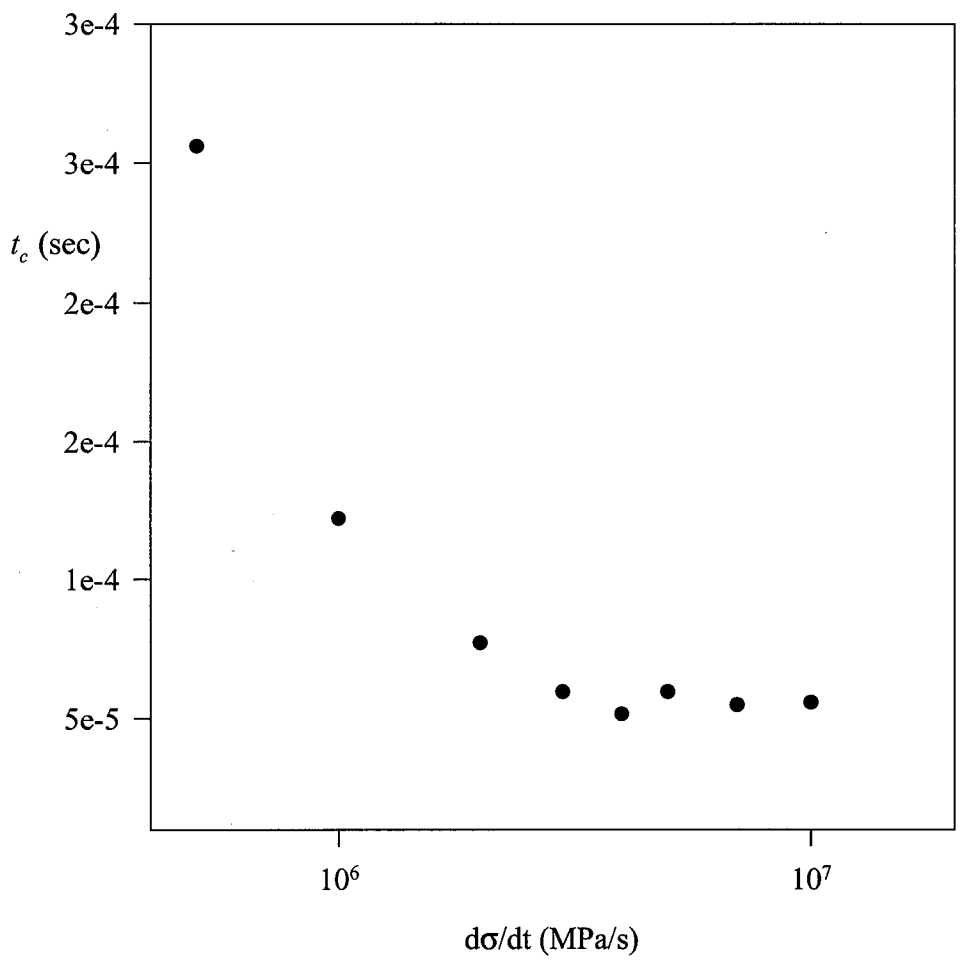

Figure 14

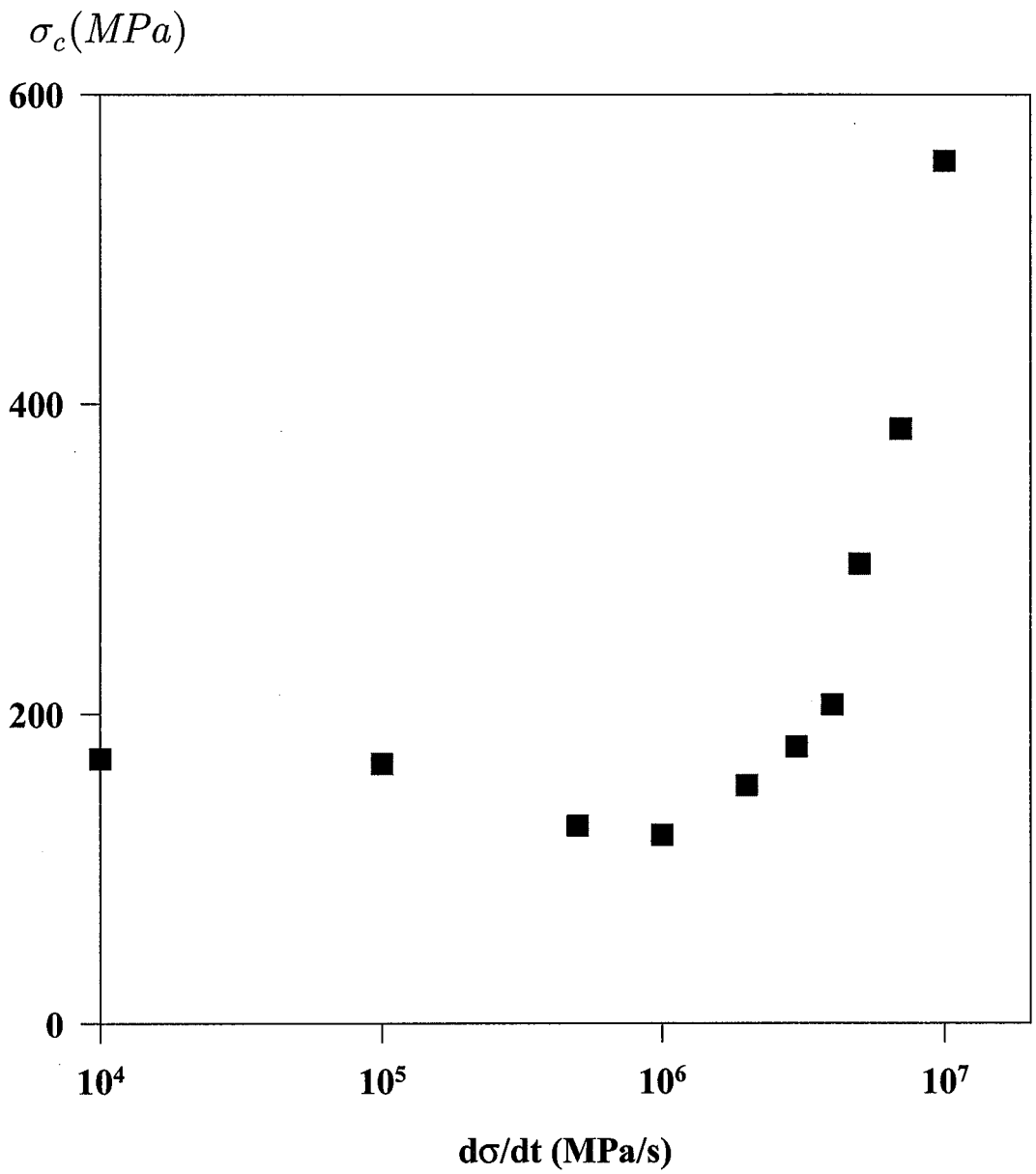

Figure 15

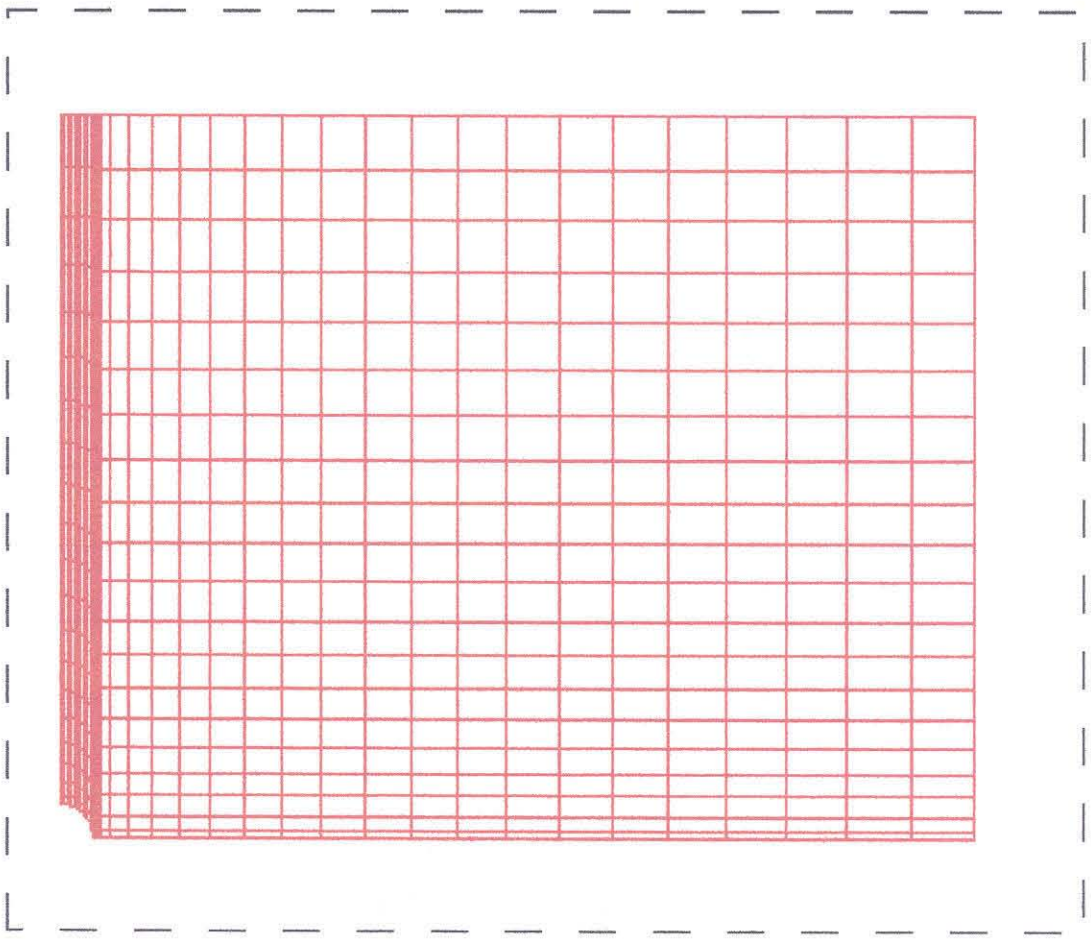

Figure 16

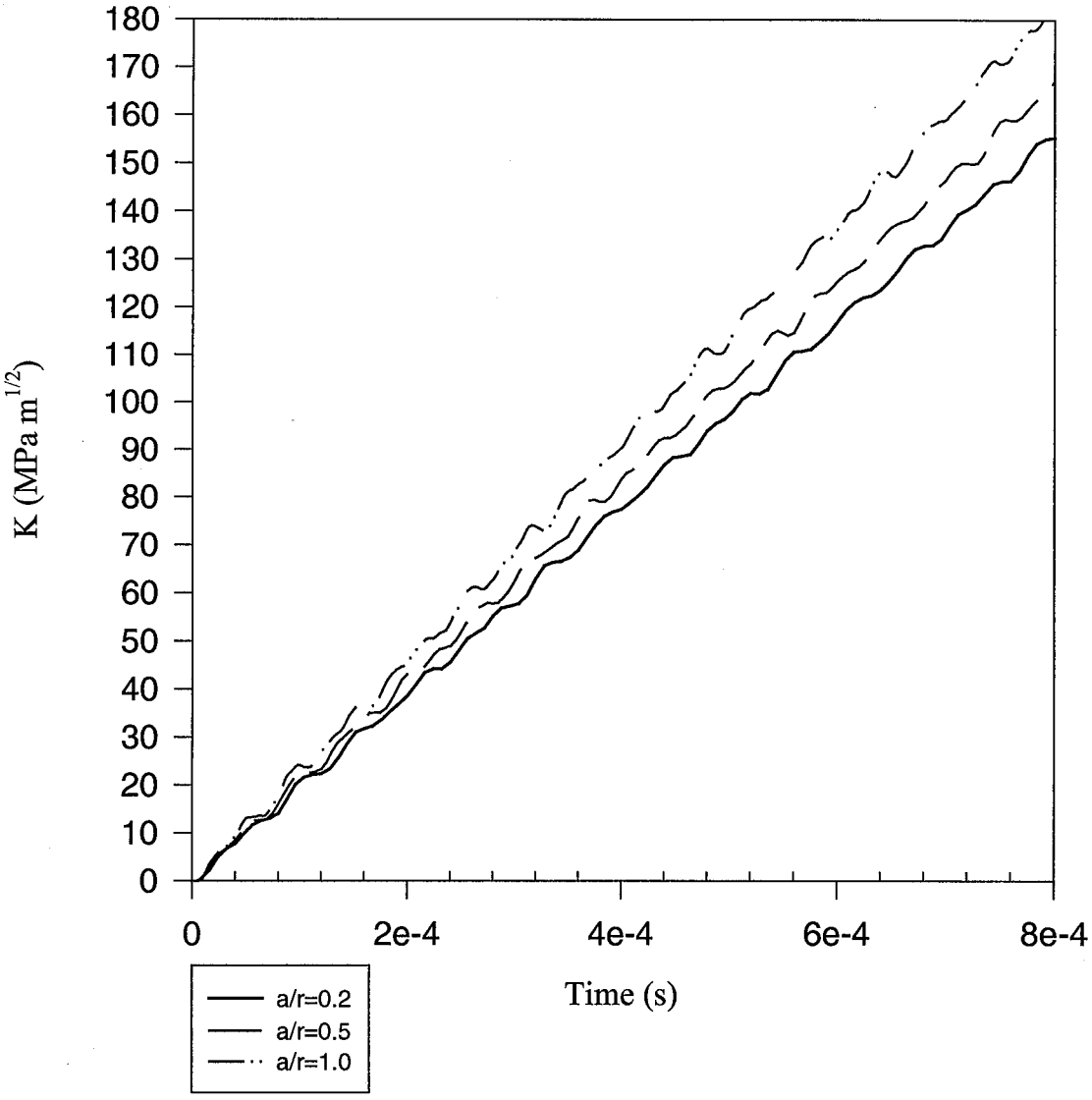
180
170
160
150
140
130
120
110
100
90
80
70
60
50
40
30
20
10
0
K (MPa m^1/2)
0
2e-4
4e-4
6e-4
8e-4
Time (s)
a/r=0.2
a/r=0.5
a/r=1.0

Figure 17

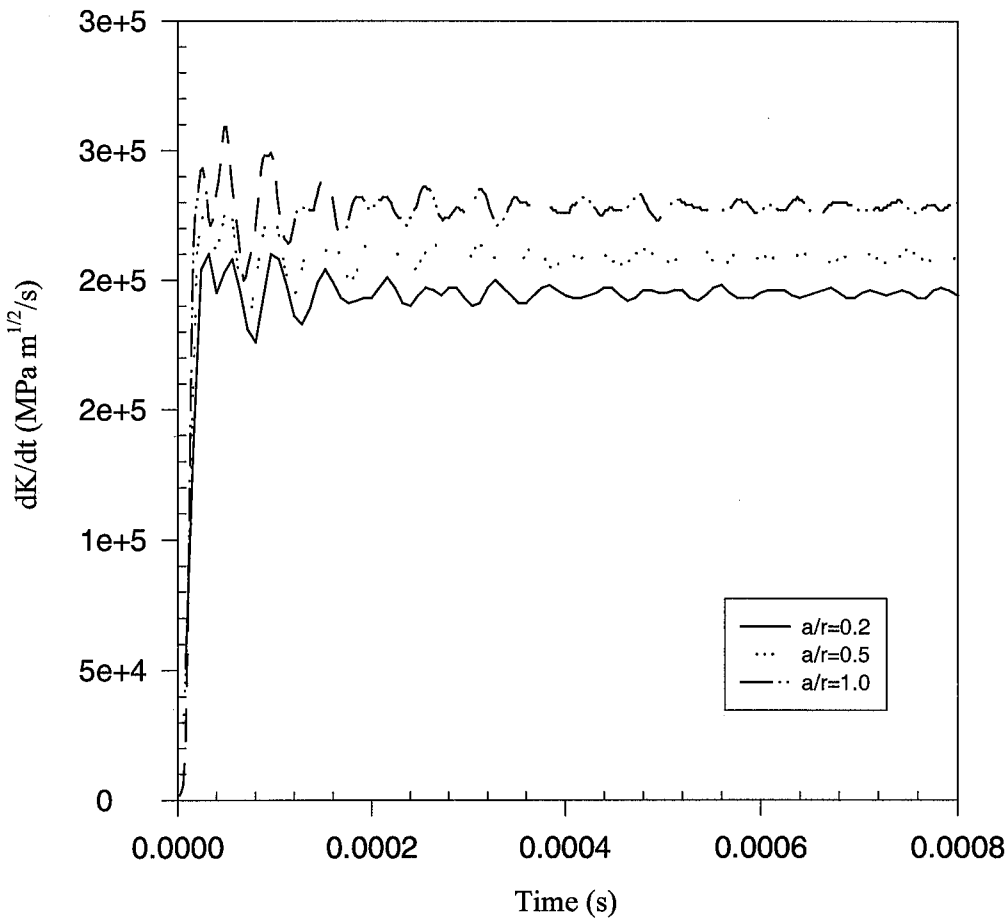
3e+5
3e+5
2e+5
2e+5
1e+5
5e+4
0
dK/dt (MPa m^1/2/s)
0.0000
0.0002
0.0004
0.0006
0.0008
Time (s)
a/r=0.2
a/r=0.5
a/r=1.0

Figure 18

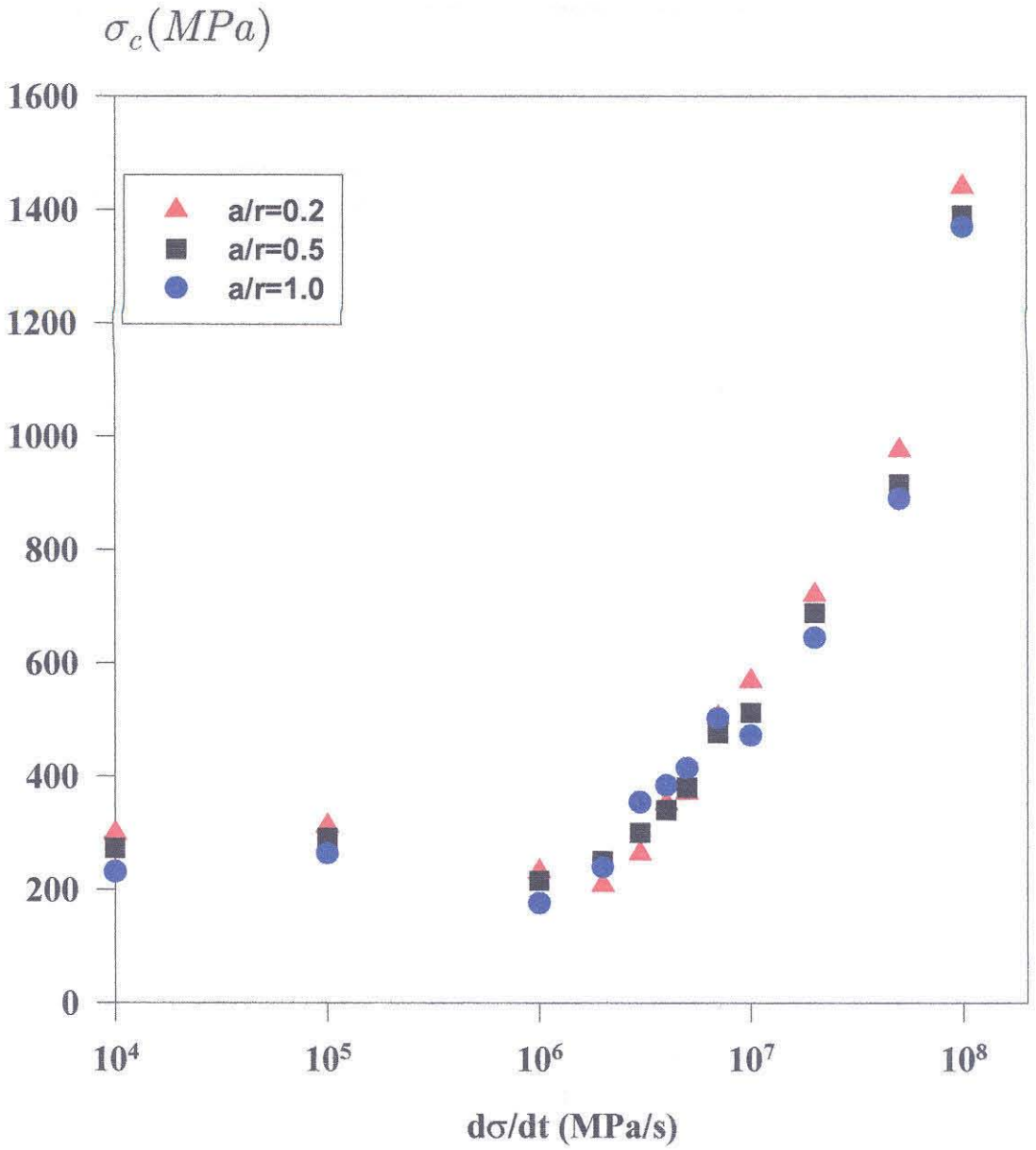
$\sigma_c(MPa)$
1600
1400
1200
1000
800
600
400
200
0
a/r=0.2
a/r=0.5
a/r=1.0
10^4
10^5
10^6
10^7
10^8
dσ/dt (MPa/s)

Figure 19

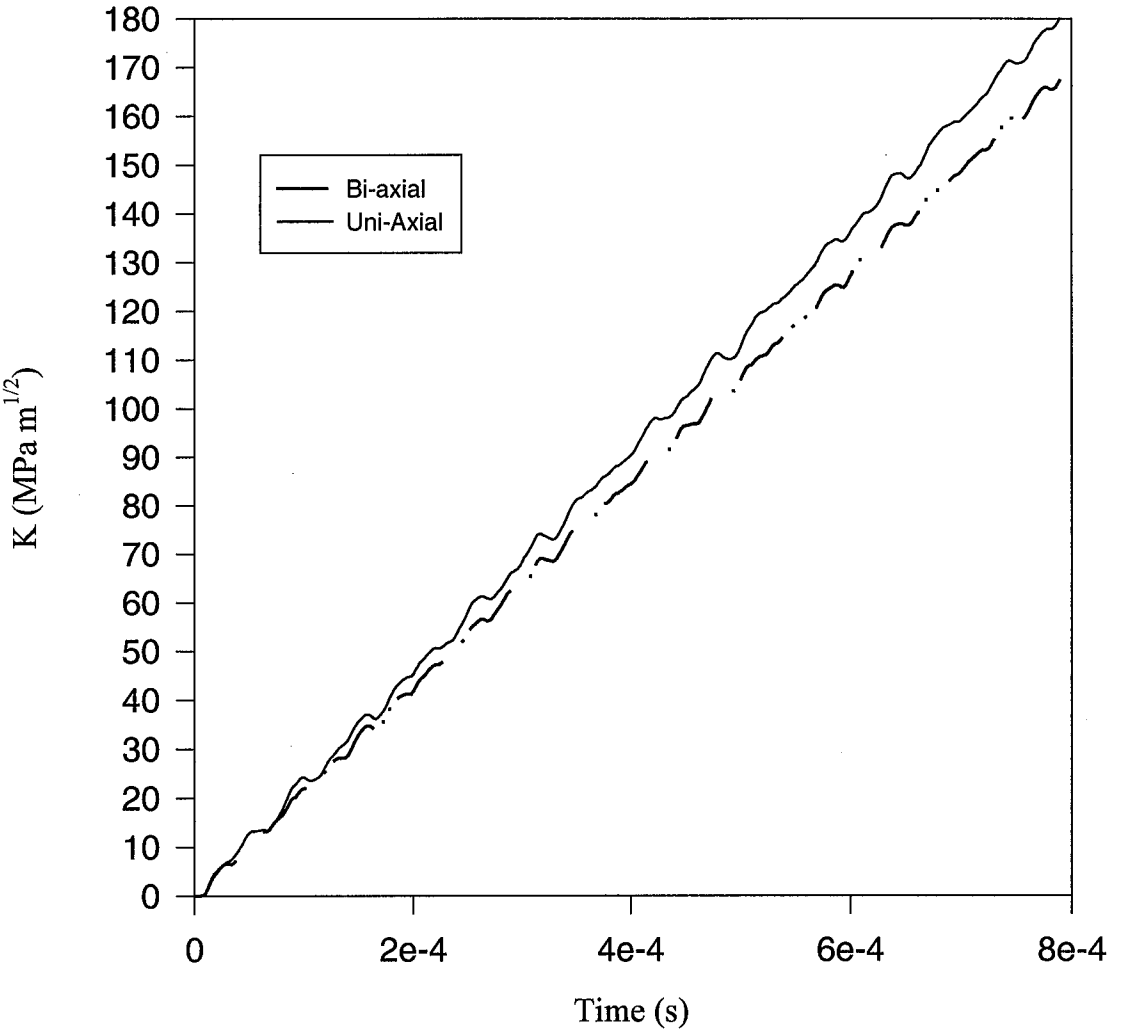
180
170
160
150
140
130
120
110
100
90
80
70
60
50
40
30
20
10
0
K (MPa m^1/2)
Bi-axial
Uni-Axial
0
2e-4
4e-4
6e-4
8e-4
Time (s)

Figure 20

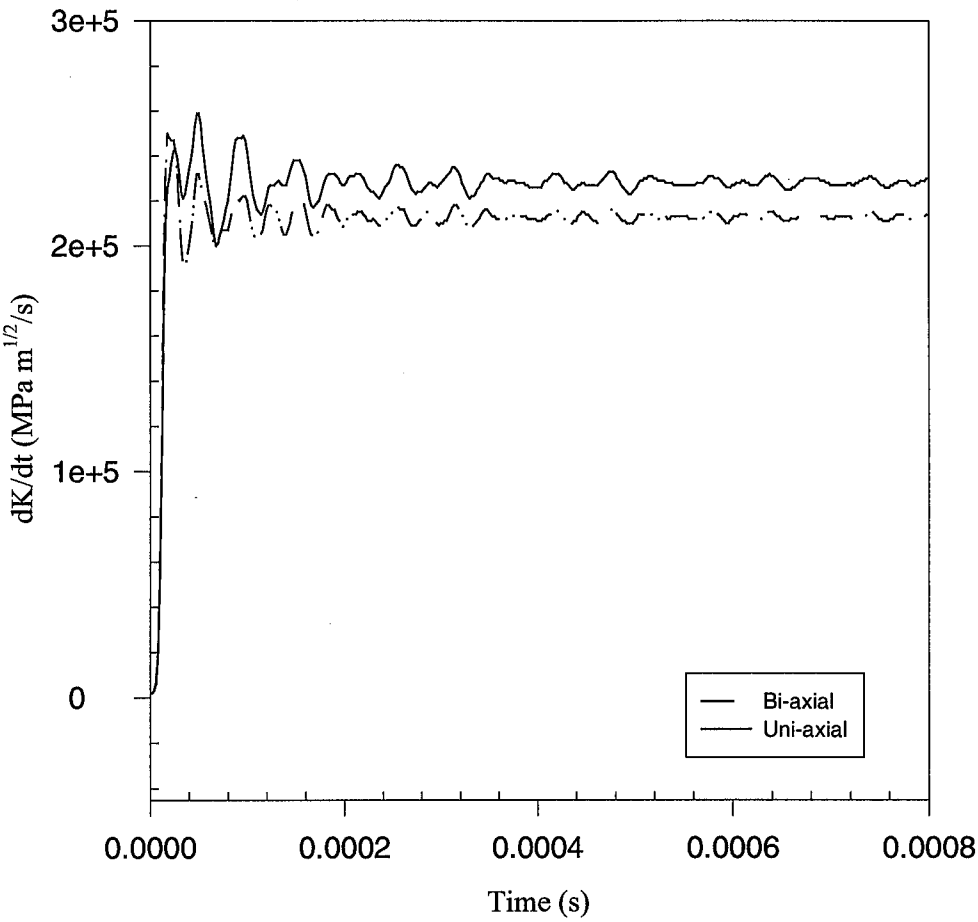
3e+5
2e+5
1e+5
0
dK/dt (MPa m^1/2/s)
0.0000
0.0002
0.0004
0.0006
0.0008
Time (s)
Bi-axial
Uni-axial

Figure 21

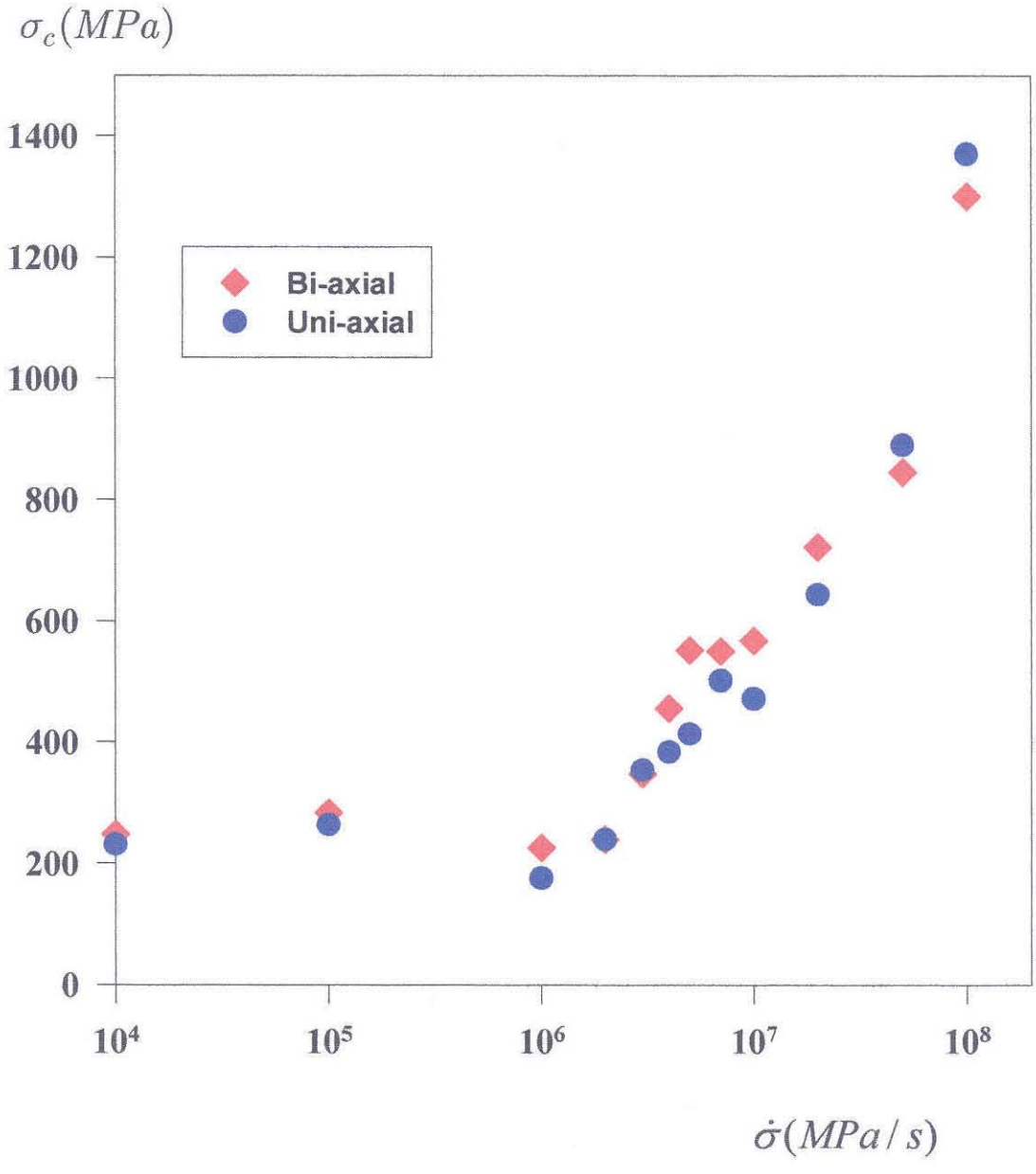
$\sigma_c(MPa)$
1400
1200
1000
800
600
400
200
0
Bi-axial
Uni-axial
10^4
10^5
10^6
10^7
10^8
$\dot{\sigma}(MPa/s)$

Figure 22

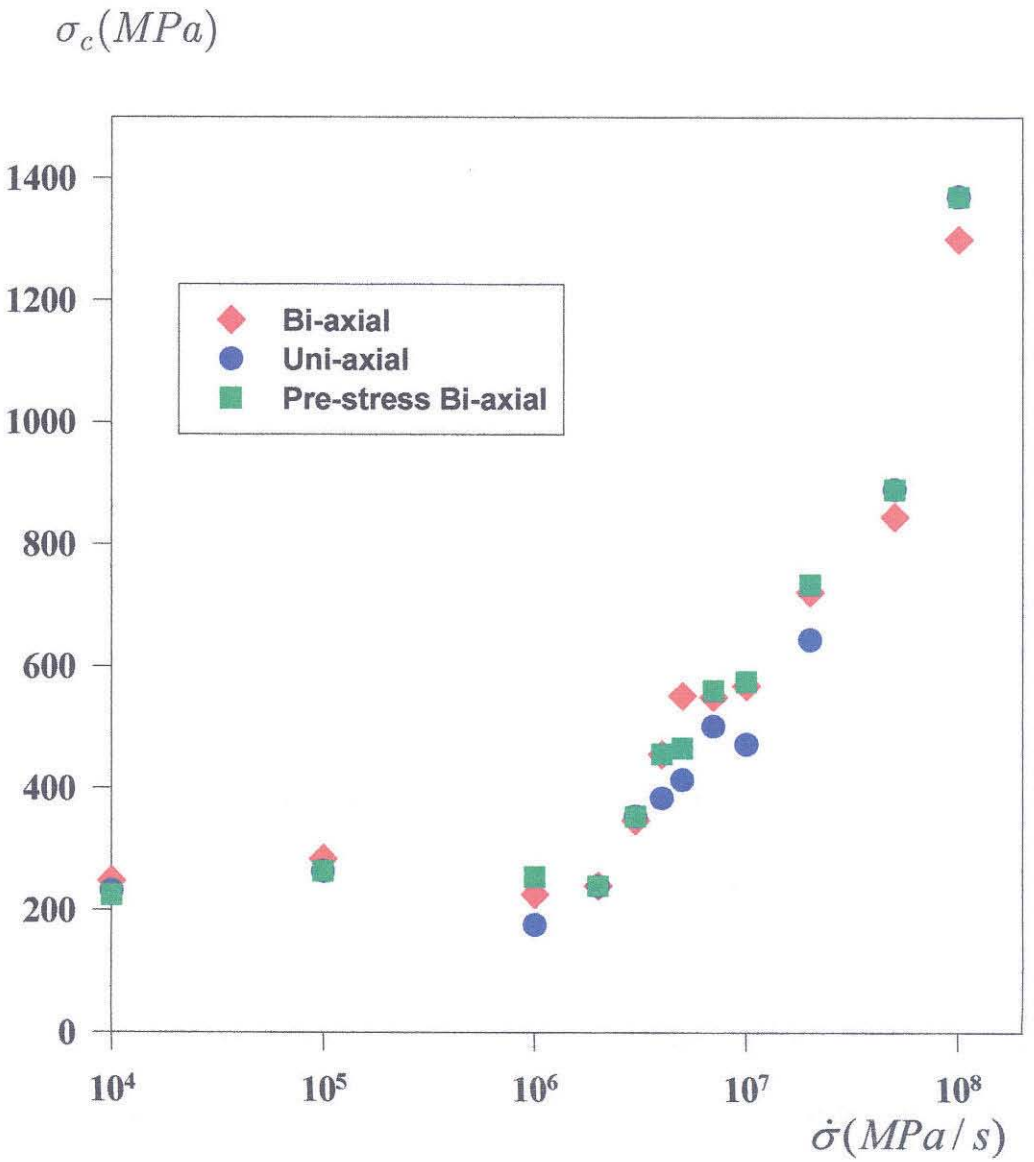
$\sigma_c(MPa)$
1400
1200
1000
800
600
400
200
0
Bi-axial
Uni-axial
Pre-stress Bi-axial
10^4
10^5
10^6
10^7
10^8
$\dot{\sigma}(MPa/s)$

Figure 23

Chapter 3

An Investigation of Mixed Mode Dynamic Crack Initiation in 2024-T3 Aluminum Alloy

Abstract

The mixed mode dynamic crack initiation in aluminum 2024-T3 alloy is investigated by combining experiments with numerical simulations. Pre-fatigued single edge notched specimens and three point bend specimens are subjected to dynamic symmetric and asymmetric loading to generate a range of mode mixity at the crack tip. The optical technique of coherent gradient sensing (CGS) and method of strain gages are employed to study the evolution of the mixed mode stress intensity factors. The dynamic mixed mode failure envelope is obtained using the crack initiation data from the experiments at a nominal loading rate of $7\times10^5\ MPa\sqrt{m}/s$ and is compared with the static counterpart for 2024-T3 aluminum alloy. The fracture surfaces near the crack initiation site are investigated using a scanning electron microscope and reveals ductile void growth and coalescence. Numerical simulations of the experiments are conducted to both help in designing the experiments and validating the results of the experiments. The numerical simulations show good correlation with the experimental results.

3.1 Introduction

Mode I fracture toughness is traditionally used in the design of metallic structures against failure. Such practice implicitly assumes that the dominant loading is tension. However, in most cases the loading is much more complex and therefore could not be treated with simple mode I loading conditions. In these situations, fracture occurs in a mixed mode fashion, and can occur under a variety of mixed mode combinations (I/II, I/III, II/III, I/II/III). In the case of aircraft fuselage structure, which is primary thin sheet structure, mixed mode fracture initiation can occur mainly in mode I/II, however, the crack can propagate under a mode III dominant condition. For a pressurized fuselage, a rivet hole with a kinked wing crack on both sides under a static pressure load is in a mixed mode loading condition, as illustrated in Figure 1 (Kennenin, 1995). In case of fuselage structure subjected to explosive/denotation loading, it represents a dynamic mixed mode loading condition for the flaws associated with wide-spread multi-site damage. Therefore, a mixed mode dynamic failure criterion based on experimental investigations is important and necessary for potential structural design in the case of explosively loaded aircraft structures, as well as other similar structural applications. A commercial aircraft fuselage is primarily constructed using aluminum 2024-T3 alloy and hence this was chosen as the material for investigation.

3.1.1 FAILURE CRITERIA

There are several fracture criteria that exist for static mixed mode I/II loading conditions. The first study of the problem was carried out by Erdogan and Sih (1963), which was based on a maximum tangential (hoop) stress approach. Another widely citied

mixed mode criteria was based on a strain energy density criterion by Sih (1974). Fracture criteria based on maximum energy release rate are widely used (e.g., Palaniswamy and Knauss, 1994, Hutchinson and Suo, 1999). Richard (1986) has proposed a generalized failure criteria that is based on a material-dependent mixed mode fracture boundary curve, as shown in Figure 2. The fracture boundary curve can be determined for different materials experimentally. It is constructed by experimentally determining combinations of fracture toughness pairs, K_I and K_{II}, at crack initiation for a variety of mode mixity, $\phi = \tan^{-1}(K_{II}/K_I)$. For the case of dynamic mixed mode fracture, this fracture criterion (or fracture envelope) is also dependent on the loading rate, $\dot{K}$, in additional to its material dependency.

Although many static failure envelopes exist for different materials, few results are available for dynamic mixed mode fracture. Dynamic mixed mode fracture was studied mainly for investigations of dynamic shear banding: Kalthoff and Winkler (1988), Grady (1992, 1994) and Guduru *et al.* (2001). Dynamic mixed mode experimental investigations have been conducted on materials such as steels, PMMA and polycarbonate by Mason *et al.* (1992), Zhou (1994), Ravi-Chandar (1995) and Rittel and Levin (1998). Data on dynamic mixed mode initiation of ductile metals is generally not available. Therefore, in order to construct the failure envelope of aluminum 2024-T3, dynamic mixed-mode initiation experiments need to be carried out. The experimental techniques and the diagnostic tools employed in the study are described in Section 3.2. In the current study, the dynamic mixed mode failure envelope of aluminum 2024-T3 at a fixed loading rate is presented in Section 3.2.

To understand the transition from opening to shearing type of fracture, it is necessary to investigate the micro-mechanism of failure. A SEM (scanning electron microscope) has been employed to study the ductile void growth on the crack surface near the initiation site and the results of this study are described in Section 3.2.4.3. Extensive numerical simulations were carried out to aid in the design of the mixed mode dynamic fracture experiments and as a tool for interpreting the experimental results.

3.2 Experimental Investigation

Mixed-mode dynamic crack initiation experiments were conducted for the 2024-T3 aluminum alloy. Various methods of loading, in one point and three point impact configurations, and diagnostic techniques were used to conduct these experiments. These experimental methods include impacting the specimen with a steel projectile from a gas gun, and utilizing CGS (Coherent Gradient Sensing) (Rosakis, 1990) and dynamic strain gage measurement (Dally, 1993) as the diagnostic techniques. The desired mode mixity was obtained by imposing impact loading in the asymmetric and symmetric configurations on specimens supported in a modified three point support or by impacting the specimen on the edge of the notch.

3.2.1 SPECIMEN DESIGN

The dimensions of the specimens used in the experiments are illustrated in Figure 3, typically 305 mm in width, 123 mm in height and 10 mm in thickness. All specimens were made from commercial grade 2024-T3 aluminum alloy plate stock. Edge notches (260 μm wide and 38.25 mm long) in the specimen were made by a wire EDM (Electro Discharge Machining). Then the specimens were pre-fatigued to introduce a sharp crack of about 2 mm in length at the tip of the notch By pre-fatiguing, the crack tip was located away from the heat affected zone introduced by the EDM wire. The pre-fatiguing is carried out following the procedures outlined in ASTM standards for fracture testing of materials (ASTM Handbook).

Since the optical interferometric technique of CGS is used to conduct the majority of the experiments, it is necessary to have the specimen resemble that of a reflective, optically flat surface. This was achieved by successive lapping and polishing. Lapping is done by using an industry standard lapping machine to make the specimens as close to optically flat as possible, and remove the surface perturbations in the plastic zones resulting from the fatiguing process. The specimens are polished by hand using different particles size of diamond paste to achieve the desired reflectivity. The strain gages for measuring the strains near the crack tip are then fixed by strain gage adhesive to the back side (non-reflective side) of the specimens.

3.2.2 DYNAMIC EXPERIMENT

The dynamic loading device used to conduct the mixed mode dynamic crack initiation is a custom-made gas gun. The gas gun is used to propel a projectile into a specimen under either a three point bend or a single edge notched loading condition. The impact velocities were kept around 40 m/s to insure a consistent loading rate for all the experiments. The projectile is made of high strength steel, cylindrical in shape (55mm in diameter and 125mm long) and weighs approximately 2.5kg.

In the experiments, two different types of loading schemes were used to achieve different mode-mixities at crack initiation. The first type involved a modified three point bend specimen, as illustrated in Figure 4. The projectile impacts on the edge of the specimen opposite from the one with the crack. The distance between the crack line and the impact point, denoted by l, is changed to obtain different mode-mixities. When l is set to zero, the loading condition corresponds to pure mode I, opening mode. The second type of loading is a modified single edge notched impact loading as illustrated in Figure 5. The projectile impacts the specimen below the crack line at a distance b from the crack line, on the side of the specimen with the pre-existing crack. The distance b is varied to achieve different mode-mixities. As b decreases, the loading approaches mode II, shear dominated condition.

3.2.3 DIAGNOSTICS

In the current investigation, two experimental diagnostic techniques were used to establish the critical conditions (time and amplitude) for dynamic mixed mode crack

initiation. On one side of the specimen, the optical technique of CGS (Coherent Gradient Sensor) is used to obtain the mixed mode dynamic stress intensity factors $K_I^d(t)$ and $K_{II}^d(t)$ (Rosakis, 1993). On the other side of the specimen, a set of strain gages was mounted to determine these mixed mode dynamic stress intensity factors (Dally and Berger, 1993). Both experimental techniques are discussed in the following sections.

3.2.3.1 CGS (Coherent Gradient Sensing)

The technique of CGS is a shearing interferometric technique that is sensitive, in reflection mode, to the in-plane (x_1 or x_2) gradients of the out-of-plane displacement (u_3). The method of CGS was first developed at Caltech by Rosakis and co-workers. The technique, its principle and background information is described in the original papers by Tippur *et al.* (1990, 1991) and also in a review article by Rosakis (1993). The experimental setup for using CGS is illustrated in Figure 6. For opaque materials, as in the present investigation on 2024-T3 aluminum alloy, the reflection mode of CGS is used. A collimated laser beam from an Innova Sabre argon-ion pulsed laser is reflected from the surface of the specimen subjected to impact and optically sheared by two high density gratings separated by distance Δ. The gratings produce multiple diffraction spots of orders 0, ±1, ±2, ... and the interference fringe pattern from the +1 or the –1 order spot is used. The images from the gratings are then focused by a convex lens and captured by a Cordin model 330A rotating mirror type high-speed film camera, which is capable of capturing 80 frames (pictures) at up to 2 million frames per second.

During the experiments, the beam can be sheared in a direction parallel to the crack (x_1) or perpendicular to the crack (x_2). The governing equation for interpreting the interference fringes is given by (Rosakis, 1993):

$$u_{3,1} = \frac{\partial u_3}{\partial x_1} = \frac{np}{2\Delta} \qquad (1)$$

where u_3 is the out of plane displacement of the specimen surface, x_1 is the direction of shearing of the beam parallel to the crack, n is the fringe order and p is the pitch of the gratings, which is 25.4 μm in the current study. Figure 7 shows a picture of a typical fringe pattern from a dynamic mixed mode experiment for the 2024-T3 aluminum alloy. Each fringe in the picture represents the locus of constant $u_{3,1}$ on the specimen surface. Since the fringes are sensitive only to the gradients of displacements, they are insensitive to rigid motions of the specimen during deformation, which makes CGS an excellent full-field optical techniques for dynamic fracture mechanics experiments.

The entire experimental system shown in Figure 6 is triggered when the projectile propelled by the gas gun impacts a strain gage attached at the location of impact on the specimen. Upon impact, the pulsed laser emits 80 discrete coherent light pulses, (514.5 nm wavelength, 20 ns pulse width) with an inter-pulse time of 2 μs. These pulses, collimated to a diameter of 50 mm, carry information about the out of plane displacement when reflected from the specimen surface, pass through the CGS setup, and the resulting interference fringe patterns are then recorded using the high speed camera. The images are recorded on TMAX 3200 high sensitivity black and white film. The field of view of

the images is approximately a circle of 27 mm diameter. Synchronization between the laser, high speed camera and the strain gage for both triggering and recording purposes is crucial to insure the successful recording of the images and gage signals. A high-speed digital oscilloscope (Nicolet Model 440) with a sampling interval of 200 nano-seconds is used to record all the strain gage signals as well as the impactor speed measured using interrupted optical beams. The film from the high speed camera is developed and the negatives are scanned into a personal computer (PC) using a high resolution Epson Scanner, (Expression 636).

For calculating the dynamic stress intensity factors, $K_I^d(t)$ and $K_{II}^d(t)$, the following equation is used, assuming plane stress conditions (Rosakis, 1993):

$$\frac{np}{2\Delta} = \frac{\nu h}{2E\sqrt{2\pi}}\left[K_I r^{-\frac{3}{2}} \sin\frac{3\theta}{2} + K_{II} r^{-\frac{3}{2}} \cos\frac{3\theta}{2}\right] \qquad (2)$$

where ν is the Poisson's ratio, h is the specimen thickness and E is the Young's modulus of the material. Using the digitized fringes and above equation, along with the least square procedure described by Mason *et al.* (1992), K_I and K_{II} can be extracted. The fringes are digitized using MATLAB and the crack tip location with respect to the original crack tip, $\Delta a(t)$, and values of $K_I^d(t)$ and $K_I^d(t)$ are calculated for each image (time) and recorded.

3.2.3.2 Method of Strain Gages

During the dynamic crack initiation experiments, measurements from two strain gages are also used for determination of mixed-mode dynamic crack initiation toughness. Dally and Berger (1993) described the method used in these experiments in detail in a review article. Figure 8 shows the coordinate system that Dally and Berger (1993) used to obtain the mixed mode stress intensity factors from the strain gage measurements. Placement of the gages is illustrated in Figure 8. The coordinate system is taken to coincide with the origin at the crack tip, and, hence $-x_1$ coincides with the crack. The orientation of the gages with respect to the crack line is determined by the Poisson's ratio (ν) of the material that is being investigated. For aluminum 2024-T3, with a Poisson's ratio, ν, of 0.33, both α and θ are 60° (Figure 8). Two strain gages placed at +60° and -60° are used to measure strains $\varepsilon_{x'x'+}$ and $\varepsilon_{x'x'-}$ along these directions. The mode I and II stress intensity factors K_I and K_{II} are computed as a function of $\varepsilon_{x'x'+}$ and $\varepsilon_{x'x'-}$:

$$K_I = E(\varepsilon_{x'x'+} + \varepsilon_{x'x'-})_g \sqrt{\frac{2}{3}\pi r_g}\,, \tag{3}$$

$$K_{II} = E(\varepsilon_{x'x'+} - \varepsilon_{x'x'-})_g \sqrt{2\pi r_g}\,, \tag{4}$$

where r_g is the distance between the strain gage and the crack tip. For a dynamically loaded stationary crack, $K_I(t_i)$ and $K_{II}(t_i)$ can be determined by measuring $\varepsilon_{x'x'+}$, $\varepsilon_{x'x'-}$ and applying Eqs. (3) and (4). The initiation time, t_i, can be obtained by examining a

major deviation from linearity in $\varepsilon_{x'x'+}$ and $\varepsilon_{x'x'-}$ as a function of time (Dally and Berger 1993, Guduru *et al.* 1998).

The Strain gages used in the experiments are 350 Ω gages obtained from Micro-Measurements, (model EA-06-062AQ-350). Each gage is placed 6 mm (r_g) from the tip of the fatigue crack, at an angle 60° to the crack. The strain gage signals are recorded using the Nicolet Model 440 oscilloscope at a sampling interval of 200 ns.

3.2.4 EXPERIMENTAL RESULTS

In most experiments that were conducted, both CGS and strain gage techniques were employed. Good agreement was found between the two methods in the determination of critical stress intensity factors and the time to crack initiation. Hence, because of its simplicity, some experiments were conducted using only the strain gage method. In this section, the results from both the strain gage and CGS experiments are presented first. From the experimental results, a failure envelope, K_{IC}^{d} vs. K_{IIC}^{d} for the dynamic crack initiation is constructed. The SEM micrographs of the crack surfaces for various experiments are presented to illustrate the different micro-mechanisms of failure.

3.2.4.1 CGS and Strain Gage Experimental Results

Figure 9 shows a series of CGS images from a dynamic mixed-mode experiment using the gas gun with an impact velocity of 40 m/s. In order to identify mixed mode dynamic crack initiation toughness, one needs to identify the time at which crack initiation takes place. In dynamic ductile fracture, this is recognized to be a difficult problem (e.g., Costin and Duffy, 1979, Guduru *et al.,* 1998). One way to identify crack initiation is to plot the crack extension, $\Delta a(t)$, deduced from locating the current crack tip using the curve fitting procedures employed in analyzing the CGS fringe pattern. As $\Delta a(t)$ increases outside of the noise zone, one can identify the initiation time by extrapolating the linear portion of the $\Delta a(t)$ and intersecting it with abscissa (t-axis) to locate the initiation point. As shown in Figure 10(a), the initiation time, t_i, is around 50 μs. Figure 10(b) shows a typical $K_I^d(t)$ and $K_{II}^d(t)$ vs. t for a dynamic mixed mode CGS experiment, each data point obtained by fitting the fringe pattern using the procedure (Mason *et al.,* 1992) described in Section 3.3.1. In this case the computed $K_I^d(t_i)$ and $K_{II}^d(t_i)$ from the digitized CGS fringes at $t=t_i$ are $23.78\ MPa\sqrt{m}$ and $13.06\ MPa\sqrt{m}$, respectively.

Strain gage results are analyzed from the raw signals recorded using the high-speed digital oscilloscope. Figure 11 shows the raw strain gage signals from a typical dynamic mixed-mode experiment using the gas gun with an impact velocity of 40 m/s. Since the oscilloscope begins to acquire data before the specimen is impacted (usually it is triggered by the projectile velocity measurement system), it is necessary to identify the time of impact. Therefore, the signal from the strain gage that is fixed at the point of impact on the specimen is also needed to pin point the initiation time, t_i. The jump in the

signal from the strain gage at the point of impact is identified as t_o. Since all the strain gage signals are recorded on the same oscilloscope, t_o needs to be subtracted from the actual time of initiation in order to accurately determine initiation time, t_i. This t_i can later be compared with the one from the CGS data for the same experiment when both CGS and strain gages are used. Figure 11 shows typical strain gage data for the same experiment as discussed in the CGS section (gas gun mixed-mode experiment with a impact velocity of 40 m/s). An apparent deviation from linearity is observed at $t = 49\ \mu s$. This corresponds to the crack initiation time t_i, (note that this t_i has already taken into account of the time takes for the impactor to impact the strain gage on the specimen). Figure 12 shows the $K_I^d(t)$ and $K_{II}^d(t)$ calculated from the strain gage signal using Eqs. (3) and (4) for the same experiment. The dynamic mixed mode crack initiation toughness pair are identified by $K_I^d(t_i)$ and $K_{II}^d(t_i)$. In this case the computed $K_I^d(t_i)$ and $K_{II}^d(t_i)$ from the strain gage signals at $t=t_i$ are $23.86\ MPa\sqrt{m}$ and $13.54\ MPa\sqrt{m}$, respectively. The effective dynamic stress intensity factor, K_{eff}^d, is defined as the follows:

$$K_{eff}^d(t) = \sqrt{(K_I^d(t))^2 + (K_{II}^d(t))^2} \qquad (5)$$

The loading rate $\dot{K}_{eff}^d$ is calculated from the slope of the nearly linear portion of $K_{eff}^d(t)$ until crack initiation, i.e., $\dot{K}_{eff}^d = K_{eff}^d(t_i)/t_i$. In this case, the crack tip loading rate $\dot{K}_{eff}^d$ is $5.6\times10^5\ MPa\sqrt{m}/s$.

Most of the experiments were conducted with both CGS and strain gage setup simultaneously. By doing so, we were not only able to compare the results from the two different methods but also to help pin-point the time of crack initiation in cases where initiation is not obvious in either measurement. An example of the comparison between the two techniques is shown using the CGS data in Figure 10 and strain gage data in Figure 12. As seen in the strain gage data in Figure 11, initiation occurs at $t = 49\ \mu s$, as shown by the deviation from linearity. In Figures 9 and 10, one can see from the CGS data shows that initiation occurs at $t = 50\ \mu s$, by the extrapolating the linear portion of $\Delta a(t)$ back to zero, for the same experiment. This initiation time as obtained from these distinctly different techniques, agree reasonably well within experimental error. Comparing the $K_I^d(t_i)$ and $K_{II}^d(t_i)$ obtained from the two techniques, they are very similar in value, with the difference in their values less than 5%.

The mixed mode dynamic initiation toughness pair $K_I^d(t_i)$ and $K_{II}^d(t_i)$ were determined for all the experiments using the techniques described in the previous section. The loading rate $\dot{K}_{eff}^d$ for all cases was found to be around $7\times10^5\ MPa\sqrt{m}/s$. By keeping loading rates for all the experiments as close as possible, the effect of loading rate on the failure envelope is eliminated. A mode I experiment using three point bend specimen and gas gun was also conducted for the impact velocity of 40 m/s to give a dynamic mode I initiation toughness, K_{IC}^d, to be used as a normalizing factor in the construction of the dynamic failure envelope.

Experiments where specimens were supported using three point bend support with projectile impact on the opposite side from the pre-cracked edge (shown in Figure 4) result in $K_{II}^{d}(t_i)$ and $K_{I}^{d}(t_i)$ closer to open or mode I dominated failures. The experiments where single edge notched specimens (shown in Figure 5), with projectile impact just below the crack, produce $K_{II}^{d}(t_i)$ and $K_{I}^{d}(t_i)$ pairs that are closer to shear or mode II dominated crack initiation.

3.2.4.2 Dynamic Mixed Mode Failure Envelope

Once the mixed mode dynamic initiation toughness pairs, $K_{I}^{d}(t_i)$ and $K_{II}^{d}(t_i)$, are determined for the different mode-mixities, one is able to construct the failure envelope by plotting $K_{II}^{d}(t_i)$ vs. $K_{I}^{d}(t_i)$ for each case. This gives the dynamic failure envelope curve, as shown in Figure 13, for the loading rate $\sim 7\times10^{5}\ MPa\sqrt{m}/s$. As shown in Figure 14, the shape of the dynamic failure envelope follows the same trend as the static data given by Chao and Liu(1995). The dynamic values of $K_{I}^{d}(t_i)$ and $K_{II}^{d}(t_i)$ pairs are generally less than the static values. This is expected since the K_{IC}^{d} value for this loading rate of $7\times10^{5}\ MPa\sqrt{m}/s$ is $26.3\ MPa\sqrt{m}$, which is less than the static value of $30\ MPa\sqrt{m}$ (Chow, Rosakis and Ravichandran, 2001).

During the current investigation, pure mode II loading under dynamic loading was not achieved. But as shown in Figure 14, the K_{IIC}^{d} value approaches to $22\ MPa\sqrt{m}$. Thus, for the purpose of curve fitting, the value used for K_{IIC}^{d} is $22\ MPa\sqrt{m}$. As shown by Richard (1987), a mixed mode fracture boundary, as shown in Figure 2, can be expressed by the following equation:

$$\left(\frac{K_I}{K_{IC}}\right)^u + \left(\frac{K_{II}}{K_{IIC}}\right)^v = 1 \qquad (6)$$

One can choose the value of u and v to fit the experimentally determined values fairly well. Utilizing Eq. (6), one will be able to fit the experimentally determined data from Figure 14 to calculate the value and u and v, and thus calculate the value of K_{IIC}^{d}. In order to do so, one first needs to normalize the $K_I^d(t_i)$ and $K_{II}^d(t_i)$ pairs for each case by the K_{IC}^{d} and K_{IIC}^{d} obtained from the experiments for this loading rate (in this case, $26.3MPa\sqrt{m}$ and $22MPa\sqrt{m}$ respectively) and then plot the $K_{II}^d(t_i)/K_{IIC}^d$ vs. $K_I^d(t_i)/K_{IC}^d$. Figure 15 shows the fitted curve utilizing Eq. (6) for the current experimental data. The curve represents the dynamic failure envelope for aluminum 2024-T3 alloy under dynamic mixed mode loading conditions for a loading rate $\sim 7\times10^5 MPa\sqrt{m}/s$. For a $K_I^d(t_i)$ and $K_{II}^d(t_i)$ pair inside this fracture boundary curve, there is no crack initiation. Once the $K_I^d(t_i)$ and $K_{II}^d(t_i)$ value reaches the boundary, the crack starts to initiate under dynamic mixed mode conditions. The values of u and v are 4 and 5, respectively, for this experimental study.

3.2.4.3 SEM Fractography

Scanning Electron Microscope (SEM) fractographs were taken on the specimen crack surfaces near the crack tip initiation region to understand the micro-mechanisms of failure under dynamic mixed mode loading conditions. Selected samples from the initiation areas of different specimens were cut using a bench saw into approximate cubes with sides of 1 cm. The surface that was examined included the pre-fatigued, as well as the crack initiation regions. The samples were then examined using a Camscan Series II Scanning Electron Microscope.

In order to illustrate the failure mechanisms at different mode mixities, samples were taken from six different specimens, including a mode I sample. The fractograph of these samples at a range of magnifications are shown in Figure 16 to 21, transitioning from pure mode I to mostly mode II dominated loading. As mode mixity transitions from mode I to mode II, the features shown in the fractographs, such as voids size and shape, change. For mode I dominated loading, the fracture occurred by a ductile micro-void nucleation, growth and coalescence process. There are primarily large voids circular in shape nucleated from particles and inclusions, as shown in Figure 16. As the loading gradually changes from mode I to mixed mode, the large voids become more elongated and are accompanied by smaller void sheets that forms a wave-like pattern in the sheared direction. In the mixed mode region, the voids are elongated and the inclusions break in shearing mode as illustrated by Figure 22. As the mixity becomes mode II dominated,

the number of large circular voids decreases dramatically with only the presence of the small void sheets that composed of elongated (sheared) voids in a pattern parallel to the shearing direction, as shown in Figure 21.

To illustrate the significant differences in the failure mechanism between tensile and shear dominated fracture, Figure 23 compares the two extreme loading conditions (mode I and mode II) by comparing the fractograph of the two samples at different magnifications. At lower magnification (200X), the shear dominated fracture shows a parallel sheared line patterns while the mode I fracture shows large circular voids. At higher magnification (600X), the mode I fracture surface consists of primary voids of $20\,\mu m$ in diameter and the shear dominated surfaces contain small voids forming void lines or void sheets. At a magnification of 1500X, the dramatic shape and size differences can be seen for voids in both cases. It can be seen that while the mode I fracture is mainly dominated by nucleation, growth and coalescence of large voids, the shear dominated fracture is caused by growth, coalescence and linkage of small secondary sheared void sheets.

3.3 Numerical Simulations of Mixed Mode Dynamic Fracture Experiments

Numerical simulations of the mixed mode dynamic initiation experiments were carried out using a commercial finite element code, LS-DYNA. The numerical simulations were conducted for two purposes: The first was used to design the mixed mode fracture experiments. By conducting the numerical simulations with the

approximate loading conditions to be used in the experiments, one can collect important information such as the loading rate $\dot{K}$, mode mixity and approximate time to failure. Since each experiment requires time consuming specimen preparation and lengthy experimental setup, by knowing the information in advance, one is able to set the approximate inter-frame time for high-speed photography, the correct projectile velocity and appropriate loading setup. Another purpose of the numerical analysis is to validate the experiment. By using established techniques to calculate mixed mode dynamic stress intensity factors as a function of time, one is able to compare the numerical result to that of the experimental results to verify the data reduction scheme used in reducing the raw experimental data.

In the following sections, the details of the current numerical studies are described. First, finite element modeling using LS-DYNA using elastic material properties is presented. Second, the issue of material nonlinearity is addressed by using a power law, elastic-plastic description for the 2024-T3 aluminum alloy. The method used to extract mixed mode stress intensity factors K_I and K_{II} is also presented. This method is validated by comparing the result with the theoretical and numerical results of Lee and Freund (1990). Third, the results of the numerical simulations are presented and comparison to the experimental results are illustrated.

3.3.1 LS-DYNA

The commercial finite element program LS-DYNA is used to conduct the numerical simulations. LS-DYNA is a general purpose finite element code for analyzing the large deformation dynamic response of structures. It is an explicit, nonlinear, dynamic Lagrangian code first developed by the Lawrence Livermore National Laboratory, which has been improved, modified and marketed by Livermore Software Technology Corporation. The program is chosen for the current numerical studies due to its capabilities in modeling complex, nonlinear, dynamic and contact problems. LS-DYNA consists of over 130 different types of custom material models, including linear elasticity, power law plasticity, temperature dependent, rate sensitive, special purpose materials and user defined material properties for nonlinear dynamic analysis. The element formulations include 1-D elements, 2-D plane stress, plane strain, axi-symmetric and shell elements as well as 3-D brick elements. The program also has the capability of modeling sophisticated contact interfaces including frictionless sliding, frictional sliding, tied interface and deform to rigid contact. These contact capabilities are useful when modeling the impact interface, the interface between the specimens and supports as well as the contact interfaces between the crack surfaces. In the following sections, only relevant topics to the current studies about LS-DYNA are briefly presented. Detailed explanation of capabilities and underlying theories of the finite element program can be found in the LS-DYNA user manual and theoretical manual published by Livermore Software Technology Corporation (1999).

3.3.2 ELASTIC ANALYSIS

For the current studies, the linear elastic material model is used initially to model the specimens under dynamic impact. The linear elastic material properties used for the aluminum 2024-T3 alloy are as follows: density, $\rho = 2700\ kg/m^3$, the Young's modulus, $E = 72.5\ GPa$, and the Poisson's ratio, $\nu = 0.33$. The material properties of the projectile and the support in the experiments are modeled as rigid materials with density of steel, $\rho = 7800\ kg/m^3$.

Different element formulations have been investigated to model the aluminum specimens under impact loading. Both two-dimensional, 4 node plate elements and three-dimensional, 8 node brick elements were used to conduct the simulations. Both formulations produced very similar results for a specimen that was simulated. The features and choices of contact interfaces offered by LS-DYNA for three-dimensional brick elements are much more robust than the two-dimensional elements provided by LS-DYNA. As the three-dimensional brick formulation does not change computation time significantly over the two-dimensional plane stress formulation, the formulation of three-dimensional brick elements is used to conduct the simulations of the dynamic mixed mode crack initiation experiments.

The exact dimensions of the actual specimens (Figures. 4 and 5) are used in the numerical simulations. The aluminum specimens are modeled with a single layer of elastic 8 node brick elements. The crack face is modeled by disconnecting nodes on adjacent elements. The supports and the projectile are modeled with rigid solid brick elements. There are about 12000 nodes and 9500 solid elements in a typical simulation.

The specimen thickness is modeled using one layer of 3-D elements to simulate plane stress conditions. Since the experimental measurements are interpreted with plane stress assumptions, it was decided to simulate such conditions in the numerical analysis. Figure 24 shows a typical mesh for the numerical analysis.

The interfaces between the specimen and the projectile, as well as the interface between the specimen and supports, are modeled as nodes to surface contacts. The master surface used is always the rigid element. Since LS-DYNA always prevents slave surfaces penetrating the master surface, setting rigid elements as the master surface are apparent. The crack surface is also modeled with contact interfaces, which is relevant under mixed mode loading conditions.

To model the projectile impacting the specimen, an initial velocity of 40 m/s is assigned to the projectile in the direction of impact. The bottom nodes of the support are fixed to avoid rigid body translation of the whole model. LS-DYNA automatically determines time step sizes from the element size and the following material properties: Young's modulus E, Poisson's ratio ν, and density ρ. For detailed calculation of the minimum time step size, refer to the theoretical manual of LS-DYNA. A typical termination time of 10 *ms* is specified for each analysis. The field variables such as nodal displacements, element stresses and strains are recorded in a binary output data file for post-processing purposes.

3.3.3 ELASTIC-PLASTIC ANALYSIS

Elastic-plastic analyses using power law plasticity were also conducted. Such analyses were conducted to assess the effect of crack tip plasticity. The results were compared with that of the elastic analyses. When conducting elastic-plastic analyses, all the other analysis parameters and conditions were kept unchanged, except for the material properties of the specimen.

A power law model using the Ramberg-Osgood constitutive material description is employed to model the aluminum 2024-T3 specimens. A stress vs. strain curve for aluminum 2024-T3 is shown in Figure 25 (Hodowany *et al.* 2000). The following equation describes the plasticity constitutive relation in LS-DYNA:

$$\frac{\varepsilon}{\varepsilon_o} = \alpha(\frac{\sigma}{\sigma_o})^n$$
$$\sigma_o = E\varepsilon_o, \tag{7}$$

where $E = 72.5GPa$ is the Young's modulus, $\sigma_o = 350MPa$ is the yield stress, $\alpha = 0.87$, $n = 8.7$ and ε_o is the reference strain.

3.3.4 CALCULATION OF MIXED MODE STRESS INTENSITY FACTORS

The comparison between the results of the elastic-plastic and elastic material model did not produce noticeable differences. It was concluded that small scale yielding

conditions were met. Thus, one can determine the stress intensity factors from the knowledge of asymptotic displacement or stress fields.

In order to extract the stress intensity factors $K_I^d(t)$ and $K_{II}^d(t)$, the in-plane displacement, $u_1(t)$ and $u_2(t)$, near the crack tip are used. Figure 26 is a schematic of the deformations under mixed mode loading conditions. As shown in Figure 26, O is the location of the crack tip, A and A' are locations of two adjacent points (nodes) on the two crack faces with distance x_1 away from the crack tip which initially coincide with each other. After loading starts, the two nodes start to move in the fashion shown in the figure. If the relative displacements between the two nodes are denoted as $\Delta u_1(t)$ and $\Delta u_2(t)$ in the x_1 and x_2 directions respectively, then for linearly elastic solids, the dynamic mixed mode stress intensity factors can be computed using LEFM:

$$K_I^d(t) = \frac{E}{4}\sqrt{\frac{2\pi}{|x_1|}}\Delta u_2(t)(x_1, \theta = \pi)$$

$$K_{II}^d(t) = \frac{E}{4}\sqrt{\frac{2\pi}{|x_1|}}\Delta u_1(t)(x_1, \theta = \pi). \qquad (8)$$

The stress intensity factors can also be found using the normal stress distribution, $\sigma_{22}(t)$, and shear stress, $\sigma_{12}(t)$, ahead of the crack tip by the following:

$$K_I^d(t) = \sqrt{2\pi x_1}\sigma_{22}(r, \theta = 0, t)$$
$$K_{II}^d(t) = \sqrt{2\pi x_1}\sigma_{12}(r, \theta = 0, t). \tag{9}$$

Once the stress intensity factors are obtained, one will be able to obtain the information on mode mixity and loading rate. The mode mixity is computed by:

$$\phi = \tan^{-1}\left(\frac{K_{II}}{K_I}\right). \tag{10}$$

The loading rate, $\dot{K}_{eff}^d$, can be found by first calculating $K_{eff}^d(t)$ using Eq. (5) and then differentiating $K_{eff}^d(t)$ with respect to time. This information is crucial in helping to design experiments with desired mode mixity. In adopting the procedure described above, it is implicitly assumed that the K-field is established in the region of interest

3.3.5 VALIDATION STUDY USING THE LEE AND FREUND SOLUTION

In order to validate the method of extracting the mixed-mode dynamic stress intensity factors, $K_I^d(t)$ and $K_{II}^d(t)$, discussed in the previous section, numerical simulation was conducted to compare with the result of Lee & Freund (1990). Motivated by the experiments conducted by Kalthoff and Winkler (1988), Lee and Freund (1990) carried out theoretical and numerical investigations of the evolution of the mixed mode stress field in a single edge notched specimen, impacted under the notch. Reasonable

agreement was found between the predictions of the theoretical analysis and the experimental results reported by Kalthoff and Winkler (1988). Figure 27 shows the loading configuration of Kalthoff and Winkler (1988)'s experiments and the one used by Lee and Freund (1990) in their theoretical and numerical investigation. To accurately validate the method of determining stress intensity factors (Eq. (8)) with that of Lee and Freund (1990), a numerical simulation was carried out using LS-DYNA to simulate a crack of length a in a semi-infinite solid used in Lee and Freund's analysis.

The mesh used for this validation analysis is shown in Figure 28. To simulate a semi-infinite plate under impact loading, the crack length needs to be much smaller than other dimensions in the analysis. The following normalized dimensions are used in the analysis: crack length $a=1$, plate width $w=20$, height $h=10$ and plate thickness $t=0.5$. The material properties used in the simulations are: density $\rho=1.0$, Young's modulus $E=1.0$ and Poisson's ratio $v=0.25$. The Poisson's ratio of 0.25 was chosen to match the one used in Lee and Freund (1990)'s studies. Plane strain two dimensional elements in LS-DYNA are used to simulate the plane strain conditions used in Lee and Freund (1990)'s work. An initial velocity v_o simulates a step pulse having a magnitude of 0.01 applied over a region at the edge of the crack, as shown in Figure 28.

The stress intensity factor are normalized by the following scale factor K':

$$K' = \sqrt{\frac{a}{\pi}} \frac{Ev_o}{2c_d^{pl-\varepsilon}(1-\nu^2)}, \qquad (11)$$

where a is the initial crack length, v_o is the impact speed and $c_d^{pl\text{-}\varepsilon}$ is the plane strain dilatational wave speed. Time *(t)* is normalized with $a/c_d^{pl\text{-}\varepsilon}$.

Numerical simulation was carried out using LS-DYNA and the stress intensity factors, $K_I^d(t)$ and $K_{II}^d(t)$, were extracted using Eq. (8). The numerically obtained dynamic stress intensity factors along with corresponding solutions from Lee and Freund are plotted in Figures 29 and 30. The result for $K_{II}^d(t)/K'$ agrees very well with the results of Lee and Freund (1990) from impact to a normalized time of 3. The result for $K_I^d(t)/K'$ agrees very well with the result of Lee and Freund (1990) from the time of impact to a normalized time of 2. The discrepancies in the stress intensity factors between the current study and Lee and Freund's for longer times after impact may be due to the waves reaching the crack tip carrying information about the existence of free boundaries. This validation study provides confidence in the values obtained for the dynamic stress intensity factors using the procedure outlined in Section 3.3.4.

3.3.5 RESULTS AND DISCUSSION

Figure 31 shows a series of stress contour plots of σ_{22} (normal stress which contributes to the evolution $K_I^d(t)$) for a typical simulation (three point bend loading condition, with l=72.6mm (Figure 4) with impact velocity being 40 m/s). A series of stress contour plots of σ_{12} (shear stress which contributes to the evolution of $K_{II}^d(t)$) is

shown in Figure 32. From such plots, one can be informed about the evolution of the stress intensity factors and their region of dominance at the crack tip.

Figure 33 illustrates the time history of relative nodal displacements, $\Delta u_1(t)$ and $\Delta u_2(t)$, at a distance of 6.15 mm from the crack tip and is used to construct the mixed mode dynamic stress intensity factors for a typical simulation. From the relative displacements shown in Figure 33, using the method outlined in Section 3.3.4, the mixed mode dynamic stress intensity factors, $K_I^d(t)$ and $K_{II}^d(t)$ are computed, and hence $K_{eff}^d(t)$. Figure 34 shows the time history of the mixed mode dynamic stress intensity factors. As one can see, $K_{eff}^d(t)$ is fairly linear. By taking the slope of the linear portion of $K_{eff}^d(t)$, an effective loading rate, $\dot{K}_{eff}^d(t)$, is determined, which in this case is $6.8\times10^5 MPa\sqrt{m}/s$. The mode mixity, $\phi(t)$, for this particular case is plotted as a function time in Figure 35. As shown by the figure, $\phi(t)$ varies before 40 μs and approaches a constant value of about 60° after 45 μs. This provides information on the possible mode mixity at the time of initiation for this particular impact loading condition.

Mode I stress intensity factors obtained from numerical analysis and experiment results are plotted in Figure 36 for a typical experiment. The experimental impact velocity is 40 m/s and the support condition is a modified single edge notched configuration with *b=76.2* mm (Figure 5). The figure shows reasonably good agreement between the experiment and the simulation. Similar observation is also made for mode II stress intensity factor, $K_{II}^d(t)$, and is shown in Figure 37. Mode mixity, $\phi(t)$, as a

function of time for both simulation and experiment is presented in Figure 38. For most of the experiments, the numerical simulations agree very well with the experimental results. The small differences between experimental and numerical results can be attributed to the differences in boundary conditions such as the support condition.

3.4. Conclusions

Experiments have been conducted using single edge notched specimens and three point bend specimens made of aluminum 2024-T3 alloy to obtain mixed mode dynamic initiation toughness. The optical technique of CGS and method of strain gages were simultaneously employed to obtain the evolution of dynamic stress intensity factors. A range of mode mixities were achieved by varying the impact locations for the single notched and three point bend specimens at a loading rate of approximately $7\times10^5 MPa\sqrt{m}/s$. A mixed mode failure envelope was developed for this particular loading rate and is shown in Figure 13. This failure envelope lies inside of the static one for the same material presented by Chao and Liu (1997). This implies that the design using the static failure envelope for structures subjected to dynamic loading conditions (e.g., explosively loaded aircraft fuselages) can be non-conservative and even dangerous. The fact that the dynamic envelope falls within the static one for the loading rate of $7\times10^5 MPa\sqrt{m}/s$ may be explained by the contribution of thermal softening effects.

Fractographs near the crack initiation site on the specimens using SEM were obtained for selected experiments covering the whole range of mode mixity. The fracture

surfaces from the experiments that were close to mode I loading had large circular primary voids, while the ones from experiments close to mode II loading had small, sheared secondary void sheets and sheared inclusions. It is apparent that different microscopic failure mechanisms cause failure at different dynamic mode mixties.

Numerical simulations were conducted using a commercial finite element code, LS-DYNA, for the purpose of designing and validating the experiments. Elastic analyses were carried out with the assumption of small scale yielding. The numerical method of obtaining dynamic stress intensity factor was validated by comparing it with the theoretical and numerical studies of Lee and Freund (1990). The results from the numerical simulations matched well with the experimental result. This further provides confidence in the experimental techniques used for the mixed mode dynamic crack initiation experiments and justifies the use of the numerical simulations to design this type of experiment, thus saving time and experimental resources.

Reference

Chao, Y.J. and Liu. S., 1997. On the failure of Cracks Under Mixed-mode Loads. *International Journal of Fracture* 87: 201-223.

Chow B., Rosakis, A.J. and Ravichandran, 2001. G. A Dynamic Fracture Mechanics Approach to the Estimation of Residual Strength of Impulsively Loaded Structures: Part I Experiments and Theoretical Methodology. *Solid Mechanics Report SM01-03, GALCIT*, California Institute of Technology, Pasadena, California, USA.

Costin, L.S. and Duffy, J., 1979. The Effect of Loading Rate and Temperature on The Initiation of Fracture in a Mild, Rate Sensitive Steel. *Journal of Engineering Materials and Technology*, 101, 258-264.

Costin, L.S., Crisman, E.E., Hawley, R.H. and Duffy, J., 1979. On the localization of plastic flow in mild steel tubes under torsional loading. *2nd Conference on the Mechanical Properties of Materials at High Rates of Strain (Ed. Harding, J.)* The Institute of Physics, London, 90-100.

Freund, L.B., Wu, F.H. and Toulios, M., 1985. Initiation and propagation of shear band in antiplane shear deformation. *Proceedings of the Considere Memorial Symposium*, 125-143, Presse de l'Ecole Nationale des Ponts et Chaussees.

Grady, D.E., 1992. Properties of an adiabatic shear band process zone. *J Mech. Phys. Solids.* 40, 1197-1215.

Guduru, P.R., Singh, R.P., Ravichandran, G. and Rosakis, A.J., 1998. Dynamic crack initiation in ductile steels. *J. Mech. Phys. Solids.* 46, 1997-2016.

He, M.-Y. and Hutchinson, J.W., 1989. Kinking of crack out of an interface. *J. Appl. Mech.* **56**, 270-278.

Hodowany, J., Ravichandran, G., Rosakis, A.J. and Rosakis, P., 2000. Partition of plastic work into heat and stored energy in metals. *Exper. Mech.* 40, 113-123.

Kalthoff, J.K. and Winkler, S., 1988. Failure mode transition at high rates of loading, *Proceedings of the international conference on impact loading and dynamic behaviour of materials* (Ed. C.Y. Chiem, H.D. Kunze and L.W. Meyer) 43-56, Deutsche Gesellshaft fur Metallkunde.

Lee, Y.J. and Freund, L.B., 1990. Fracture initiation due to asymmetric impact loading of an edge cracked plate, *J. Mech. Phys. Solids.* 57, 104-111.

Li, Z. and Lambros, J., 2000. Dynamic thermomechanical behavior of fiber reinforced composites. Composites, Part A – *Appl. Sci. Manufact.* 31, 537-547.

Livermore Software Technology Corporations, 1995. LS-DYNA Keyword User's Manual, Version 950.

Livermore Software Technology Corporations, 1995. LS-DYNA Theoretical Manual, Version 950.

Marchand, A. and Duffy, J., 1988. An experimental study of the formation process of adiabatic shear bands in a structural steel. *J. Mech. Phys. Solids.* 36, 251-283.

Mason, J.J., Lambros, J. and Rosakis, A.J., 1992. The use of a coherent gradient sensor in dynamic mixed mode fracture mechanics experiments. *J. Mech. Phys. Solids.* 40, 641-661.

Mason, J.J. and Rosakis, A.J., 1993. On the dependence of the dynamic crack-tip temperature fields in metals upon crack-tip velocity and material parameters. *Mech. Mater.* 16, 337-350.

Meyers, M.A., 1994. *Dynamic behavior of Materials.* John Wiley & Sons, New York.

Moss, G. and Pond Sr., R.B., 1975. Inhomogeneous thermal changes in copper during plastic elongation. *Metall. Trans.* 6A, 1223-1235.

Palisniswami, K. and Knauss, W.G.,1978. On the Problem of Crack Extension in Brittle Solids Under General Loading. *Mechanics of Today* 4,87-148.

Ravi-Chandar, K., 1995. On the failure mode transition in polycarbonate under dynamic mixed mode loading. *Int. J. Solid. Struct.* 32, 925-938.

Ravi-Chandar, K., Lu, J., Yang, B. and Zhu, Z., 2000. Failure mode transitions in polymers under high strain rate loading. *Int. J. Fract.* 101, 33-72.

Recht, R.F., 1964. Catastrophic thermoplastic shear. *J. Appl. Mech.* 31, 189-193.

Richard, H.A., 1987. Crack Problems Under Complex Loading. *Role of Fracture Mechanics in Modern Technology* (Ed. Sih, G.C., Nisitani, H., and Ishihara, T.) Elsevier Science Publishers B.V. (North-Holland), 577-588.

Rittel, D. and Levin, R., 1998. Mode-mixity and dynamic failure mode transitions in polycarbonate. *Mech. Mater.* 30, 197-216.

Roessig, K.M. and Mason, J.J., 1998. Adiabatic shear localization in the impact of edge-notched specimens. *Exper. Mech.* 38, 196-203.

Rogers, H.C., 1979. Adiabatic plastic deformation. *Ann. Rev. Mater.* Sci 9, 283-311.

Rosakis, A.J., 1993. Two optical techniques sensitive to gradients of optical path difference: the method of caustics and the coherent gradient sensor (CGS). In: *Experimental Techniques in Fracture* (Ed. Epstein, J.), VCH, New York, 327-425.

Shawki, T.G. and Clifton, R.J., 1989. Shear band formation in thermal viscoplastic materials. *Mech. Mater.* 8, 13-43.

Tippur, H.V., Krishnaswamy, S. and Rosakis, A.J., 1990. Coherent gradient sensor for crack tip deformation measurements: analysis and experimental results. *Int. J. Fract.* 48, 193-204.

Tippur, H.V., Krishnaswamy, S. and Rosakis, A.J., 1991. Optical mapping of crack tip deformations using the method of transmission and reflection coherent gradient sensing: a study of crack tip *k*-dominance. *Int. J. Fract.* 52, 91-117.

Vankert, A., Guduru, P.R., Ravichandran, G., 2000. An Investigation of Dunamic Failure in 2.3Ni-1.3Cr-0.17C Steel. *Metallurgical and Materials Transaction A* 31A, 1147-1154.

Wright, T.W., 1987. Steady shearing in a viscoplastic solid. *J. Mech. Phys. Solids.* 35, 269-282.

Wright, T.W., 1995. Scaling laws for adiabatic shear bands. *Int. J. Solids. Struct.* 32, 2745-2750.

Wright, T.W. and Ockendon, H., 1992. A model for fully formed shear bands. *J. Mech. Phys. Solids.* 40, 1217-1226.

Wright, T.W. and Ravichandran, G., 1997. Canonical aspects of adiabatic shear bands. *Int. J. Plasticity.* 13, 309-325.

Wu, F.H. and Freund, L.B., 1984. Deformation trapping due to thermoplastic instability in one-dimensional wave-propagation. *J. Mech. Phys. Solids*. 32, 119-132.

Zhou, M., Ravichandran, G. and Rosakis, A.J., 1996a. Dynamically propagating shear bands in impact-loaded prenotched plates – I. Experimental investigations of temperature signatures and propagation speed. *J. Mech. Phys. Solids*. 44, 981-1006.

Zhou, M., Ravichandran, G. and Rosakis, A.J., 1996b. Dynamically propagating shear bands in impact-loaded prenotched plates – II. Numerical simulations. *J. Mech. Phys. Solids*. 44, 1007-1032.

List of figures

Figure 8. Schematics of the strain gage diagnostic tool for measuring the mixed mode dynamic stress intensity factors.

Figure 9. A series of CGS images for a typical dynamic mixed mode initiation experiments using a modified single edge notch specimen, impact velocity of 40 m/s.

Figure 10. Mixed mode dynamic stress intensity factors as a function of time obtained by analyzing the CGS images shown in Figure 9 for a modified single edge notched specimen.

Figure 11. Strain gage signal from a typical dynamic mixed mode initiation experiment for a modified single edge notched specimen, impact velocity of 40 m/s.

Figure 12. Mixed mode dynamic stress intensity factors as a function of time obtained from strain gage signal from a typical dynamic mixed mode initiation experiments using a modified single edge notched specimen, impact velocity of 40 m/s.

Figure 13. Dynamic failure envelope consists of mixed mode dynamic stress intensity factors for 2024-T3 aluminum alloy obtained from the current study for the loading rate of $7\times10^5 MPa\sqrt{m}/s$.

Figure 14. Dynamic failure envelope of 2024-T3 aluminum alloy for the loading rate of $7\times10^5 MPa\sqrt{m}/s$ compared with the static results of Chao and Liu (1995).

Figure 15. Fitted static and dynamic failure envelope curves for the 2024-T3 aluminum alloy using equations presented by Richard (1987)

Figure 16. Fractographs of different magnifications near the crack initiation surface for a dynamic mode I experiment.

Figure 17. Fractographs of different magnifications near the crack initiation surface for a dynamic mixed mode experiment ($K_I^d = 23.86\ MPa\sqrt{m}$, $K_I^d = 13.54\ MPa\sqrt{m}$, $\phi = 29.57°$).

Figure 18. Fractographs of different magnifications near the crack initiation surface for a dynamic mixed mode experiment ($K_I^d = 22.68\ MPa\sqrt{m}$, $K_I^d = 18.84\ MPa\sqrt{m}$, $\phi = 39.72°$).

Figure 19. Fractographs of different magnifications near the crack initiation surface for a dynamic mixed mode experiment ($K_I^d = 17.30\ MPa\sqrt{m}$, $K_I^d = 19.95\ MPa\sqrt{m}$, $\phi = 49.06°$).

Figure 20. Fractographs of different magnifications near the crack initiation surface for a dynamic mixed mode experiment ($K_I^d = 14.18\ MPa\sqrt{m}$, $K_I^d = 22.75\ MPa\sqrt{m}$, $\phi = 58.07°$).

Figure 21. Fractographs of different magnifications near the crack initiation surface for a dynamic mixed mode experiment ($K_I^d = 11.14 MPa\sqrt{m}$, $K_I^d = 20.80\ MPa\sqrt{m}$, $\phi = 61.83°$).

Figure 22. Fractographs of different magnifications illustrating the features of shearing failure in precipitates for a mixed mode case ($K_I^d = 11.14 MPa\sqrt{m}$, $K_I^d = 20.80\ MPa\sqrt{m}$, $\phi = 61.83°$).

Figure 23. A comparison between the crack tip fractographic features through selected micrographs for the two cases of dynamic failure: mode I and mode II dominated case.

Figure 24. A typical three dimensional LS-DYNA finite element mesh for the simulation of a dynamic mixed mode impact experiment.

Figure 25. Elastic-plastic stress vs. strain curve for aluminum 2024-T3 alloy (adapted from Hodowany *et al.*, 2000).

Figure 26. A schematic of the crack tip deformations under mixed mode loading conditions.

Figure 27. Schematics of (a) loading geometry used by Kalthoff and Winkler (1998); (b) theoretical and (c) numerical investigations by Lee and Freund (1990).

Figure 28. The LS-DYNA finite element mesh used in the validation study of the proposed extraction method of determining mixed mode dynamic stress intensity factors.

Figure 29. Result of the validation studies comparing results of the current methodology with the theoretical and numerical studies of Lee and Freund (1990) for dynamic mode I stress intensity factor, $K_I^d(t)$.

Figure 30. Result of the validation studies comparing results of the current methodology with the theoretical and numerical studies of Lee and Freund (1990) for dynamic mode I stress intensity factor, $K_{II}^d(t)$.

Figure 31. Stress contour plots of normal stress σ_{22} at different times after impact for a typical numerical simulation for a dynamic mixed mode impact experiment on a three point bend specimen with an impact velocity of 40 m/s.

Figure 32. Stress contour plots of shear stress σ_{12} at different times after impact for a typical numerical simulation for a dynamic mixed mode impact experiment on a three point bend specimen with an impact velocity of 40 m/s.

Figure 33. Time history plots of relative nodal displacement $\Delta u_1(t)$ and $\Delta u_2(t)$ for a pair of nodes 6.15 mm behind the crack tip for a typical numerical simulation for a dynamic mixed mode impact experiment on a three point bend specimen with an impact velocity of 40 m/s.

Figure 34. Time history plots of mixed mode stress intensity factors $K_I^d(t)$ and $K_{II}^d(t)$ obtained from the time histories $\Delta u_1(t)$ and $\Delta u_2(t)$ shown in Figure 33.

Figure 35. Time history plot of mode mixity $\phi(t)$ $(\tan^{-1}(K_{II}^d(t)/K_I^d(t)))$ for a typical numerical simulation for a dynamic mixed mode impact experiment on a three point bend specimen with an impact velocity of 40 m/s.

Figure 36. Comparison between numerically and experimentally obtained mode I stress intensity factors $K_I^d(t)$ for a dynamic mixed mode impact experiment on a three point bend specimen with an impact velocity of 40 m/s.

Figure 37. Comparison between numerically and experimentally obtained mode II stress intensity factors $K_{II}^d(t)$ for a dynamic mixed mode impact experiment on a three point bend specimen with an impact velocity of 40 m/s.

Figure 38. Comparison between numerically and experimentally obtained mode mixity $\phi(t)$ for a dynamic mixed mode impact experiment on a three point bend specimen with an impact velocity of 40 m/s.

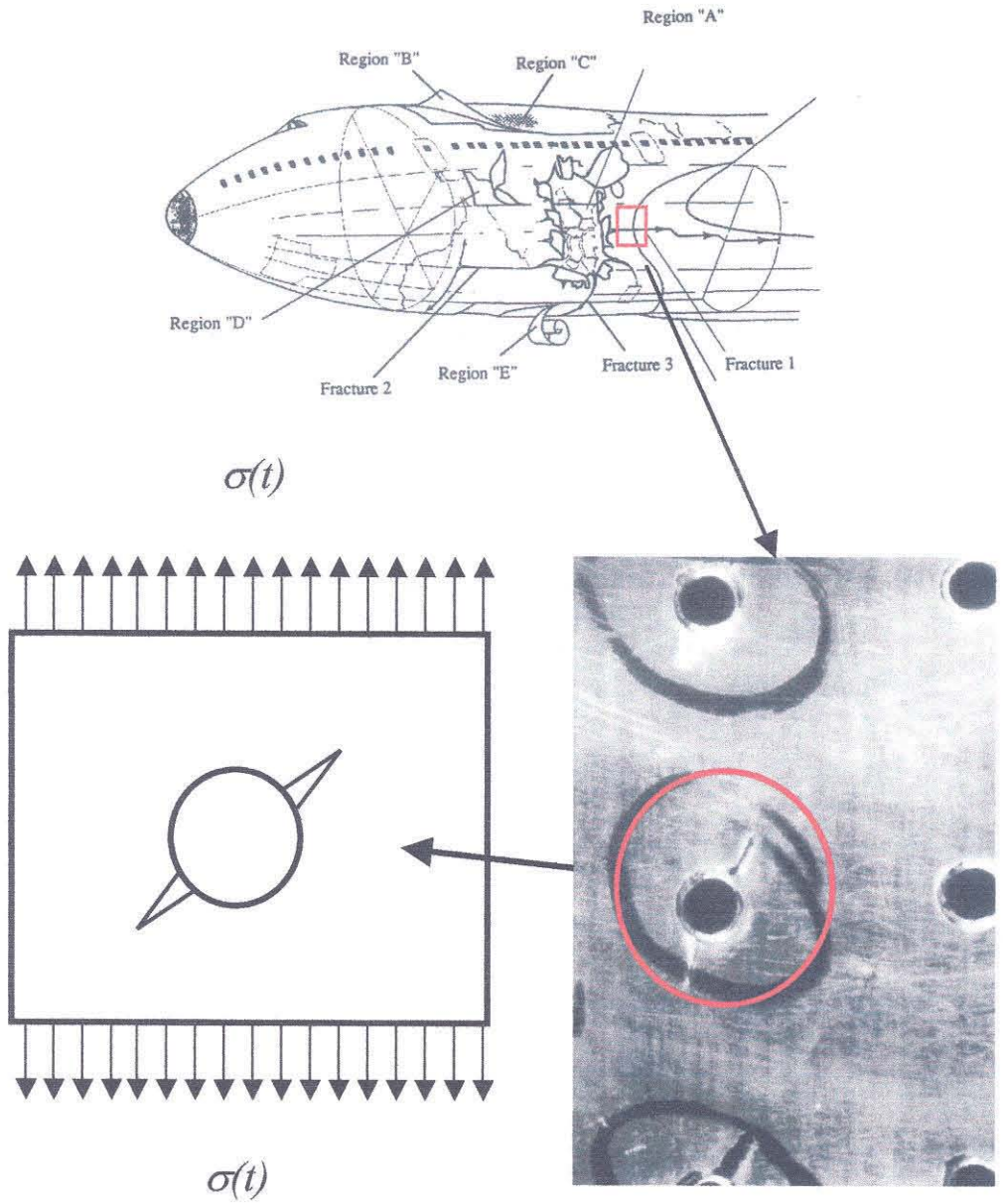
Region "A"
Region "B"
Region "C"
Region "D"
Region "E"
Fracture 1
Fracture 2
Fracture 3
σ(t)
σ(t)

Figure 1

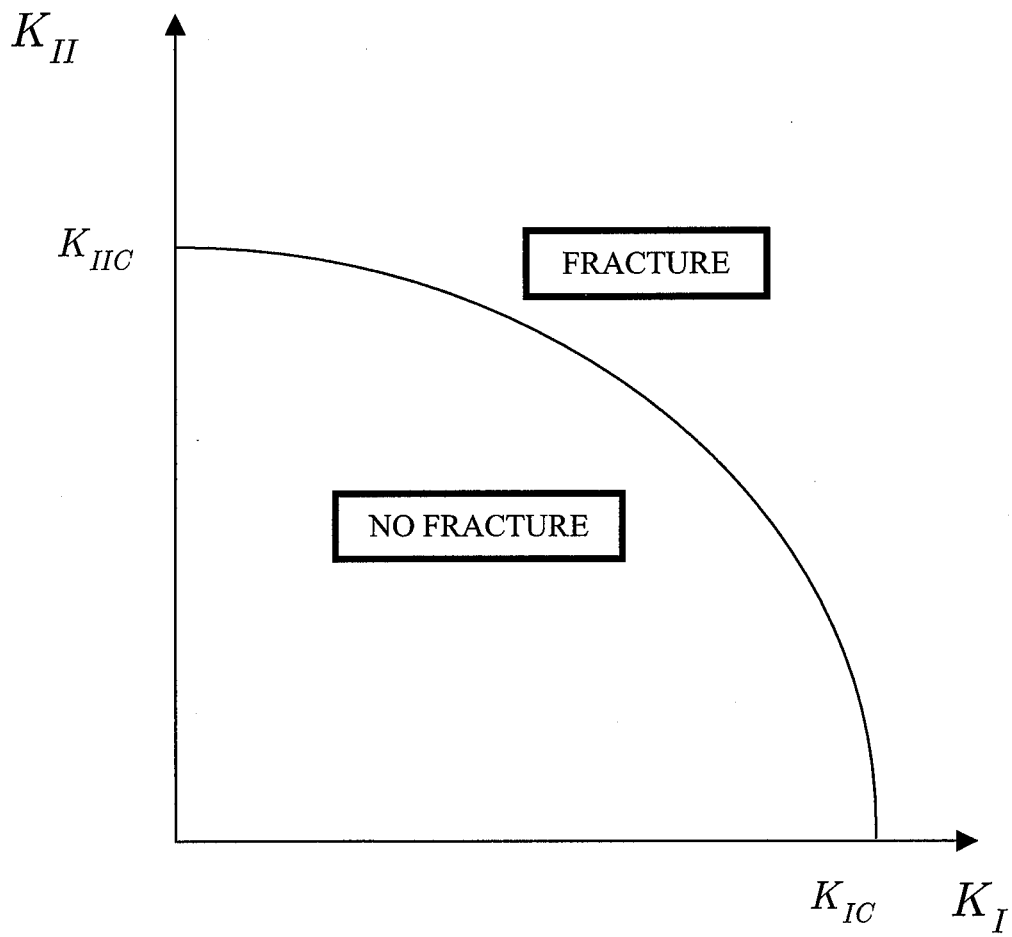

Figure 2

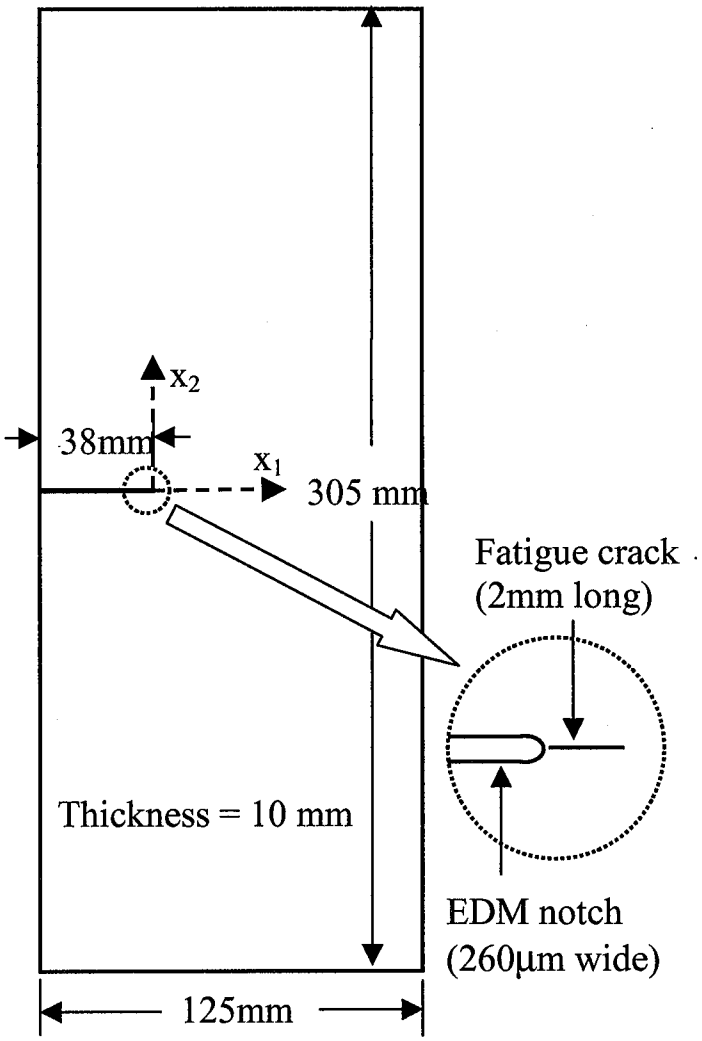
x2
38mm
x1
305 mm
Fatigue crack
(2mm long)
Thickness = 10 mm
EDM notch
(260μm wide)
125mm

Figure 3

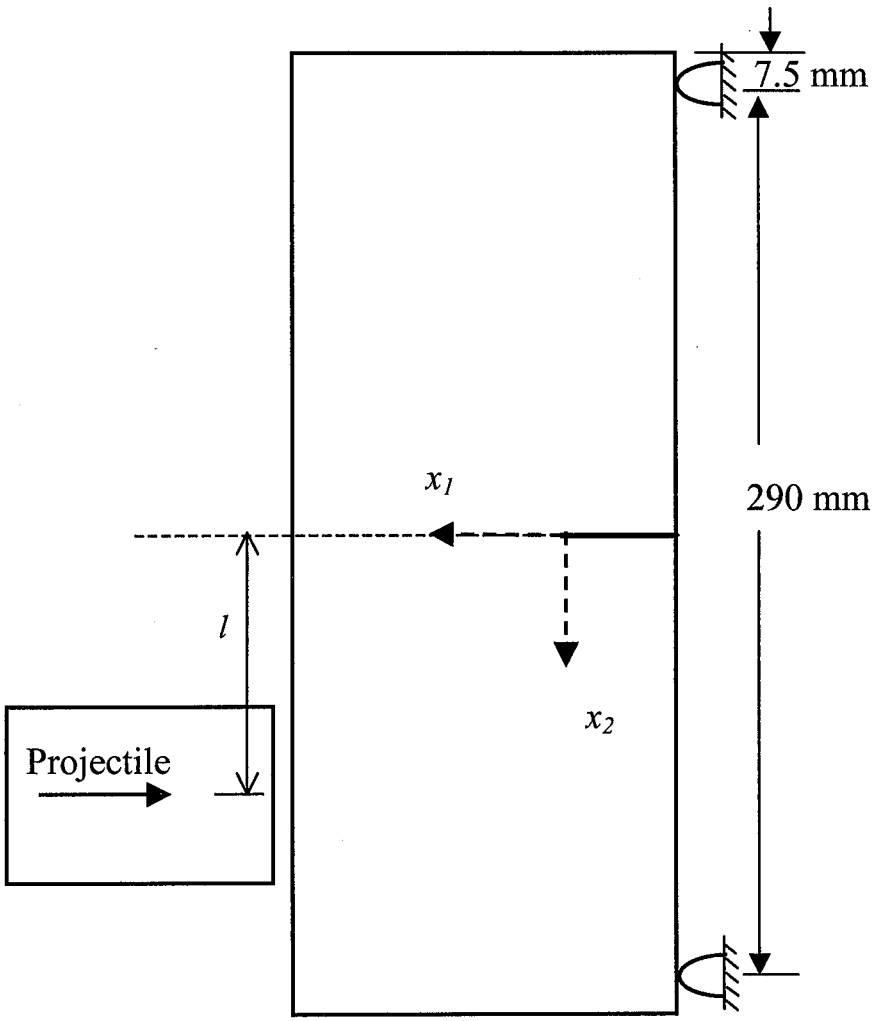

Figure 4

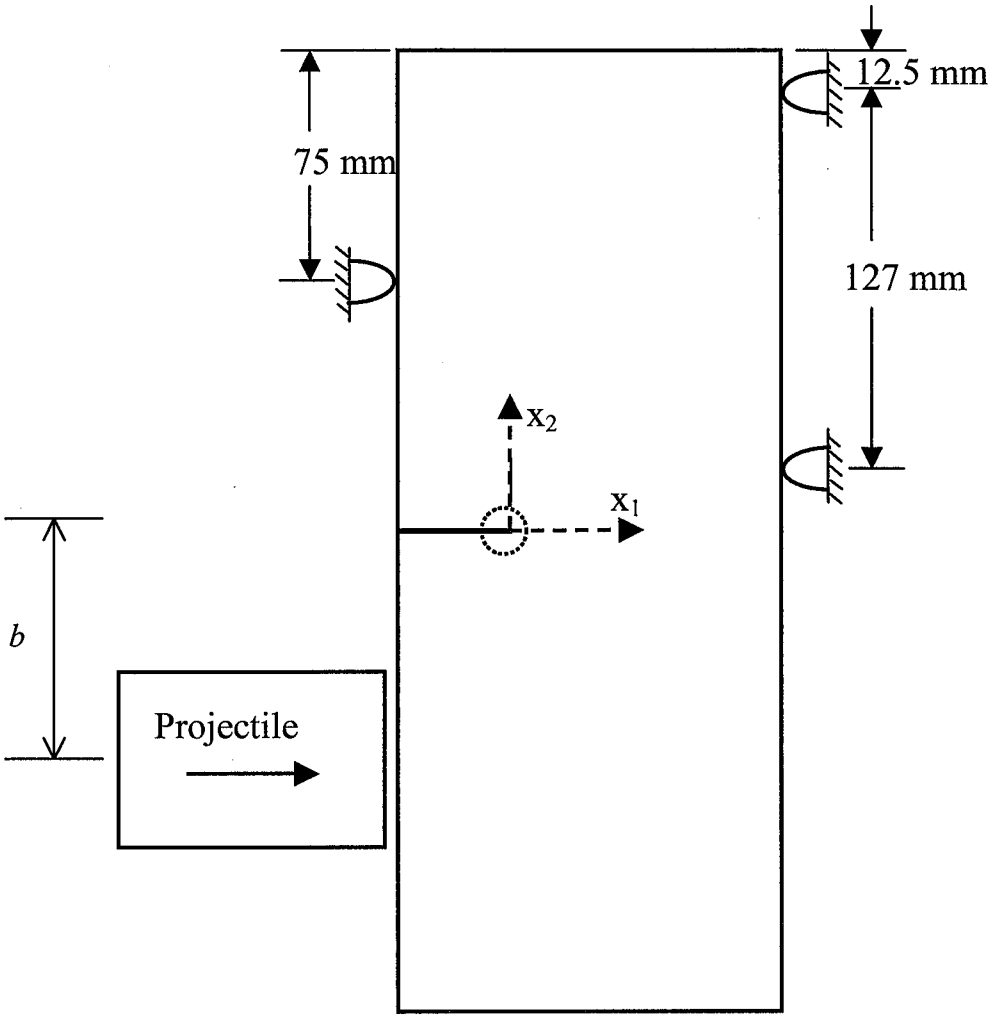

Figure 5

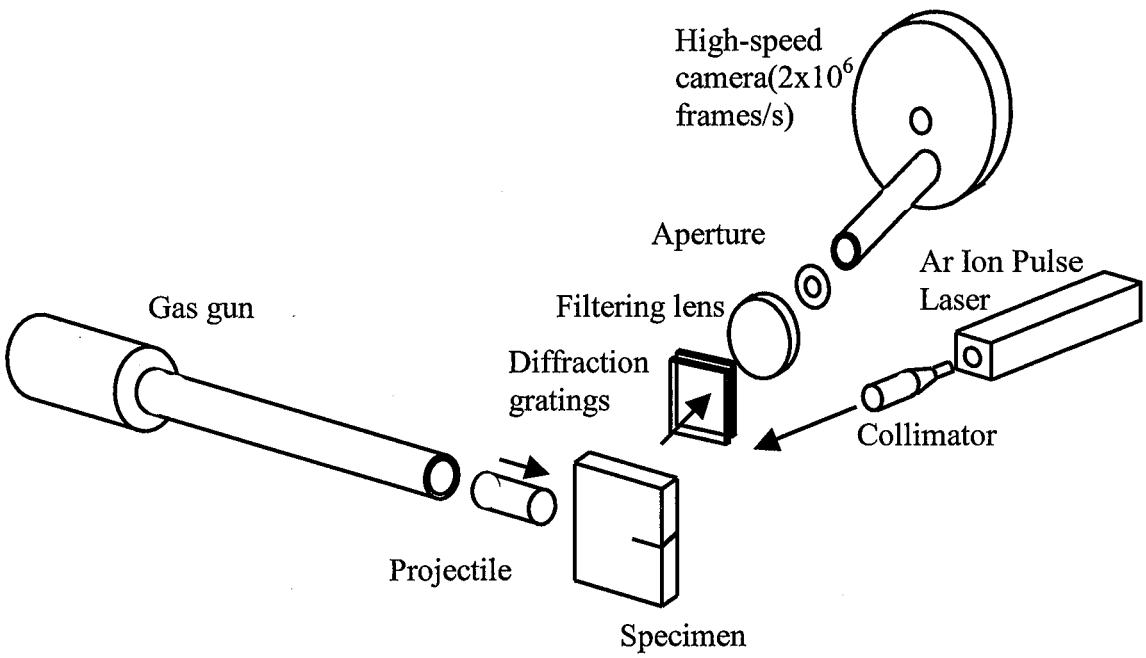
High-speed
camera(2x10^6
frames/s)
Aperture
Ar Ion Pulse
Laser
Gas gun
Filtering lens
Diffraction
gratings
Collimator
Projectile
Specimen

Figure 6

Figure 7

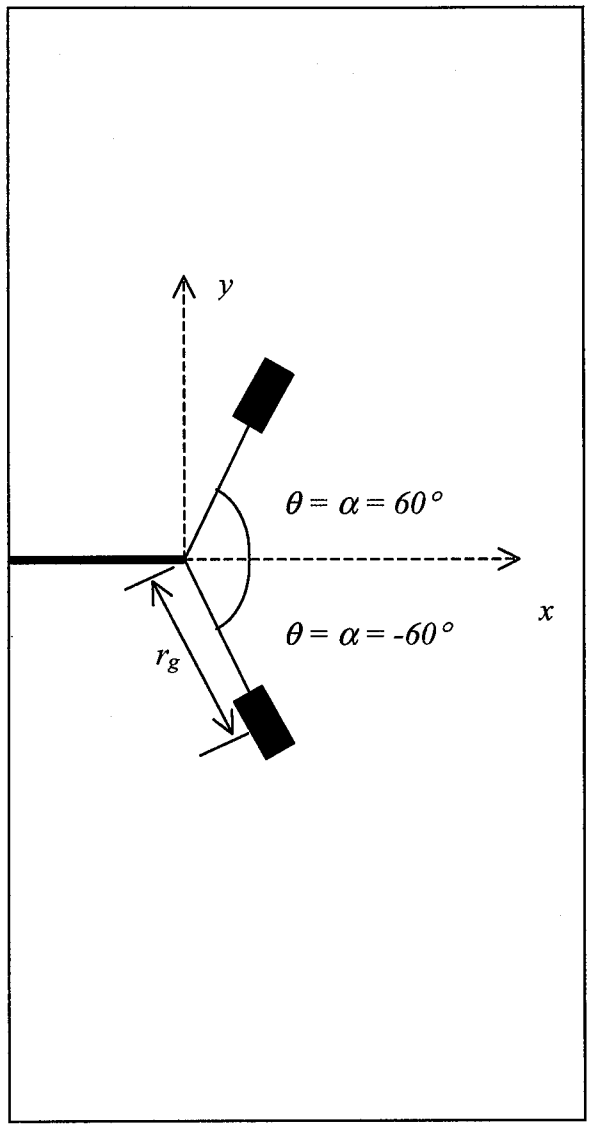

Figure 8

Figure 9

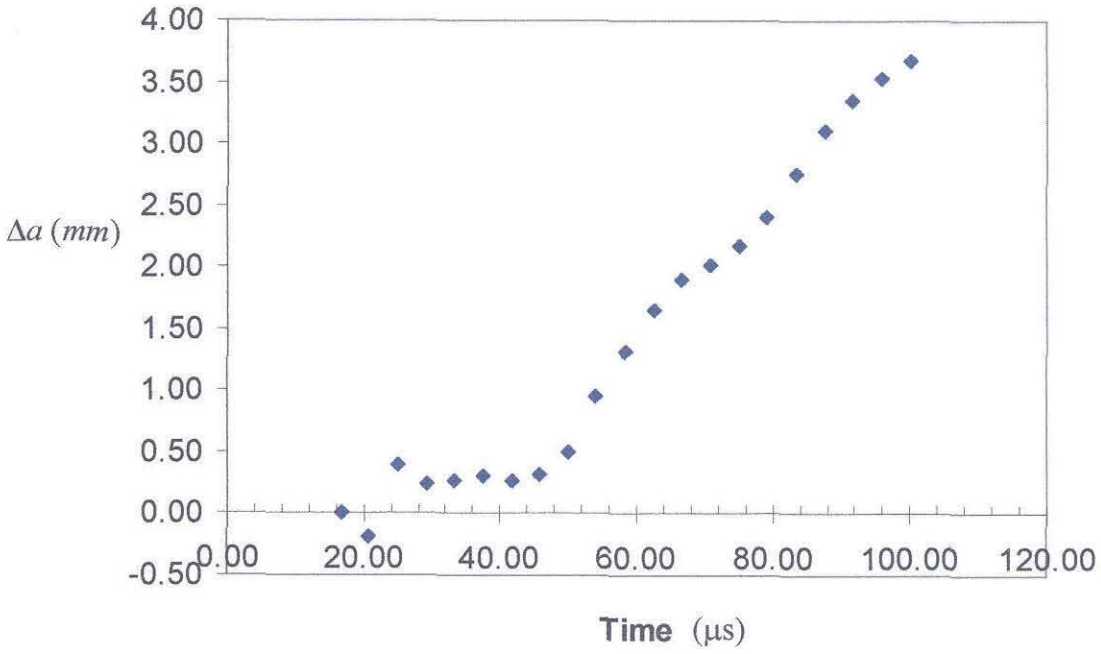
4.00
3.50
3.00
2.50
2.00
1.50
1.00
0.50
0.00
-0.50
Δa (mm)
0.00
20.00
40.00
60.00
80.00
100.00
120.00
Time (μs)

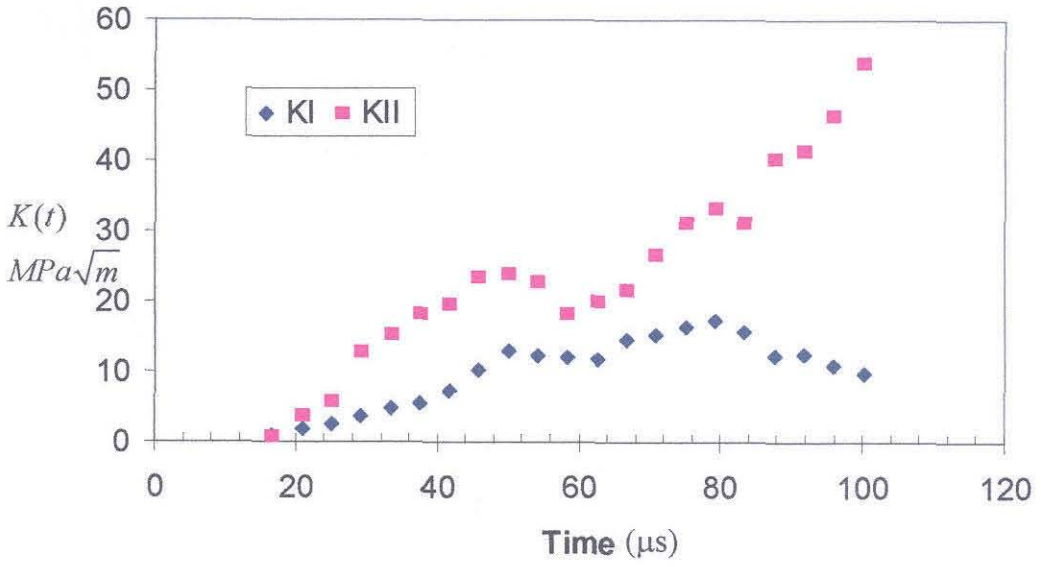
60
50
40
30
20
10
0
KI
KII
K(t)
MPa√m
0
20
40
60
80
100
120
Time (μs)

Figure 10

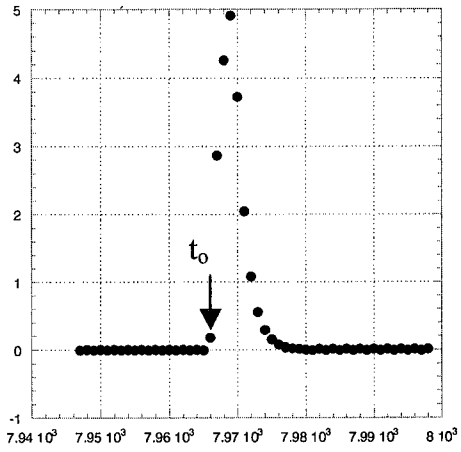
5
4
3
2
1
0
-1
t_o
7.94 10³
7.95 10³
7.96 10³
7.97 10³
7.98 10³
7.99 10³
8 10³
Time (μs)

(a)

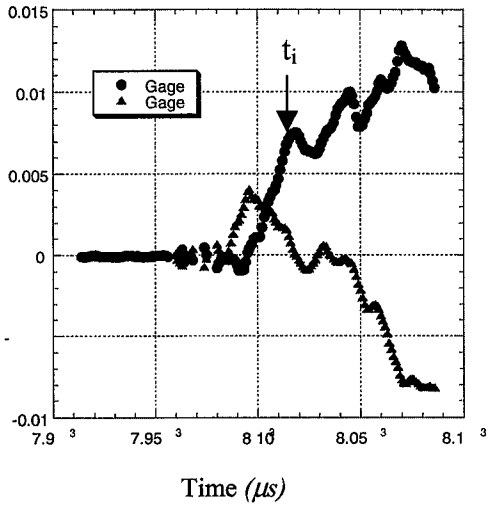
0.015
0.01
0.005
0
-0.01
Gage
Gage
t_i
7.9 ³
7.95 ³
8.05 ³
8.1 ³
Time (μs)

(b)

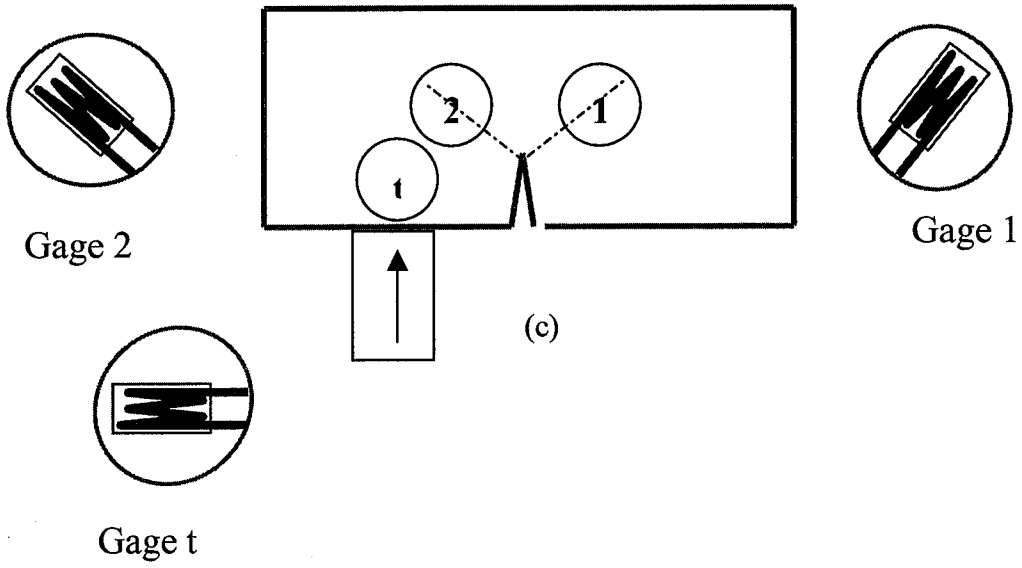
2
1
t
Gage 2
Gage 1
Gage t
(c)

Figure 11

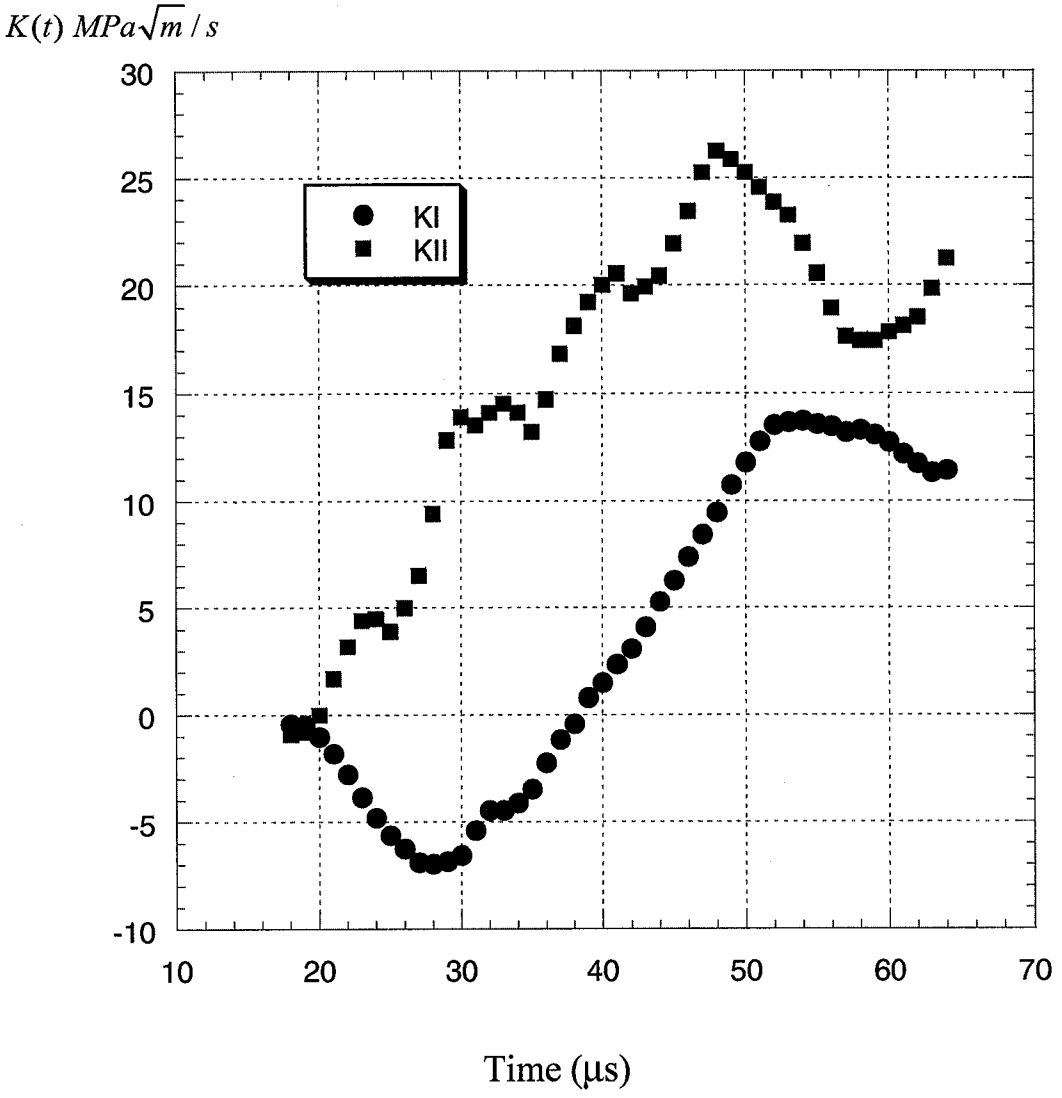
$K(t)\ MPa\sqrt{m}\ /\ s$
30
25
20
15
10
5
0
-5
-10
10
20
30
40
50
60
70
KI
KII
Time (μs)

Figure 12

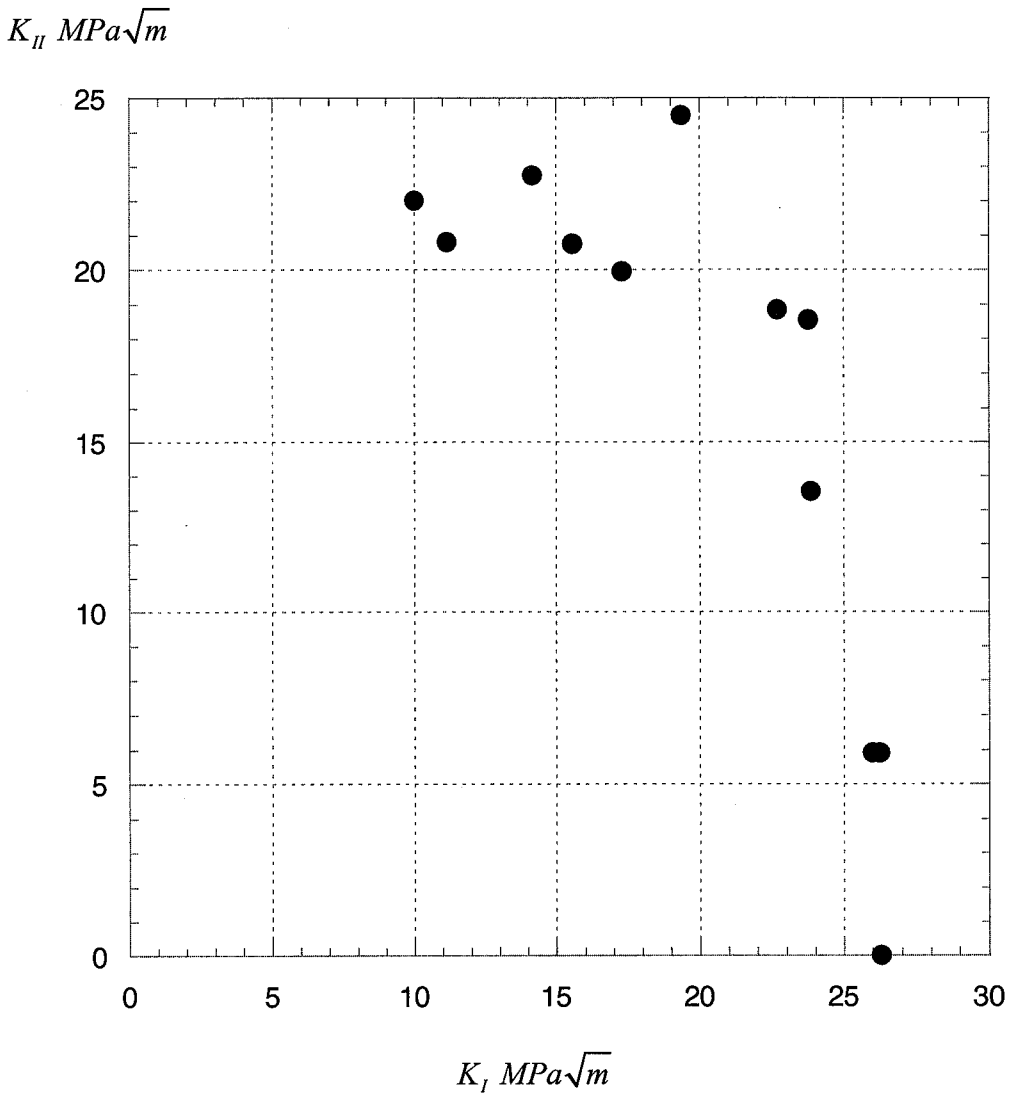

Figure 13

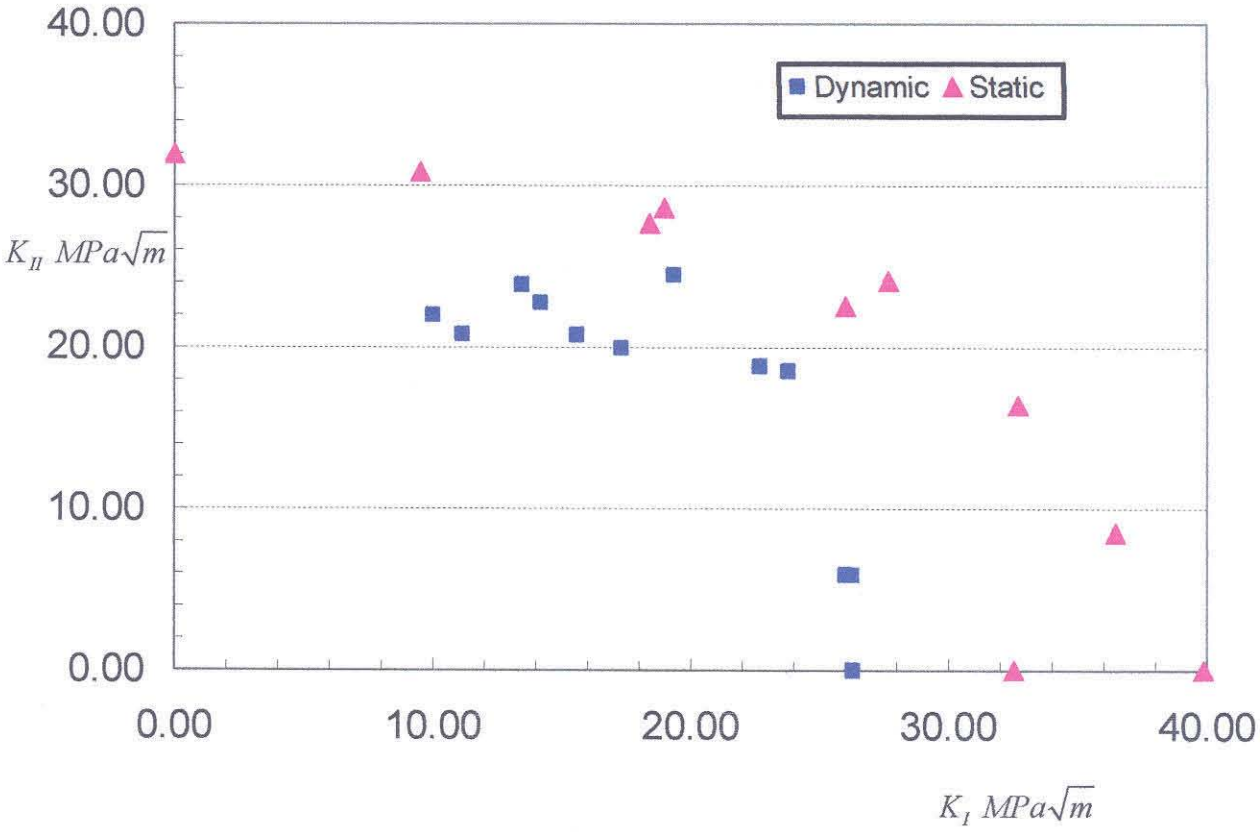
40.00
30.00
20.00
10.00
0.00
K_{II} $MPa\sqrt{m}$
Dynamic
Static
0.00
10.00
20.00
30.00
40.00
K_I $MPa\sqrt{m}$

Figure 14

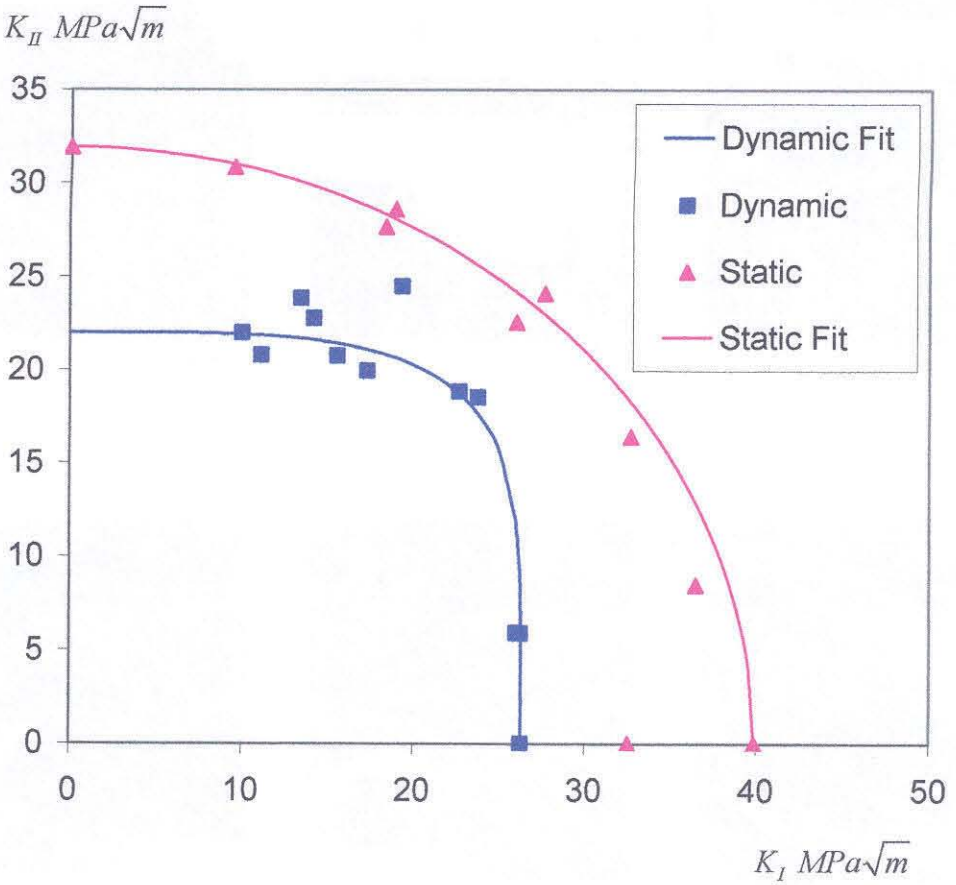
K_{II} $MPa\sqrt{m}$
35
30
25
20
15
10
5
0
0
10
20
30
40
50
K_I $MPa\sqrt{m}$
Dynamic Fit
Dynamic
Static
Static Fit

Figure 15


1mm 89X

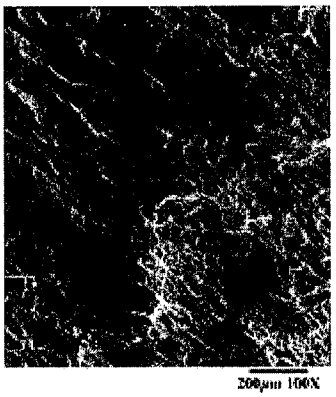
200µm 100X

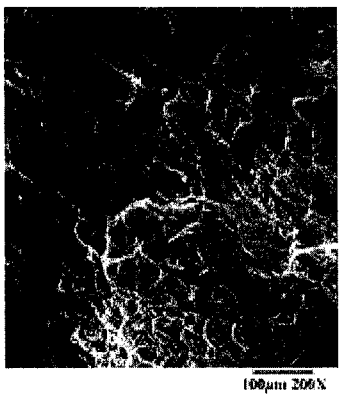
100µm 200X

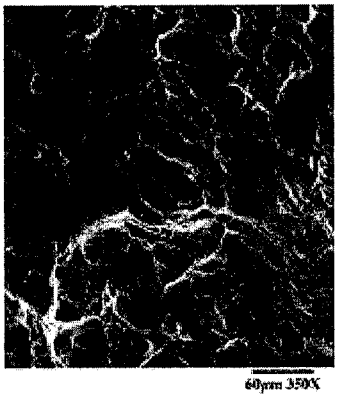
60µm 350X

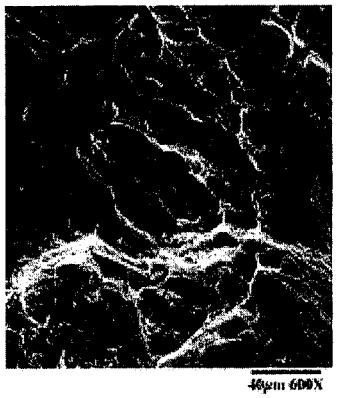
40µm 600X


10µm 1500X

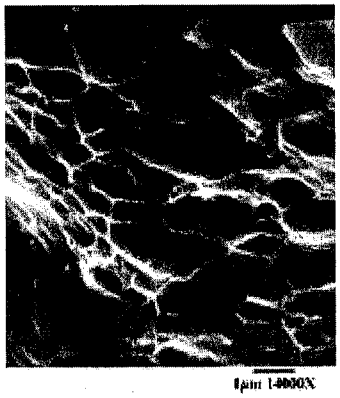
1µm 14000X

Figure 16

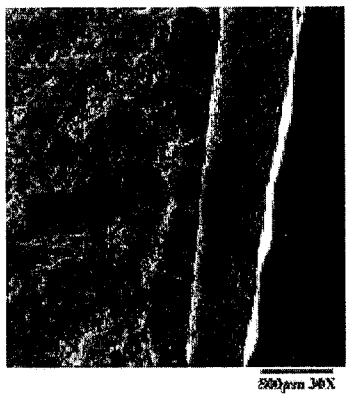
500μm 30X


200μm 100X

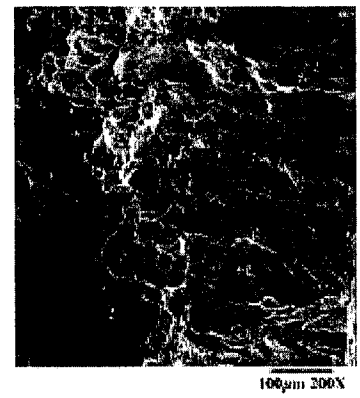
100μm 200X

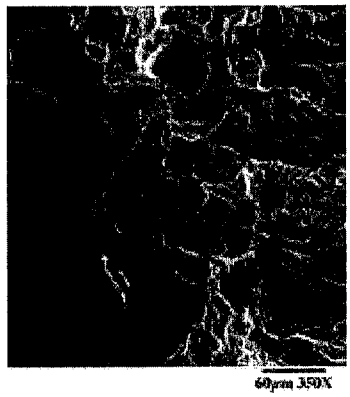
60μm 350X

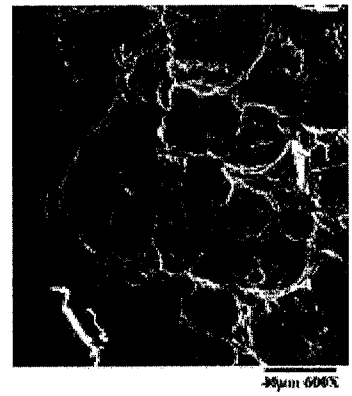
30μm 600X

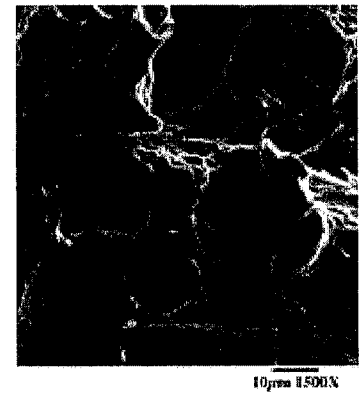
10μm 1500X

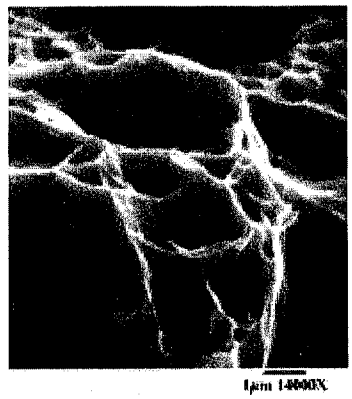
1μm 14000X

Figure 17

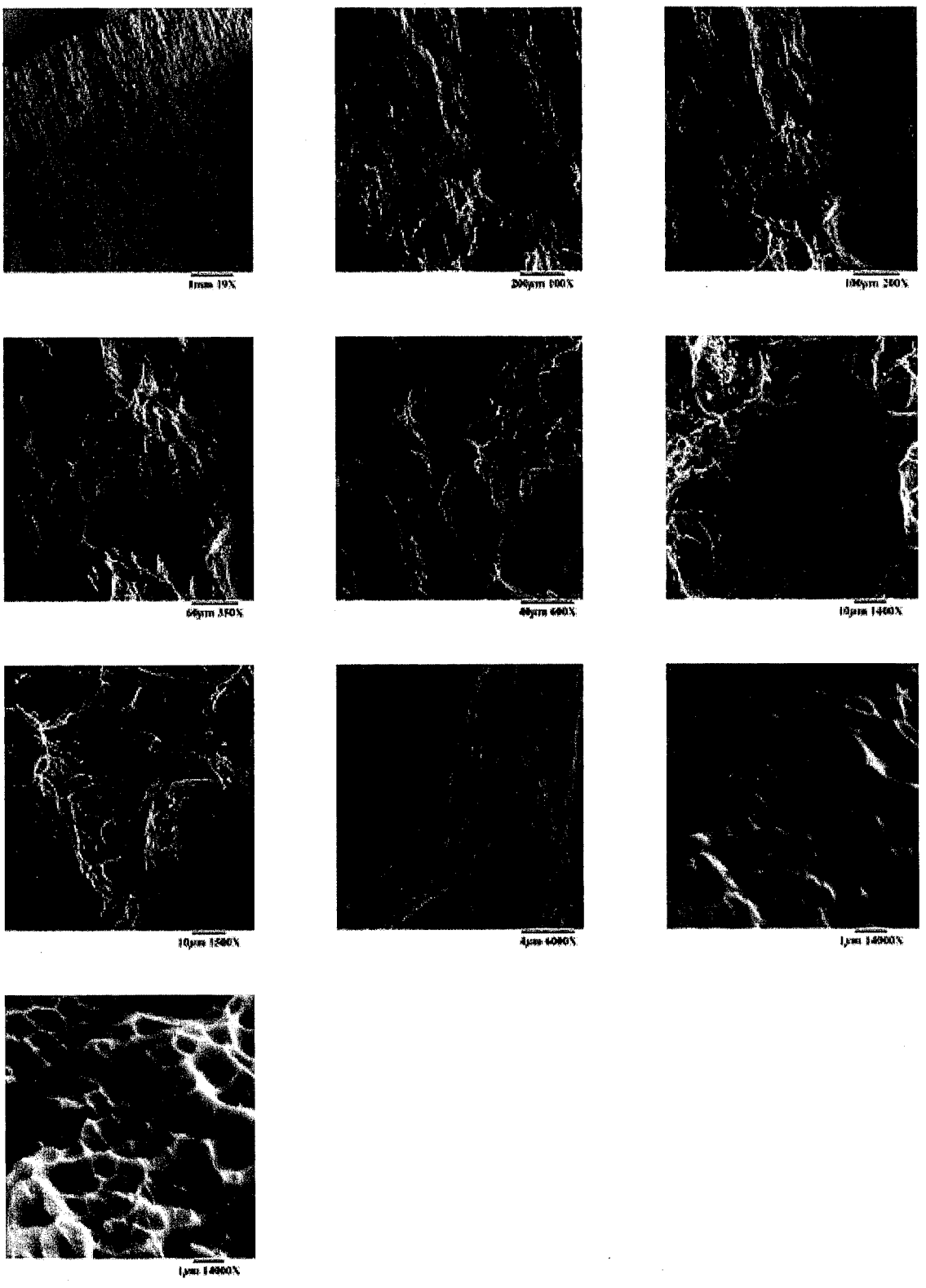

Figure 18


500μm 30X

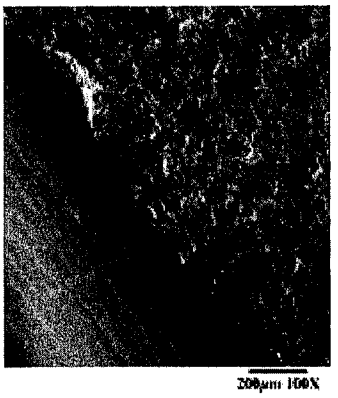
200μm 100X

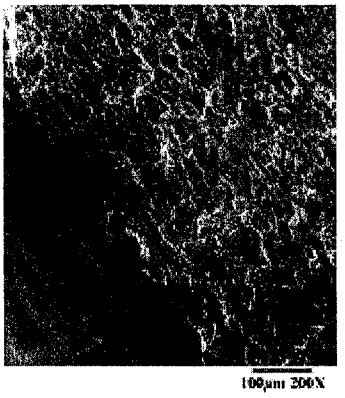
100μm 200X

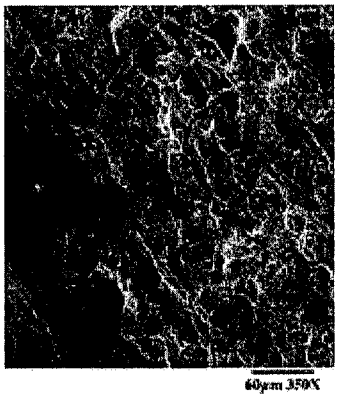
60μm 350X

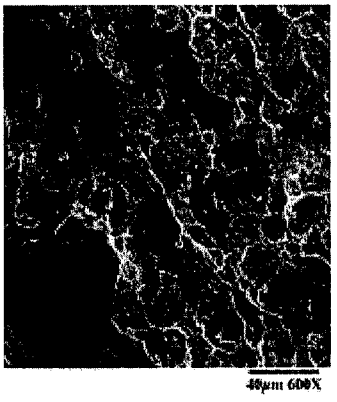
40μm 600X

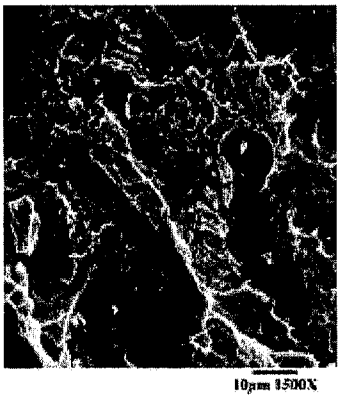
10μm 1500X

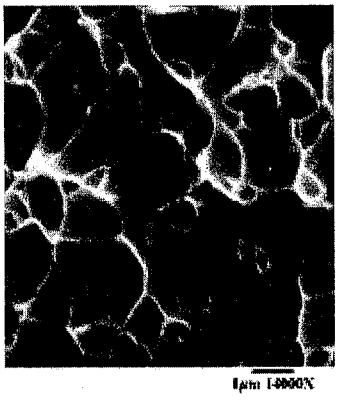
1μm 14000X

Figure 19

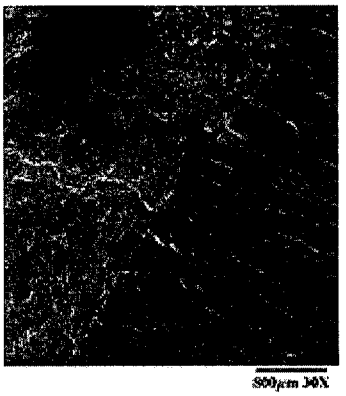
800μm 30X

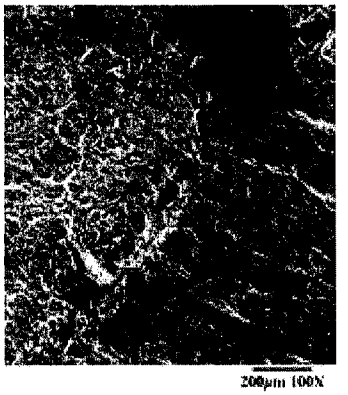
200μm 100X

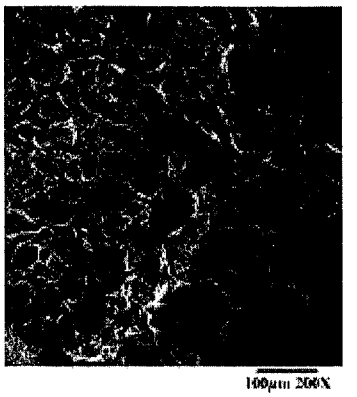
100μm 200X

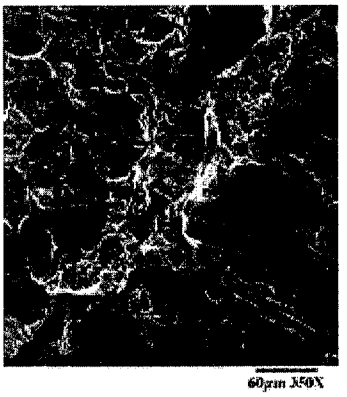
60μm 350X

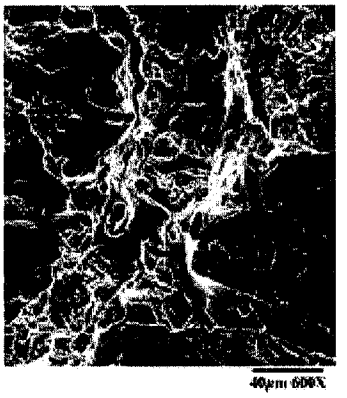
40μm 600X

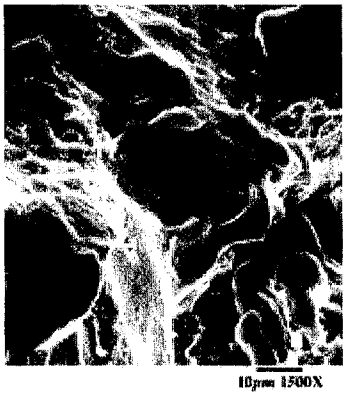
10μm 1500X

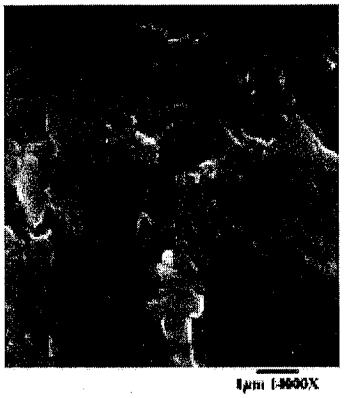
1μm 14000X

Figure 20


800μm 30X

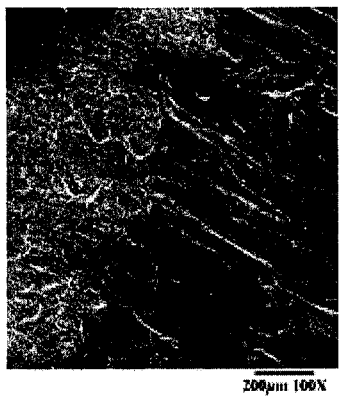
200μm 100X

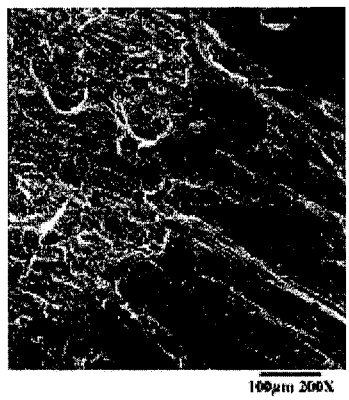
100μm 200X

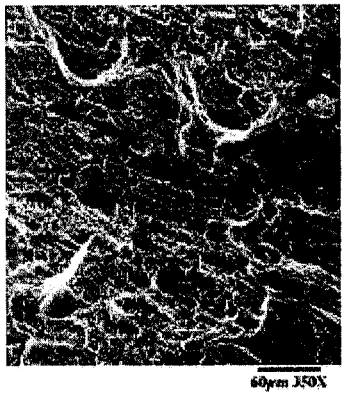
60μm 350X

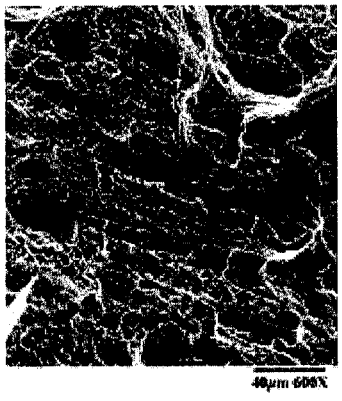
40μm 600X

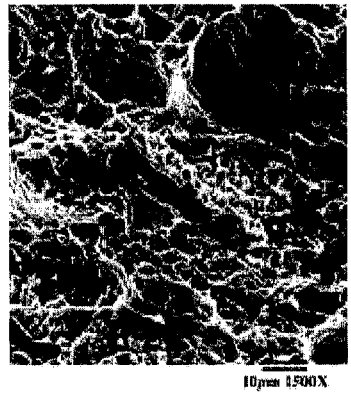
10μm 1500X


1μm 14000X

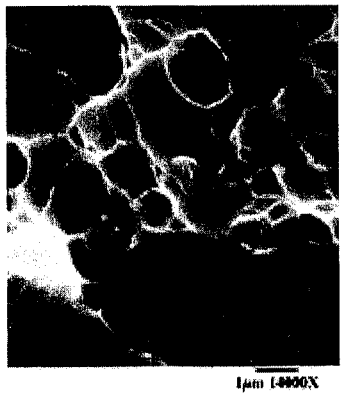
1μm 14000X

Figure 21

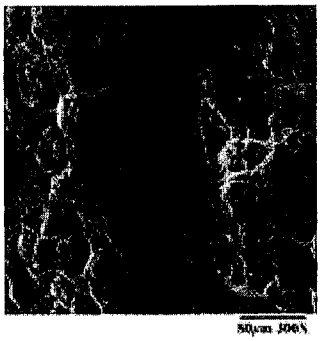

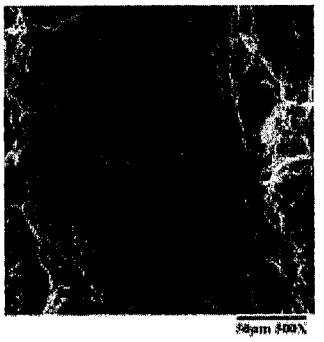

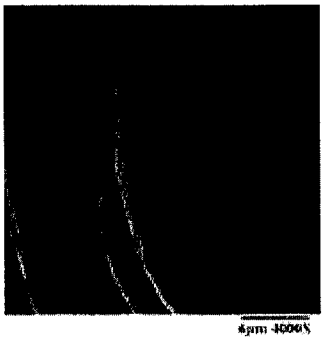

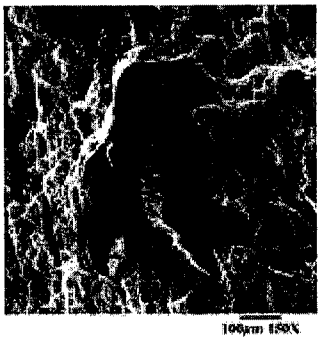

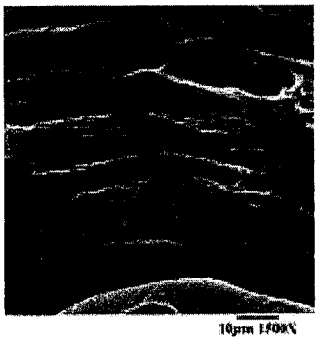

Figure 22

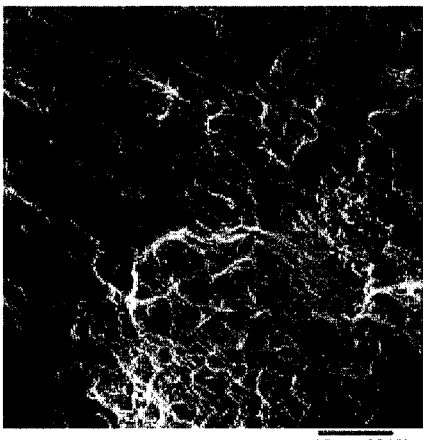

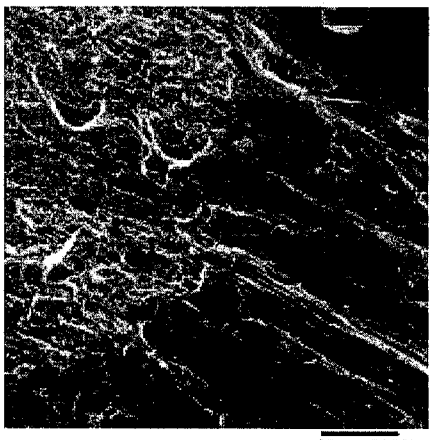

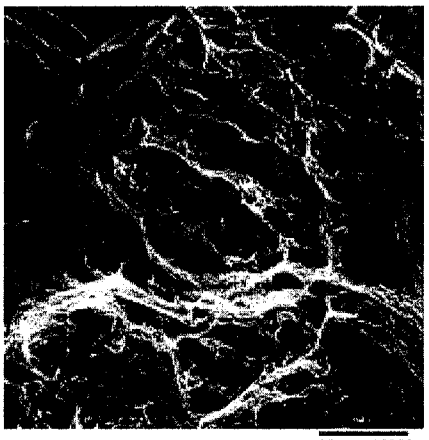

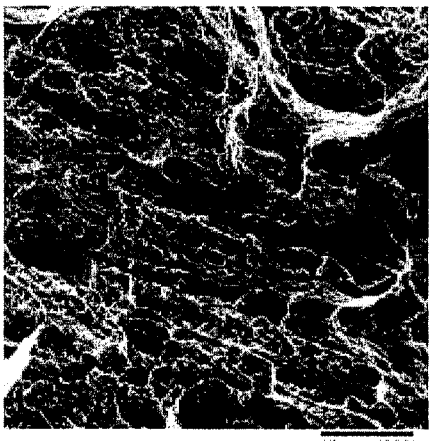

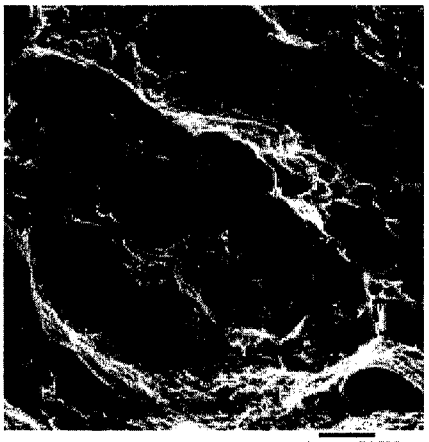

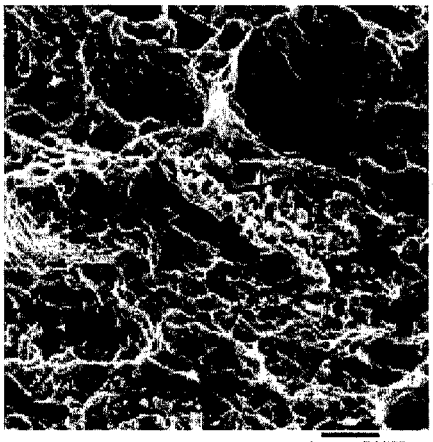

Mode I **Mode II**

Figure 23

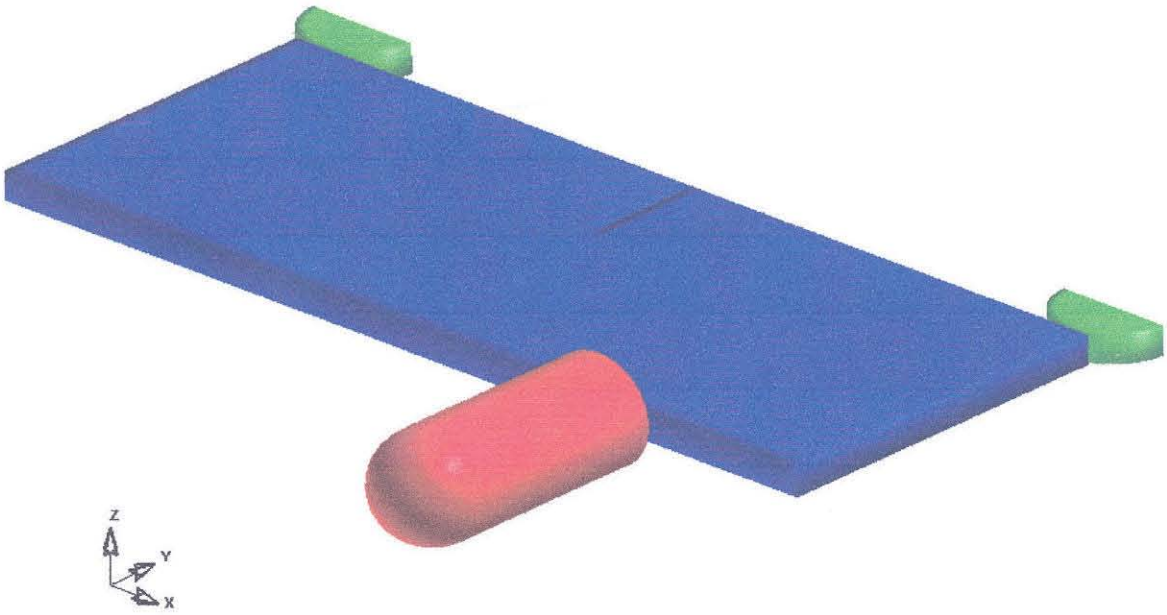

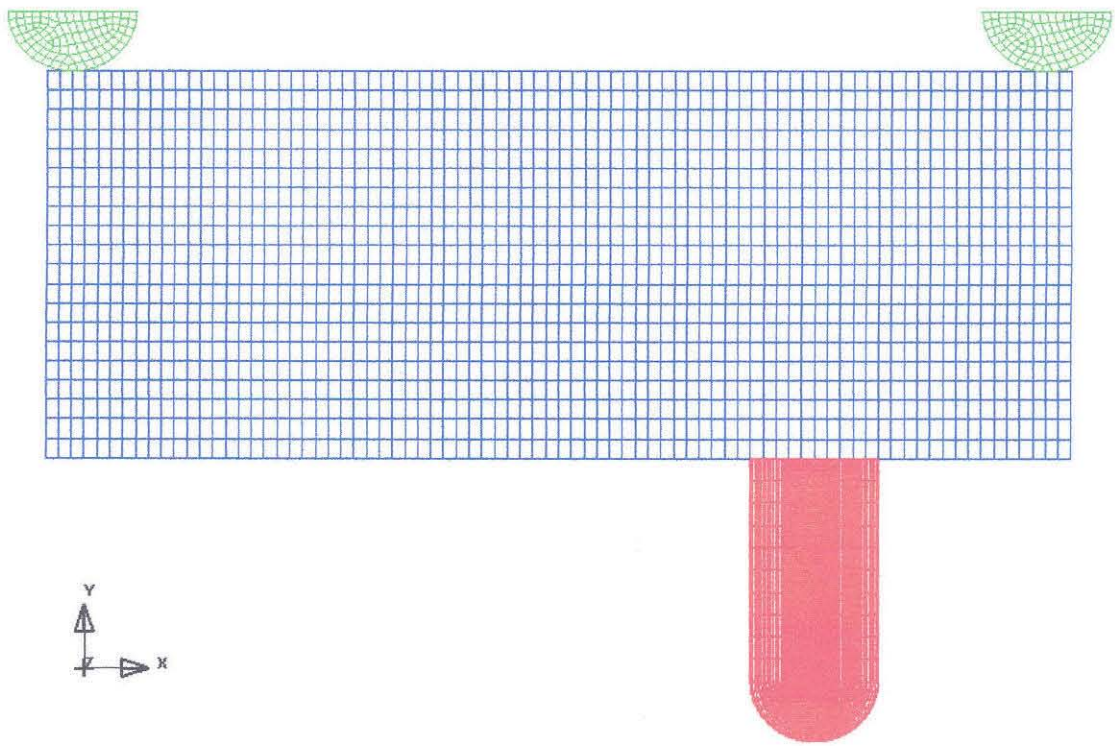

Figure 24

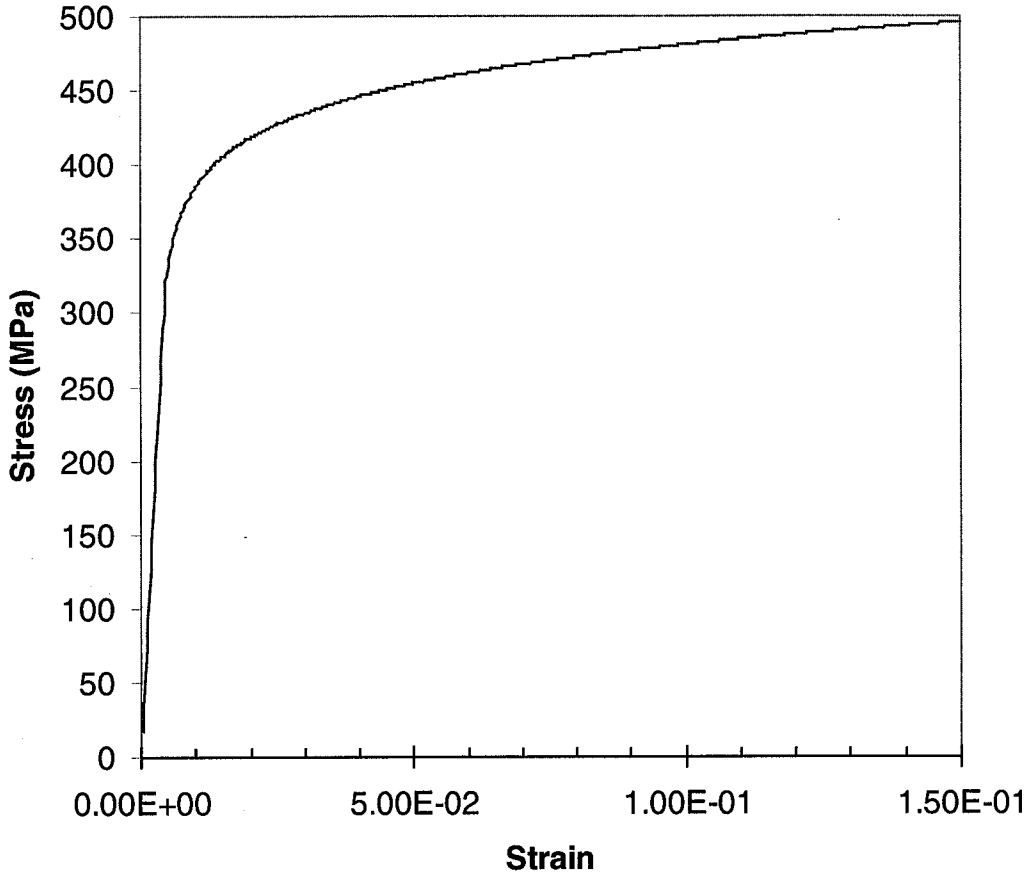
500
450
400
350
300
250
200
150
100
50
0
Stress (MPa)
0.00E+00
5.00E-02
1.00E-01
1.50E-01
Strain

Figure 25

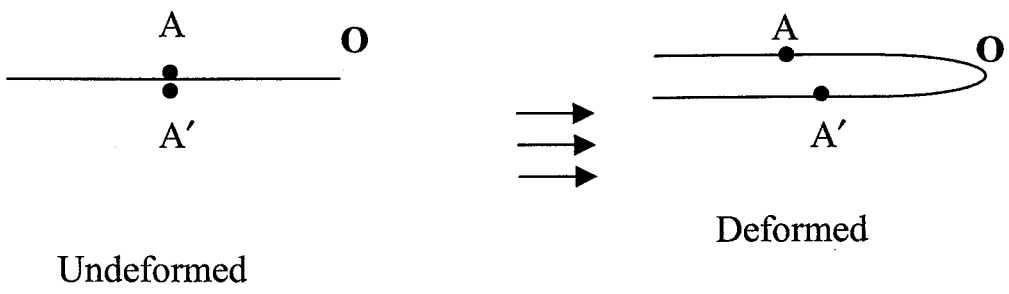

Figure 26

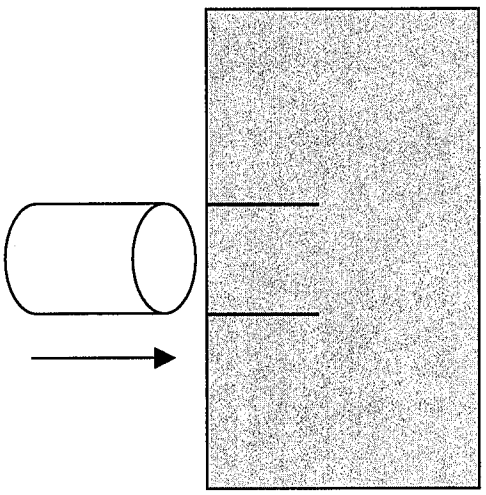

(a)

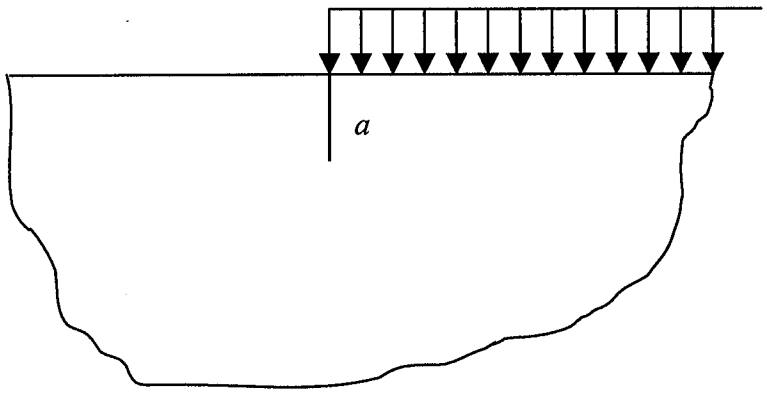

(b)

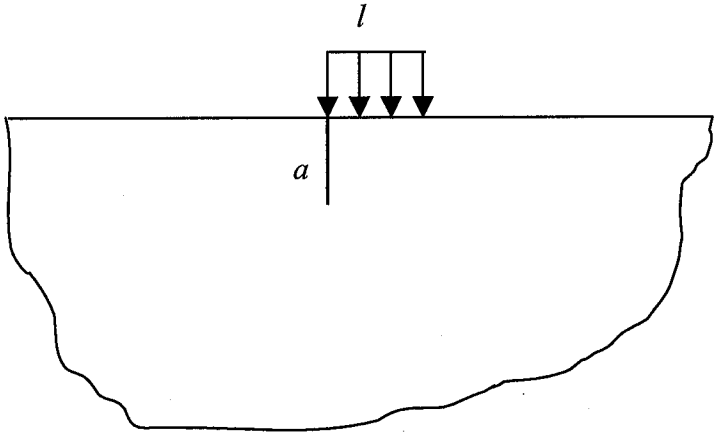

(c)

Figure 27

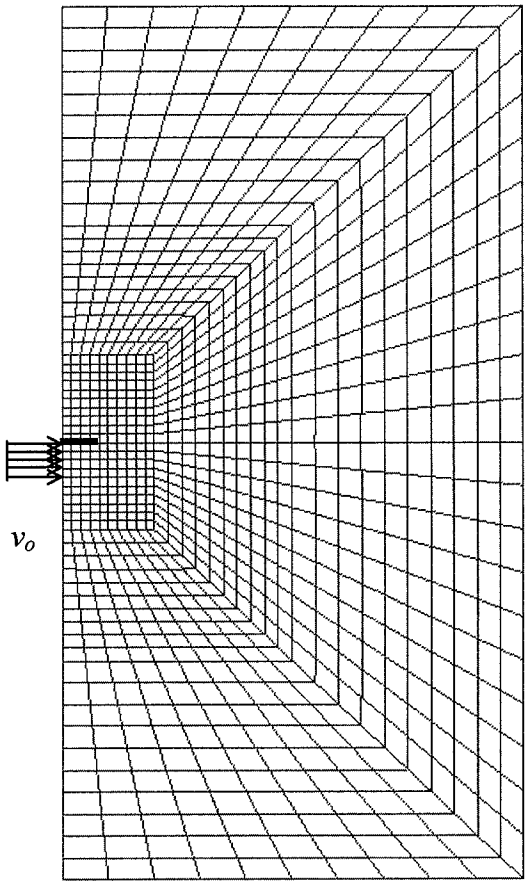

Figure 28

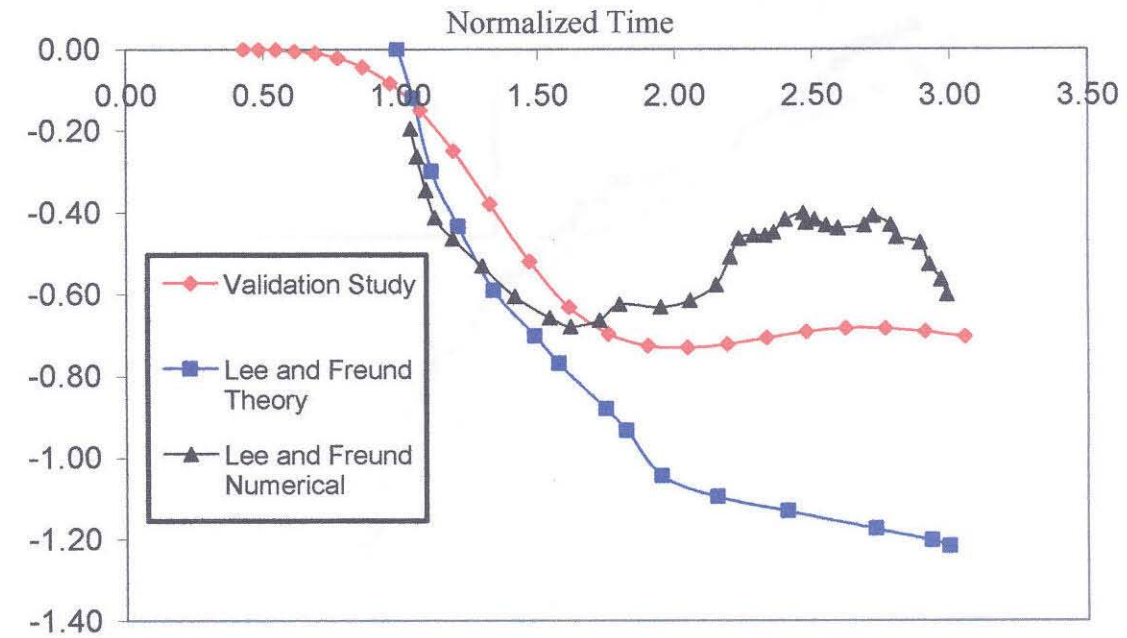
Normalized Time
0.00
0.50
1.00
1.50
2.00
2.50
3.00
3.50
0.00
-0.20
-0.40
-0.60
-0.80
-1.00
-1.20
-1.40
Validation Study
Lee and Freund Theory
Lee and Freund Numerical
Normalized K

Figure 29

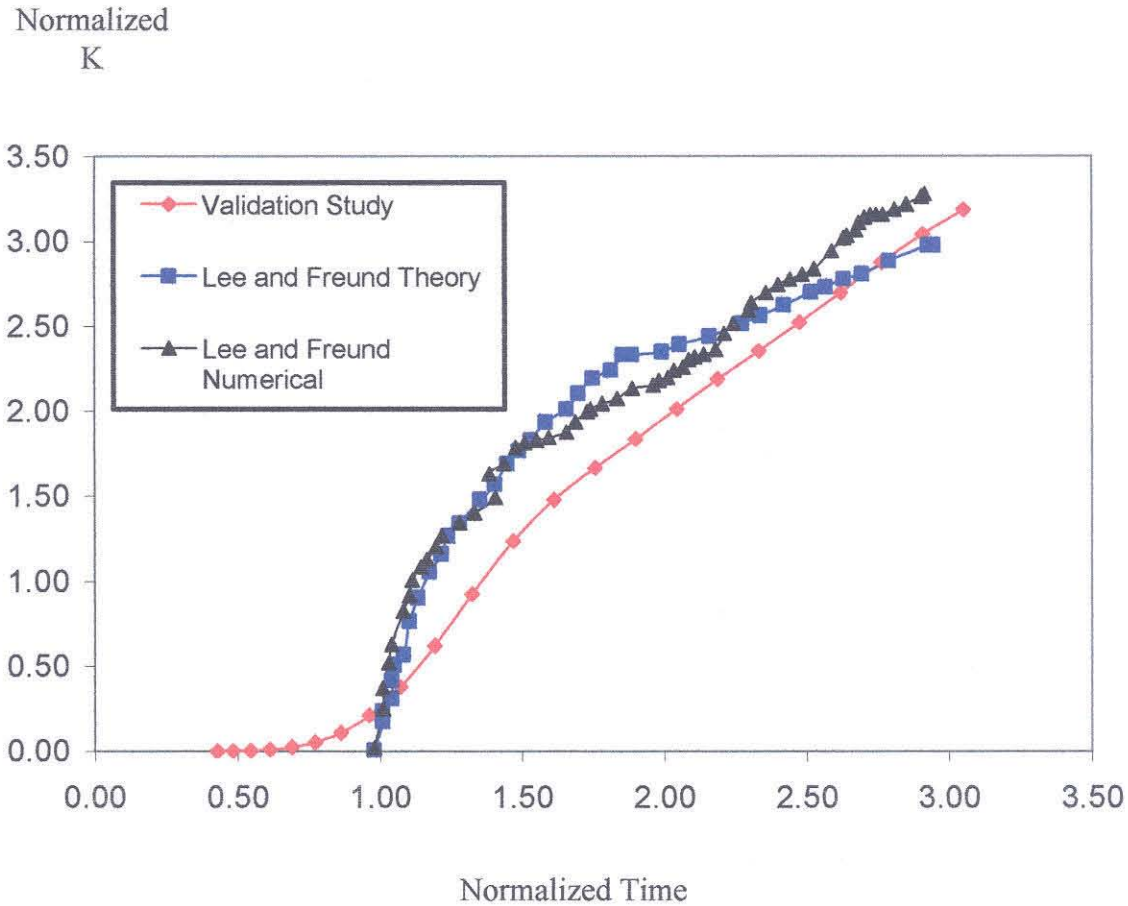
Normalized
K
3.50
3.00
2.50
2.00
1.50
1.00
0.50
0.00
0.00
0.50
1.00
1.50
2.00
2.50
3.00
3.50
Validation Study
Lee and Freund Theory
Lee and Freund
Numerical
Normalized Time

Figure 30

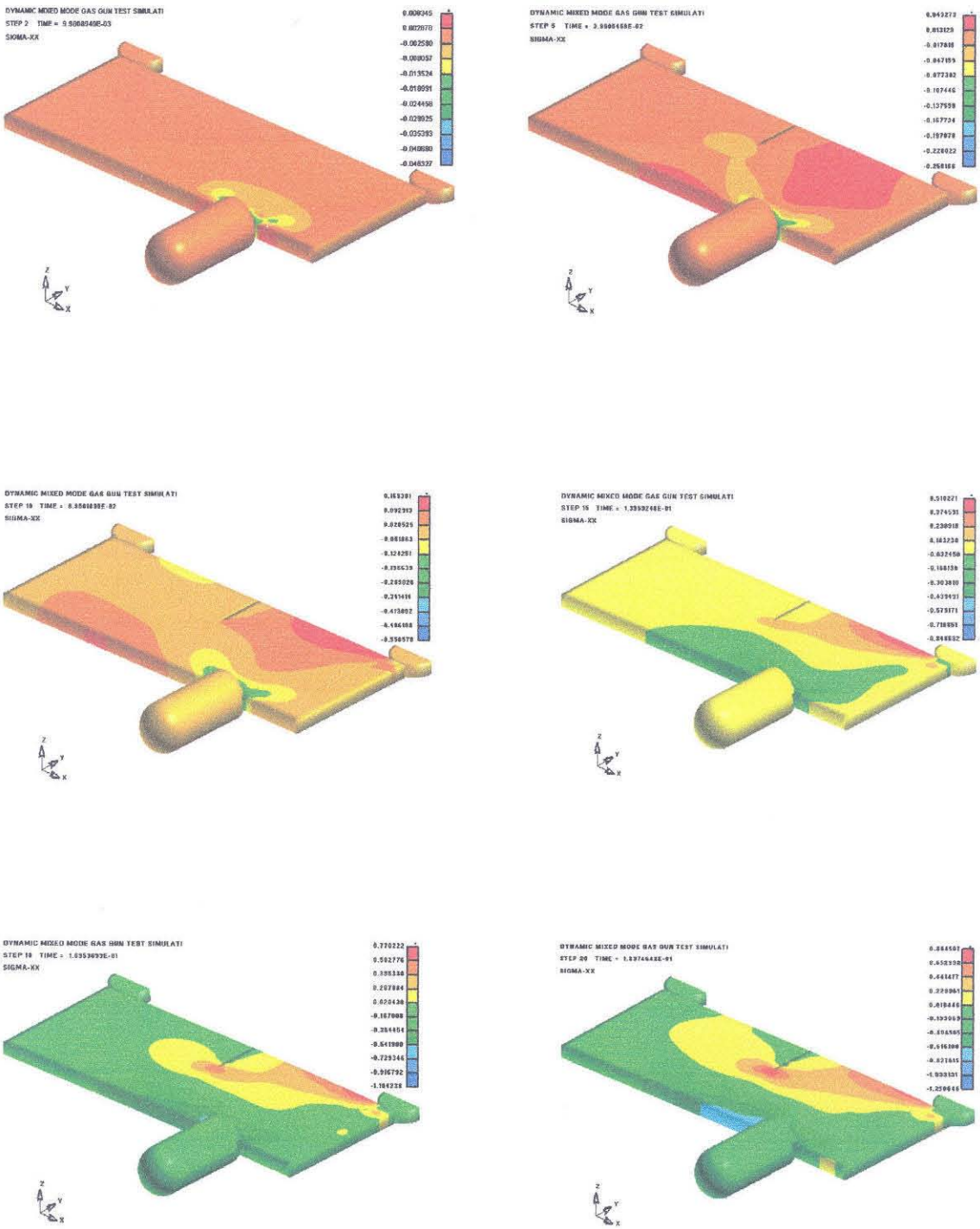
DYNAMIC MIXED MODE GAS GUN TEST SIMULATI
STEP 2 TIME = 9.9868340E-03
SIGMA-XX
DYNAMIC MIXED MODE GAS GUN TEST SIMULATI
STEP 5 TIME = 3.9965488E-02
SIGMA-XX
DYNAMIC MIXED MODE GAS GUN TEST SIMULATI
STEP 10 TIME = 8.9561838E-02
SIGMA-XX
DYNAMIC MIXED MODE GAS GUN TEST SIMULATI
STEP 15 TIME = 1.3993246E-01
SIGMA-XX
DYNAMIC MIXED MODE GAS GUN TEST SIMULATI
STEP 19 TIME = 1.8953693E-01
SIGMA-XX
DYNAMIC MIXED MODE GAS GUN TEST SIMULATI
STEP 20 TIME = 1.9974643E-01
SIGMA-XX

Figure 31

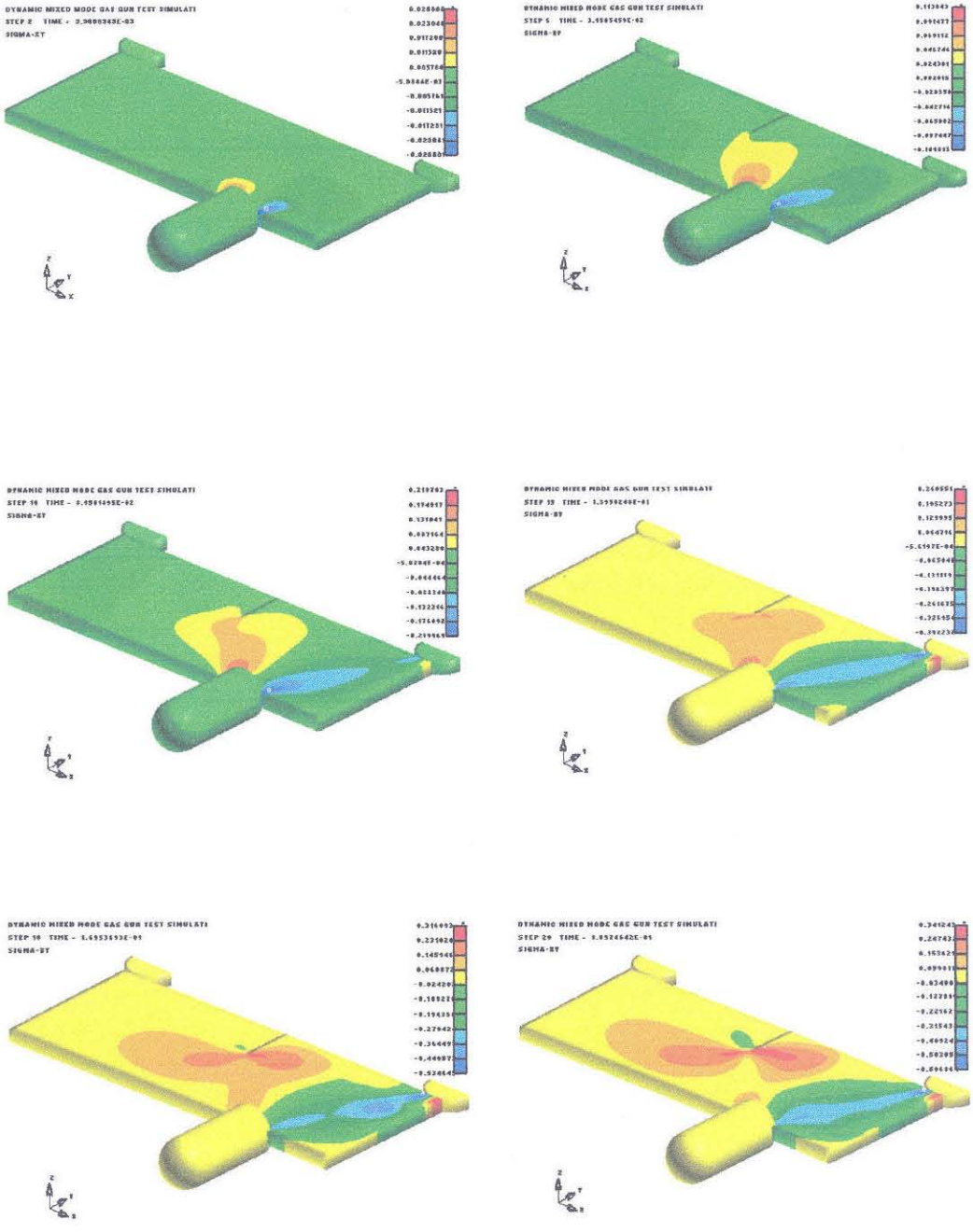

Figure 32

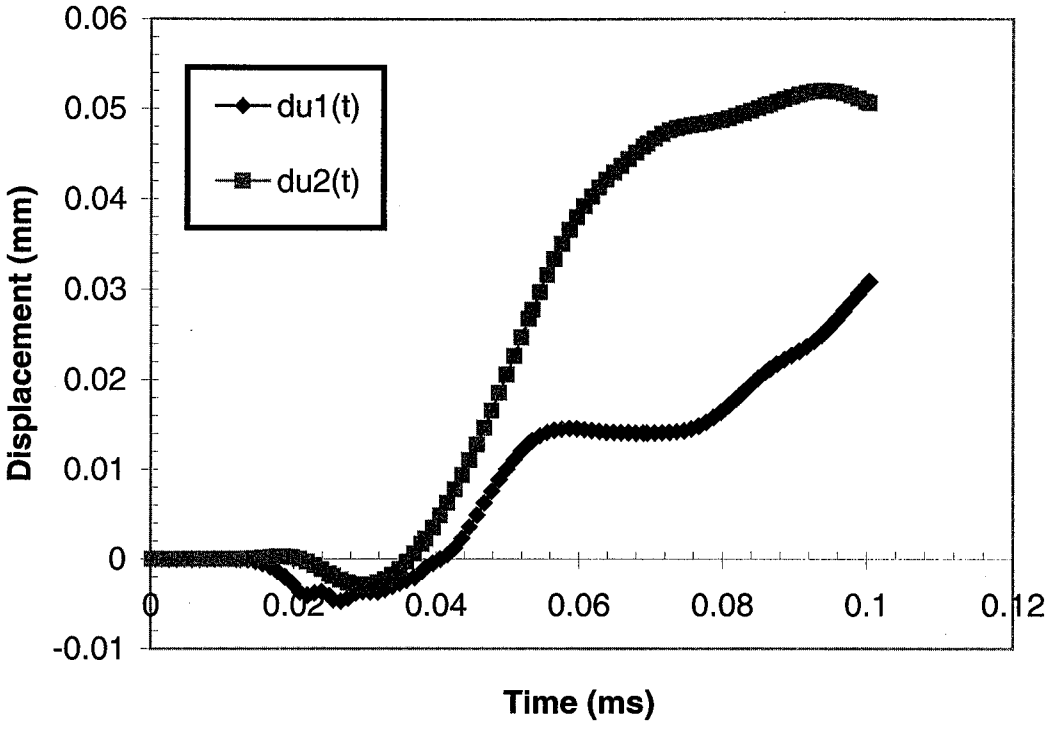
0.06
0.05
0.04
0.03
0.02
0.01
0
-0.01
Displacement (mm)
du1(t)
du2(t)
0
0.02
0.04
0.06
0.08
0.1
0.12
Time (ms)

Figure 33

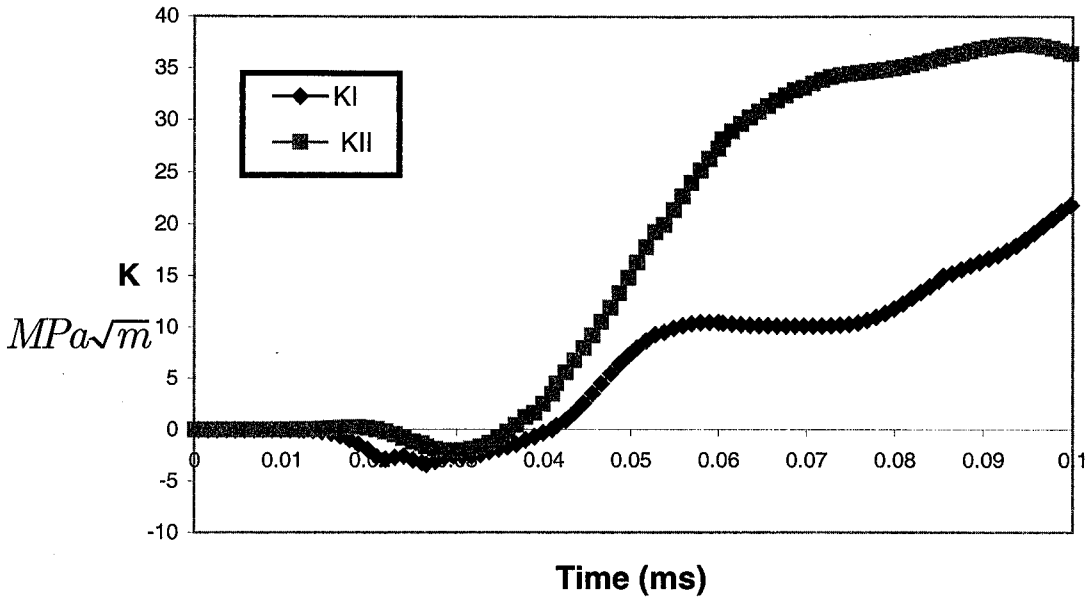
40
35
30
25
20
K
15
$MPa\sqrt{m}$
10
5
0
-5
-10
KI
KII
0
0.01
0.04
0.05
0.06
0.07
0.08
0.09
0.1
Time (ms)

Figure 34

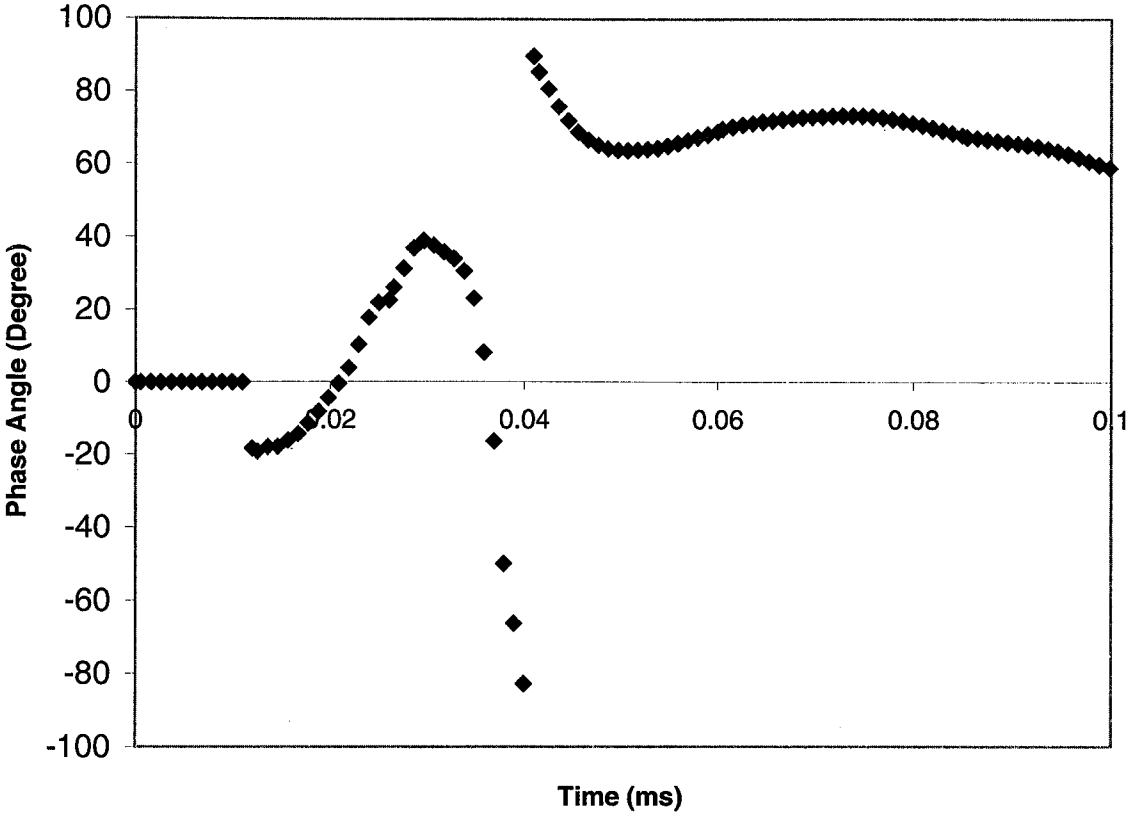
100
80
60
40
20
0
-20
-40
-60
-80
-100
Phase Angle (Degree)
0
.02
0.04
0.06
0.08
0.1
Time (ms)

Figure 35

$K_I^d(t)$

$MPa\sqrt{m}$

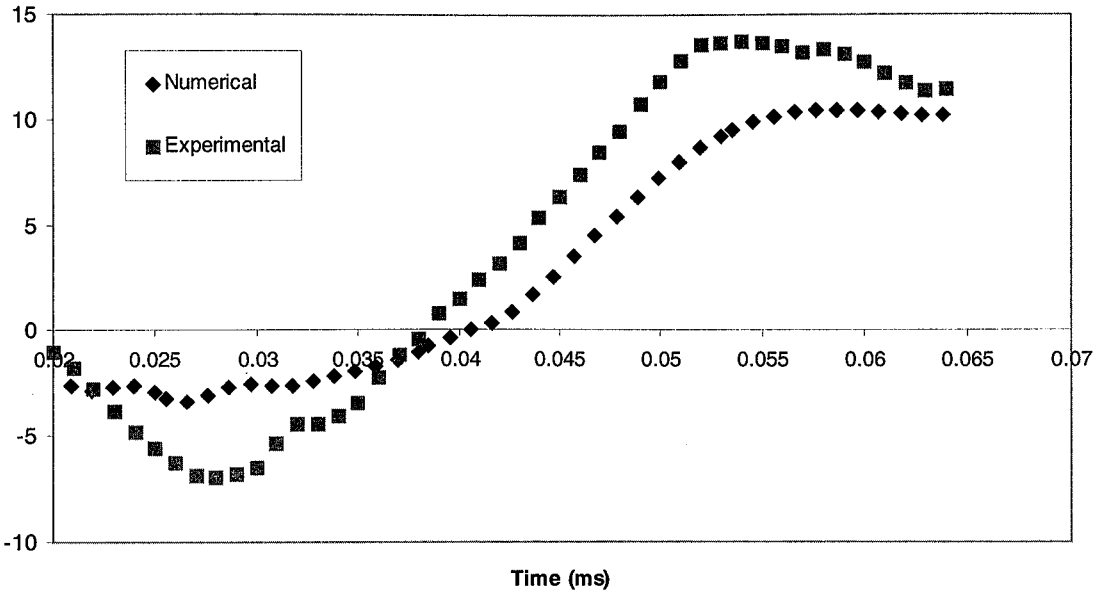

Figure 36

$K_{II}^{d}(t)$

$MPa\sqrt{m}$

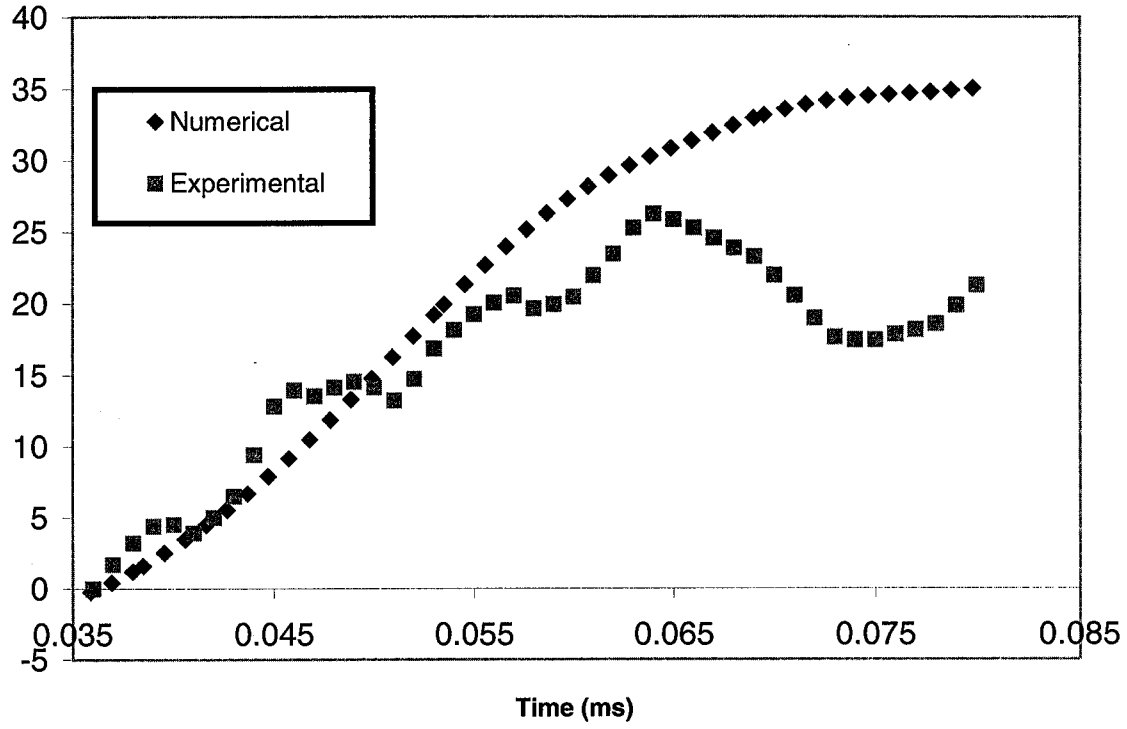

Figure 37

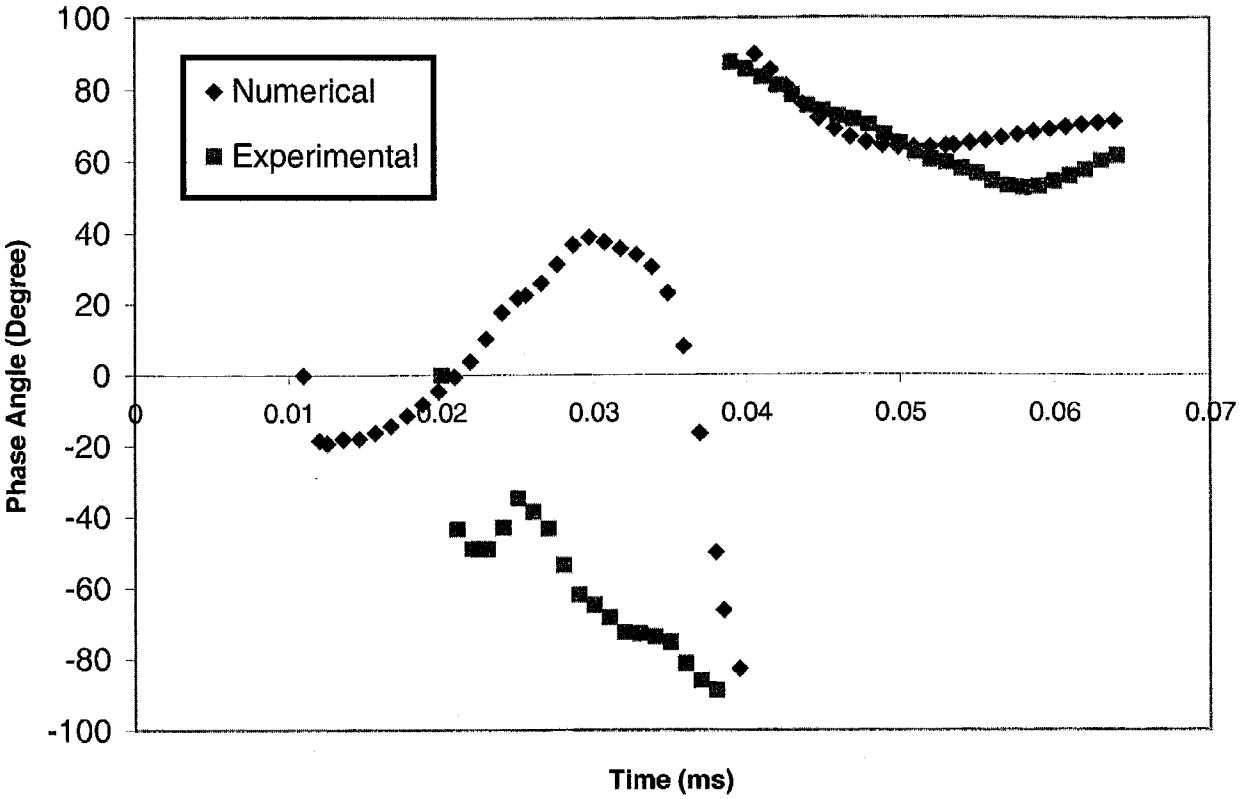
100
80
60
40
20
0
-20
-40
-60
-80
-100
Numerical
Experimental
Phase Angle (Degree)
0
0.01
0.02
0.03
0.04
0.05
0.06
0.07
Time (ms)

Figure 38